The Astrophysical Journal Supplement Series, 139:37–79, 2002 March

FAR-INFRARED PHOTOMETRY OF A STATISTICAL SAMPLE OF LATE-TYPE VIRGO CLUSTER GALAXIES[1]

Richard J. Tuffs, Cristina C. Popescu,[2, 3, 4] Daniele Pierini,[5] and Heinrich J. Völk
Max-Planck-Institut für Kernphysik, Saupfercheckweg 1, 69117 Heidelberg, Germany

Hans Hippelein
Max-Planck-Institut für Astronomie, Königstuhl 17, 69117 Heidelberg, Germany

Kieron Leech and Leo Metcalfe
ISO Data Center, Astrophysics Division, Space Science Department of ESA, Villafranca del Castillo, P.O. Box 50727, 28080 Madrid, Spain

and

Ingolf Heinrichsen and Cong Xu
Infrared Processing and Analysis Center, MS 100-22, 770 South Wilson Avenue, Pasadena, CA 91125
Received 2001 July 15; accepted 2001 October 9

ABSTRACT

We present deep diffraction-limited far-infrared (FIR) strip maps of a sample of 63 galaxies later than S0 and brighter than $B_T = 16.8$, selected from the Virgo Cluster Catalogue of Binggeli, Sandage, & Tammann. The ISOPHOT instrument on board the *Infrared Space Observatory* was used to achieve sensitivities typically an order of magnitude deeper than *IRAS* in the 60 and 100 μm bands and to reach the confusion limit at 170 μm. The averaged 3 σ upper limits for integrated flux densities of point sources at 60, 100, and 170 μm are 43, 33, and 58 mJy, respectively. A total of 63.5% are detected at all three wavelengths. The highest detection rate (85.7%) is in the 170 μm band. In many cases the galaxies are resolved, allowing the scale length of the infrared disks to be derived from the oversampled brightness profiles in addition to the spatially integrated emission. The data presented should provide the basis for a variety of statistical investigations of the FIR spectral energy distributions of gas-rich galaxies in the local universe spanning a broad range in star formation activity and morphological types, including dwarf systems and galaxies with rather quiescent star formation activity.

Subject headings: catalogs — galaxies: clusters: individual (Virgo) — galaxies: photometry — galaxies: statistics — infrared: galaxies — surveys

On-line material: machine-readable tables

1. INTRODUCTION

Galaxy emission in the far-infrared (FIR) is intimately connected to the current rate of star formation, since the characteristic radiation of young stars in the ultraviolet and optical wavelength range will at least in part be absorbed by interstellar dust. The *IRAS* all sky survey, within its limitations to wavelengths shorter than about 120 μm, raised statistical studies of star formation in galaxies to a new level, detecting over 25,000 objects (see Soifer, Neugebauer, & Houck 1987 for a review). Despite the bright (by optical standards) detection limit of $\sim$0.5 and 1.5 Jy at 60 and 100 μm, respectively, about half of the *IRAS* galaxies had no counterparts in optical catalogs at the time of the survey. In part, this was a consequence of the almost complete sky coverage and homogeneous data processing of the *IRAS* mission. However, it also reflected the fact that at luminosities greater than about 10^{11} $L_\odot$ optically selected galaxies are less common than *IRAS* galaxies. These luminous infrared objects are thought to be relatively distant systems undergoing intense bursts of massive star formation, probably triggered by mergers and interactions, in which the bulk of the stellar luminosity is locally absorbed by dust and reradiated in the FIR (see, e.g., Sanders & Mirabel 1996 for a review; Leech et al. 1994).

In the local universe the most common gas-rich systems are the so-called normal late-type galaxies (later than S0). By "normal" we loosely refer to galaxies which are not dominated by an active nucleus and whose current star formation rates (SFRs) would be sustainable for a substantial fraction of a Hubble time. These objects are intrinsically important, since, apart from the diffuse intergalactic gas, they comprise the dominant fraction of the baryonic matter in the universe. Perhaps of even more interest for structure formation and extragalactic astronomy is the fact that normal late-type galaxies are the best objects for the investigation of the still poorly understood mechanisms for star formation in galactic disks, as well as the associated global physical processes and their interrelations.

The deepest statistical investigation of normal galaxies in the local universe using *IRAS* was that of Devereux & Hameed (1997), who, after processing the data with the latest techniques, examined the FIR luminosity function at 60 μm for 1215 galaxies within a distance of 40 Mpc, selected from the Nearby Galaxies Catalog of Tully (1989). Even in

[1] Based on observations with the *Infrared Space Observatory* (*ISO*), an ESA project with instruments funded by ESA member states (especially the PI countries: France, Germany, the Netherlands, and the United Kingdom) and with the participation of ISAS and NASA.

[2] Present address: The Observatories of the Carnegie Institution of Washington, 813 Santa Barbara Street, Pasadena, CA 91101; popescu@ociw.edu.

[3] Otto-Hahn Fellow of the Max-Planck-Institut für Astronomie, Königstuhl 17, 69117 Heidelberg, Germany.

[4] Research Associate, The Astronomical Institute of the Romanian Academy, Str. Cutitul de Argint 5, Bucharest, Romania.

[5] Present affiliation: University of Toledo, Toledo, OH 43606-3390.

this catalog low optical luminosity galaxies and in particular low optical surface brightness galaxies are prone to be underrepresented. Furthermore, as discussed by Devereux & Hameed (1997), the sensitivity limit of the *IRAS* survey meant that only limited information could be derived for the FIR properties of less IR luminous objects and, in particular, of galaxies with almost quiescent star formation activity.

Further obvious biases of *IRAS* studies in general are the lack of spectral coverage longward of the 100 μm filter (for which the FWHM system response is approximately 80–120 μm; see Fig. II-C-9 of Beichman et al. 1988) and the 3 times brighter sensitivity limit in this band compared to the *IRAS* 60 μm band. This could translate into a bias against the detection of FIR emission from quiescent systems, if the 60/100 μm color ratio is indeed correlated with massive star formation activity as proposed by, e.g., Lonsdale & Helou (1987). More fundamentally, the suggestion of Chini et al. (1986) that the spatially integrated spectral energy distribution (SED) of late-type galaxies peaks in the 100–200 μm range and cannot be simply extrapolated by fitting the *IRAS* 60 and 100 μm photometric points with single-temperature dust emission components is now confirmed by initial studies with the *Infrared Space Observatory* (*ISO*) (e.g., Stickel et al. 2000; Popescu et al. 2002).

By virtue of its superior intrinsic sensitivity and the availability of longer integration times than were possible with *IRAS*, the ISOPHOT instrument (Lemke et al. 1996) on board *ISO* (Kessler et al. 1996) could detect discrete sources at least 10 times fainter than *IRAS* at 60 and 100 μm. It furthermore had a wavelength coverage extending to 240 μm. The basic observational goal of the project we present here is to use *ISO* to extend knowledge of the FIR SEDs to lower luminosity limits and to cover the peak in νS_ν for a complete sample of normal late-type galaxies, embracing a large range in morphological type and star formation activity.

Ideally, one would seek to achieve this by making a blind survey in the FIR by mapping a substantial fraction of the sky, analogous to *IRAS*. However, the optimum sensitivity to luminosity of a detection survey with ISOPHOT was for targets at such a distance that the angular size of the FIR emission region matched the angular resolution of *ISO* (45″ at 100 μm). For typical dwarf galaxies this corresponds to a distance of about 15 Mpc, so that the low surface number density of such close-by objects would have made a blind survey too costly.

An almost ideal alternative basis for a blind survey in the FIR is offered by the Virgo Cluster Catalogue (VCC), obtained by Binggeli, Sandage, & Tammann (1985) in their deep blue photographic survey. We therefore selected a sample of late-type galaxies from the VCC to be observed with ISOPHOT. From an observational point of view the Virgo Cluster has the advantage that it is situated at high Galactic latitude and is close to the ideal distance for the detection of dwarf galaxies with ISOPHOT. The VCC has a full representation of morphological types of normal gas-rich galaxies, including quiescent systems and even, to some extent, low surface brightness objects, ranging from bright ($B_T \sim 10$) giant spirals down to blue compact dwarfs (BCDs) and irregular galaxies at the completeness level of $B_T \sim 18$. Moreover, the VCC galaxies are the most carefully classified in terms of optical morphology. Virgo Cluster galaxies have been also extensively studied in the UV (Deharveng et al. 1994), optical (e.g., Schröder 1995), Hα, near-IR (Boselli et al. 1997b), radio continuum (Gavazzi & Boselli 1999; Niklas, Klein, & Wielebinski 1995), H I (Hoffmann et al. 1989 and references therein), and CO (e.g., Boselli, Casoli, & Lequeux 1995).

From an astrophysical point of view the cluster is ideal in that it is known to be a dynamically young system, with a significant fraction of galaxies freshly falling in from the field (Tully & Shaya 1984; Binggeli, Popescu, & Tammann 1993). The fundamental incentive for choosing the VCC as the basis of a statistical sample for ISOPHOT was thus that a luminosity- *and* volume-limited sample of cluster periphery and cluster core galaxies representative of the field and cluster environments, respectively, could be observed down to the least luminous dwarf galaxies reachable with ISOPHOT. This should allow an investigation of the strength and time dependence of all manifestations of star formation activity and its relation to intrinsic galaxy properties such as Hubble type or sheer overall size. Clusters are natural laboratories for the investigation of the effect on galaxy properties of external conditions such as the pressure and mass density of the diffuse intracluster medium (ICM), the large-scale gravitational potential of the cluster, or the interaction with other galaxies. This is particularly the case for the Virgo Cluster for which deep X-ray maps (Böhringer et al. 1994) of the ICM, as well as comprehensive measurements of the H I deficiencies (also for dwarf galaxies), are available (Hoffmann et al. 1989 and references therein). Another potential manifestation of galaxy-ICM interaction would be the detection of FIR emission in the vicinity of infalling spirals, arising from collisionally heated grains released from the disk through ram pressure stripping (Dwek, Rephaeli, & Mather 1990; Popescu et al. 2000b).

To maximize the statistics attainable in the fixed available observation time of 20.36 hr, the survey was made in just three broad bandpasses, centered at 60, 100, and 170 μm, which together encompass the range 40–240 μm. In all, a subset of 63 galaxies with $B_T \leq 16.8$ from the VCC were observed. These were selected from specific regions of the sky as described in § 2.

A basic aim of the survey was to derive integrated properties of the sample. This is especially appropriate for cluster samples at a fixed distance to enable the construction of FIR luminosity functions. Furthermore, the angular resolution of *ISO* (at 100 μm, 4 times superior to that of *IRAS*) was sufficient to resolve the disks of the giant spirals. This allowed a subsidiary science goal to be realized, namely, the provision of statistical information on scale lengths of spiral galaxies in the FIR, their relation to the optical scale lengths, and, to a limited extent, the separation of nuclear and disk emission components. An oversampled scanning technique was used to achieve the combined goals of obtaining integrated fluxes, structural information, and robustness against confusion with background sources or foreground cirrus emission, which limits the survey at the longest wavelength. The use of long scans means that our survey is sensitive to the emission of cold grains in the outer regions of the disks, which are prone to be missed or underrepresented in pointed observations of galaxies.

The combination of spatially integrated photometry extending in wavelength to 170 μm will provide the basis for the modeling of the SED of normal galaxies. In this wavelength range grains act as test particles probing the strength and color of the diffuse UV/optical radiation fields. This constitutes an entirely complementary constraint to direct

studies of stellar emission in the UV and optical bands. The SED modeling should yield statistical information on the disk opacities and the relative contributions of young and old stellar populations to the dust heating (see, e.g., Xu & Buat 1995; Silva et al. 1998; Devriendt, Guiderdoni, & Sadat 1999; Popescu et al. 2000a; Misiriotis et al. 2001). The SFR and star formation histories can in principle be derived from such techniques.

Another scientific goal of the survey is to study the statistical correlation of FIR emission of normal disk galaxies with other emissions from the radio to the X-ray spectral regions. In particular, an unexpected result from the *IRAS* mission was the especially tight correlation between the radio synchrotron and the FIR emission (e.g., Helou, Soifer, & Rowan-Robinson 1985; de Jong et al. 1985; Wunderlich, Wielebinski, & Klein 1987). The link is qualitatively assumed to be given by the grain heating associated with the appearance of massive stars and the acceleration of relativistic particles in their eventual supernova explosions. Basically the correlation can be explained in terms of a calorimetric theory (Völk 1989; Lisenfeld, Völk, & Xu 1996). One question raised by the *IRAS* studies is whether the effects of a cluster environment will indeed shift the FIR/radio correlation on average to considerably higher radio emission for given FIR intensity as claimed by Gavazzi, Boselli, & Kennicutt (1991). Another issue is the extent to which the constraints imposed on galactic properties by the correlation will apply to less massive and/or more quiescent systems than those typically studied with *IRAS*.

The sample of VCC galaxies selected for ISOPHOT also formed a substantial part of samples observed with *ISO* using the ISOCAM mid-IR camera in passbands centered at 6.9 and 15 μm (Boselli et al. 1997a, 1998) and the Long Wavelength Spectrometer at the 158 μm [C II] fine-structure gas cooling line (Leech et al. 1999). In particular, the latter observations provide complementary information about the energetics of the interstellar gas, the sources of [C II] emission within the interstellar medium (Pierini et al. 1999, 2001b), and the role played by different stellar populations in the gas heating (Pierini et al. 2002).

This is the first of a series of papers on the phenomology of the FIR emission of normal galaxies and its astrophysical implications, based on the ISOPHOT observations presented here. An analysis of the cold dust emission from Virgo Cluster galaxies is given by Popescu et al. (2002).

This paper is organized as follows. In § 2 we describe the selection criteria, optical properties, and completeness of the observed sample. Observational details and a description of the data analysis are given in §§ 3 and 4, respectively. The photometric characteristics of the survey, including comparisons with *IRAS* and *COBE* photometry, are given in § 5. The extraction of the integrated photometry and the resulting catalog with associated plots are presented in § 6. Basic properties and detection statistics are derived in § 7, and the main results of the paper are summarized in § 8.

2. THE SAMPLE

A sample of 62 VCC galaxies selected from the Virgo Cluster Catalogue (Binggeli et al. 1985) with Hubble type later than S0 were selected according to criteria based on their projected position and magnitude. The sample galaxies lie in two sky areas called "core" and "periphery," where the spread in distance within the sample, which is due to the complex three-dimensional structure of the cluster (Binggeli et al. 1993 and references therein), is minimized. These areas were chosen in order to optimize the statistical evaluation of the environmental effects of the cluster, if any, on the observed properties of galaxies of the same morphology. It is well known that galaxies in the cluster core are H I deficient (Haynes & Giovanelli 1984) while galaxies in the cluster periphery have the same H I content as field galaxies.

The so-called *cluster core subsample* is comprised of 25 certain spiral galaxies brighter than $B_T = 14.5$, with projected positions within 2° of M87 (Fig. 1), essentially seen toward the extended X-ray halo of M87 (Böhringer et al. 1994). These galaxies define an optically complete sample of galaxies later than S0 and earlier than Im. *The cluster periphery subsample* is comprised of 37 spiral, irregular, or BCD galaxies with $B_T \leq 16.8$ and with angular separations of greater than 4° from the position of maximum projected galaxy density given by Binggeli, Tammann, & Sandage (1987) (Fig. 1). Objects with R.A.(1950.0) $> 12^{\rm h}.596$ or within 1°.5 of the position of maximum projected galaxy density of the M49 subcluster are excluded. In addition, objects seen toward the M and W clouds (as defined in Fig. 1 of Sandage, Binggeli, & Tammann 1985 and also reproduced in our Fig. 1) or in the southern extension ($\delta < 5°$) are also excluded. The limiting magnitude of $B_T = 16.8$ is well within the VCC completeness limit of $B_T \sim 18$. These two subsamples constitute two volume- and magnitude-limited samples of late-type galaxies. The selected galaxies consist of 60 members and two possible members (VCC 130 and VCC 890) of the Virgo Cluster (Binggeli et al. 1993).

Because of technical problems with spacecraft operations for some observations, 60 out of the 62 selected VCC galaxies were actually observed with ISOPHOT, giving a statistical completeness of 97%. In particular, all 25 galaxies of the core subsample and 35 out of the 37 galaxies of the periphery subsample were observed, the two observed subsamples having a statistical completeness of 100% and 94%, respectively. Hereafter, we refer to the 60 VCC galaxies observed by us with ISOPHOT as the *statistical sample* (marked as circles in Fig. 1).

In addition to this statistical sample, an extended program to observe the remaining 20 cluster member late-type galaxies fainter than $B_T = 14.5$ from the cluster core region was initiated to provide a statistical comparison to faint galaxies (most particularly the Im and BCD galaxies) in the cluster periphery subsample. However, because of scheduling and visibility constraints, only three galaxies (VCC 1001, VCC 1121, and VCC 1569) from this extended program were actually observed (marked as crosses in Fig. 1).

Table 1 lists the optical and FIR (*IRAS*) properties of all 63 VCC galaxies observed by us with ISOPHOT. Our statistical sample includes seven early-type spiral galaxies with claims of Seyfert/LINER activity or of both (see Table 1). For VCC 836 (Philips & Malin 1982), VCC 857 (Keel 1983), VCC 1690, and VCC 1727 (Stauffer 1982), these claims were raised before the selection and observation of our statistical sample. On the other hand, VCC 92 (Barth et al. 1998), VCC 1690, and VCC 1727 (Ho, Filippenko, & Sargent 1997) have recently been defined as transition spirals, while VCC 857 (Rauscher 1995) and VCC 1043 (Ho et al. 1997) seem to be marginal candidates for nonstellar nuclear activity. The phenomenology of Virgo Cluster spiral galaxy nuclear regions has not yet been established (e.g., Rauscher 1995), since different types of LINERs (i.e., photoionized by

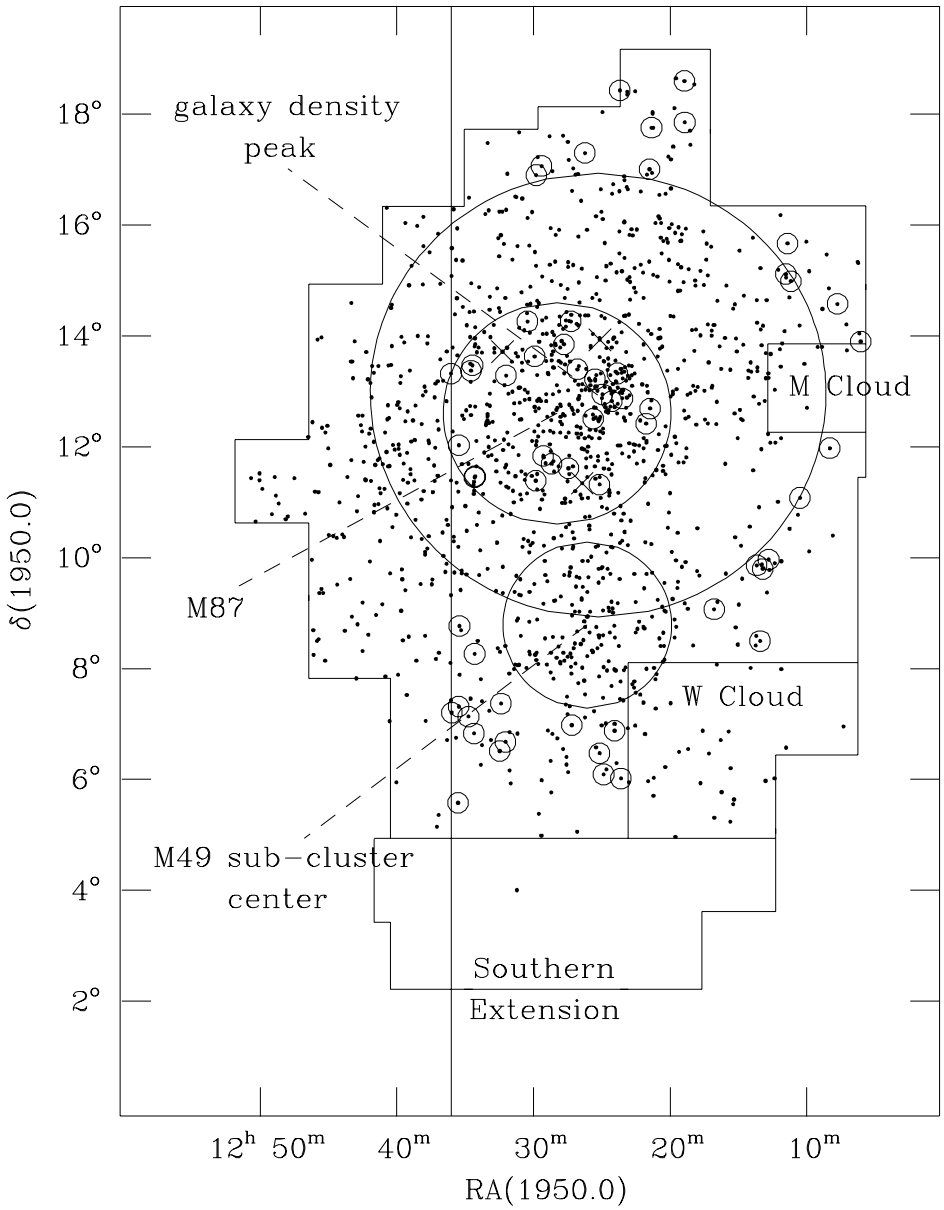

FIG. 1.—Plot of the VCC member galaxies (*filled circles*), as defined by Bingelli et al. (1985, 1993), with the cluster topology as given by Sandage et al. (1985). The 60 VCC galaxies of the statistical sample and the three VCC galaxies of the extended sample observed by us are marked with open circles and crosses, respectively. The figure also shows the 4° radius region centered on the maximum projected galaxy density of the cluster (Binggeli et al. 1987), the 2° radius region centered on M87, the 1°.5 radius region centered on the position of the maximum projected density of the M49 subcluster, and the boundary line at R.A.(1950.0) = $12^{h}.596$ (see text).

a stellar continuum or by an active galactic nucleus) cannot easily be distinguished from one another (e.g., Alonso-Herrero, Rieke, & Rieke 2000). Given this, we still consider it reasonable to include these seven VCC spiral galaxies as part of our statistical sample of normal late-type galaxies.

Figures 2*a* and 2*b* show the distribution of the objects of the core and of the periphery subsamples, respectively, in the plane defined by their Hubble type and total apparent blue magnitude B_T. The figures show that all galaxies in the core subsample and all periphery galaxies brighter than $B_T = 16.5$ were observed (*filled symbols*). The core and periphery subsamples are thus complete to $B_T = 14.5$ and 16.5, respectively. It is also evident that the periphery subsample is dominated by spiral galaxies later than Sbc and by irregular or dwarf spiral galaxies, while the core subsample is dominated by spiral galaxies of type Sc and earlier. This behavior reflects the combination of the morphology-density relation with the morphology-luminosity relation (Sandage et al. 1985). In this respect, the two subsamples are complementary, so that our statistical sample represents the overall phenomenology of the *normal* spiral, irregular, or dwarf spiral galaxies brighter than $B_T = 16.5$.

3. OBSERVATIONS

All observations were made using ISOPHOT's "P32" Astronomical Observing Template (R. J. Tuffs & C. Gabriel 2002, in preparation), which combines the standard spacecraft raster pointing mode (stepping in spacecraft Y and Z coordinates) with scans in Y made with the focal plane

TABLE 1

GALAXY PARAMETERS

VCC	Other Denominations	C/P[a]	α(2000.0)	δ(2000.0)	D[b] (arcmin)	R[c]	P.A.[d] (deg)	Type	B_T (mag)	F_{60}[e] (Jy)	F_{100} (Jy)	Notes
1.....		P	12 08 20.3	13 41 03	0.8	4.3	0	BCD?	14.8			
17.....		P	12 10 01.8	14 22 00	1.4	2.0	0	Im	15.2			
24.....		P	12 10 35.6	11 45 39	0.8	2.7	0	BCD	14.9			
66.....	NGC 4178, UGC 7215	P	12 12 46.5	10 52 06	6.6	2.8	30	SBc	11.9	2.8	9.0	H II
81.....	NGC 4192A, UGC 7223	P	12 13 26.2	14 46 20	1.8	1.2	0	d:Sc	15.6			
87.....		P	12 13 41.3	15 27 13	1.8	2.0	0	Sm	15.0			
92.....	M98, NGC 4192, UGC 7231	P	12 13 48.3	14 54 01	12.0	3.7	155	Sb:	10.9	6.5	21.5	H II, LINER[f, g]
130.....		P	12 15 04.0	09 45 13	0.4	2.5	0	BCD	16.5			
152.....	NGC 4207, UGC 7268	P	12 15 30.4	09 35 09	2.3	2.2	124	Scd	13.5	2.9	7.4	
159.....		P	12 15 41.5	08 17 08	0.9	2.0	0	Im	15.1			
169.....		P	12 15 56.4	09 38 56	1.0	2.0	0	Im	16.5			
318.....	IC 776, UGC 7352	P	12 19 02.9	08 51 22	2.1	1.7	98	SBcd	14.0			
459.....		P	12 21 11.2	17 38 18	0.6	2.3	0	BCD	14.9	0.2	0.5	
460.....	NGC 4293, UGC 7405	P	12 21 12.8	18 22 57	6.3	1.7	72	Sa pec	11.2	4.6	10.4	
655.....	NGC 4344, UGC 7468	P	12 23 37.5	17 32 27	1.4	1.0	0	S pec/BCD	13.2	0.4	1.9	
664.....	IC 3258, UGC 7470	C	12 23 44.5	12 28 42	3.2	1.4	0	Sc	13.7	0.5	0.7	
666.....		P	12 23 46.1	16 47 29	1.3	1.7	0	Im:	16.8			
692.....	NGC 4351, UGC 7476	C	12 24 01.6	12 12 18	3.6	1.5	80	Sc	13.0	0.6	2.1	
836.....	NGC 4388, UGC 7520	C	12 25 46.7	12 39 44	6.3	4.1	92	Sab	11.8	10.1	17.4	Sy2[h, i, j]
848.....		P	12 25 52.5	05 48 33	1.4	1.2	0	Im pec/BCD	14.7			
857.....	NGC 4394, UGC 7523	P	12 25 55.7	18 12 49	4.5	1.0	0	SBb	11.8	1.0	4.0	LINER[f, k]
873.....	NGC 4402, UGC 7528	C	12 26 07.7	13 06 48	4.9	3.4	90	Sc	12.6	5.4	17.4	
890.....		P	12 26 21.5	06 40 10	0.1	1.0	0	BCD	16.0			
912.....	NGC 4413, UGC 7538	C	12 26 32.2	12 36 40	3.6	1.7	60[l]	SBbc	13.0	1.1	2.9	
971.....	NGC 4423, UGC 7556	P	12 27 09.0	05 52 49	3.8	7.1	18	Sd	14.3	0.5	1.1	
984.....	NGC 4425, UGC 7562	C	12 27 13.3	12 44 05	3.7	3.0	27	SBa	12.8	<0.2	<0.5	
1001[m]...		C	12 27 24.4	13 42 57	0.5	1.5	0	Im	16.6			
1002.....	NGC 4430, UGC 7566	P	12 27 26.4	06 15 44	2.7	1.1	80	SBc	12.5	1.2	3.2	
1003.....	NGC 4429, UGC 7568	C	12 27 26.7	11 06 27	10.0	2.3	99	S0/Sa pec	11.4	1.4	4.3	
1043.....	NGC 4438, UGC 7574	C	12 27 45.6	13 00 32	10.0	2.2	27	Sb (tides)	10.9	3.7	13.1	LINER[n]
1047.....	NGC 4440, UGC 7581	C	12 27 53.5	12 17 36	2.5	1.2	0	SBa	12.7	<0.2	<0.5	
1110.....	NGC 4450, UGC 7594	P	12 28 29.5	17 05 06	7.6	1.5	175	Sab pec	10.9	1.4	7.6	LINER[o]
1121[m]...		C	12 28 41.8	11 07 55	0.9	1.3	0	Im?	16.4			
1158.....	NGC 4461, UGC 7613	C	12 29 03.0	13 11 02	4.4	2.7	9	Sa	12.1	<0.2	<0.8	
1189.....	IC 3414, UGC 7621	P	12 29 28.9	06 46 12	2.0	1.7	35	Sc	13.7	0.3	0.6	
1196.....	NGC 4468, UGC 7628	C	12 29 31.1	14 02 58	1.8	1.7	73	S0/a	13.8			
1217.....	IC 3418, UGC 7630	C	12 29 43.8	11 24 09	2.3	1.5	0	SBm	14.0			
1253.....	NGC 4477, UGC 7638	C	12 30 02.2	13 38 11	4.5	1.0	15	SB0/SBa	11.3	0.6	1.2	
1326.....	NGC 4491, UGC 7657	C	12 30 57.2	11 28 59	2.1	2.0	148	SBa	13.4	2.8	3.3	
1368.....	NGC 4497, UGC 7665	C	12 31 32.5	11 37 29	2.5	2.3	65	SB0/SBa	13.3	<0.2	<0.8	
1379.....	NGC 4498, UGC 7669	P	12 31 39.5	16 51 10	3.5	1.9	133	SBc	12.6	1.1	4.0	
1410.....	NGC 4502, UGC 7677	P	12 32 03.3	16 41 16	1.3	1.9	0	Sm	14.6	0.2	0.6	
1412.....	NGC 4503, UGC 7680	C	12 32 06.1	11 10 35	5.4	2.5	12	Sa	12.1	<0.2	<1.0	
1419.....	NGC 4506, UGC 7682	C	12 32 10.5	13 25 11	2.7	1.7	110	S pec (dust)	13.6	<0.2	<0.8	
1450.....	IC 3476, UGC 7695	C	12 32 41.9	14 03 00	3.2	1.3	30	Sc	13.3	1.4	3.1	
1552.....	NGC 4531, UGC 7729	C	12 34 15.9	13 04 32	5.2	1.7	155	Sa pec	12.6	0.3	1.4	
1554.....	NGC 4532, UGC 7726	P	12 34 19.3	06 28 07	3.2	2.6	160	Sm	12.3	9.6	16.4	
1569.....	IC 3520	C	12 34 31.7	13 30 14	1.3	1.5	0	Scd:	15.0			
1575.....	IC 3521, UGC 7736	P	12 34 39.5	07 09 36	1.3	1.4	0	SBm pec	14.0	1.2	2.3	
1581.....	UGC 7739	P	12 34 45.3	06 18 02	1.3	1.3	0	Sm	14.5			
1673.....	NGC 4567, UGC 7777	C	12 36 32.7	11 15 28	3.6	1.5	85	Sc	12.1	20.4	56.8	Paired[p]
1675.....		P	12 36 34.9	08 03 16	1.0	1.7	0	pec	14.5			
1676.....	NGC 4568, UGC 7776	C	12 36 34.3	11 14 17	6.3	2.9	23	Sc	11.7	20.4	56.8	Paired[p]
1678.....	IC 3576, UGC 7781	P	12 36 37.6	06 37 17	2.7	1.1	0	SBd	13.7	<0.2	<0.5	H II
1686.....	IC 3583, UGC 7784	C	12 36 43.5	13 15 34	3.5	1.6	0	Sm	13.9	0.4	<1.2	
1690.....	M90, NGC 4569, UGC 7786	C	12 36 49.8	13 09 46	13.2	2.0	23	Sab	10.2	8.3	25.0	LINER, Sy[k, n, q]
1699.....	IC 3591, UGC 7790	P	12 37 03.0	06 55 36	1.4	1.9	0	SBm	14.1	<0.4	<0.6	
1725.....		P	12 37 41.2	08 33 33	1.4	1.6	0	Sm/BCD	14.5			
1726.....	UGC 7795	P	12 37 45.2	07 06 12	1.6	1.3	0	Sdm	14.5			
1727.....	M58, NGC 4579, UGC 7796	C	12 37 43.4	11 49 05	7.8	1.3	95	Sab	10.6	4.9	19.6	LINER, Sy1.9[n, q]

TABLE 1—*Continued*

VCC	Other Denominations	C/P[a]	α(2000.0)	δ(2000.0)	D[b] (arcmin)	R[c]	P.A.[d] (deg)	Type	B_T (mag)	F_{60}[e] (Jy)	F_{100} (Jy)	Notes
1730	NGC 4580, UGC 7794	P	12 37 48.6	05 22 07	2.7	1.3	165	Sc/Sa	12.6	1.3	4.3	
1750		P	12 38 15.5	06 59 39	0.2	2.0	0	BCD	16.5			
1757	NGC 4584, UGC 7803	C	12 38 17.9	13 06 36	2.3	1.9	5	Sa pec	13.7	0.2	0.4	

NOTE.—Units of right ascension are hours, minutes, and seconds, and units of declination are degrees, arcminutes, and arcseconds. Table 1 is also available in machine-readable form in the electronic edition of the *Astrophysical Journal Supplement*.

[a] Subsample classification: "C" and "P" denote core and periphery, respectively.

[b] Major diameter (in arcmin) to the faintest detectable surface brightness level of approximately 25.5 B-band mag arcsec^{-2} (VCC).

[c] Major to minor axis ratio (VCC).

[d] Position angle of major axis (in deg, eastward from north), taken from the UGC (Nilson 1973), only given where known for VCC galaxies brighter than or equal to $B_T = 14.5$. Face-on galaxies and all galaxies fainter than $B_T = 14.5$ are assigned a value of 0; no galaxy fainter than $B_T = 14.5$ is larger than 3.′5 in major axis diameter, which is the UGC limit.

[e] *IRAS* 60 μm spatially integrated flux density (where known), or its upper limit (3 σ value). Values are taken from Klatt 1993 for galaxies brighter than $B_T = 14.0$ and from Helou et al. 1988, Moshir et al. 1990, or Thuan & Sauvage 1992 for galaxies fainter than this.

[f] Rauscher 1995.

[g] Barth et al. 1998.

[h] Phillips & Malin 1982.

[i] Phillips, Charles, & Baldwin 1983.

[j] Falcke, Wilson, & Simpson 1998.

[k] Keel 1983.

[l] The value of 0° for the position angle of VCC 912 in the VCC catalog is incorrect. We measured it from an R-band image taken at the Calar Alto 2.2 m telescope to be 60°. Our measurement was kindly confirmed by B. Binggeli (2001, private communication).

[m] Galaxy outside the statistical sample.

[n] Ho et al. 1997.

[o] González Delgado et al. 1997.

[p] VCC 1673 is paired with VCC 1676; the integrated *IRAS* flux density for the pair is given.

[q] Stauffer 1982.

chopper. At each spacecraft raster position the focal plane chopper is stepped at intervals of one-third of the detector pixel pitch, resulting in sky samplings in Y of $\sim$15″ and 31″ for the C100 and C200 detectors, respectively. This is close to the limit for Nyquist sampling of $(17'' \times \lambda)/100$ μm.

The dimension of the spacecraft raster in Y was always made large enough to ensure that the scans spanned the projection of the optical diameters (to the 25.5 mag arcsec^{-2} B-band isophote) in Y, plus at least one independent resolution element beyond this limit at each scan end. This technique ensured that the survey was sensitive to any infrared emission from a galaxy with as large an extent as the optical extent, while at the same time sampling the target finely enough to probe the basic morphology of the disk emission. These attributes were especially relevant to observations of the bright giant spirals in the sample. A particular aim was to be sensitive to any faint emission from cold dust in the outer disk. Typically, only one spacecraft scan leg was made for the giant spirals. The only exception was the galaxy pair VCC 1673/VCC 1676, which was mapped in two dimensions, to facilitate the morphological separation of the two systems. The single-scan observations resulted in strip maps of three and two rows in the spacecraft Z coordinate for the C100 and C200 detectors, respectively, separated by 46″ and 92″. Although undersampled in Z, the integrated properties of the galaxies could in almost all instances be recovered using the modeling procedures described in § 6. In a few unfavorable cases in which the scan direction in spacecraft Y approached being perpendicular to the major axis of the galaxy, some extended emission from the disk was missed.

The oversampling in Y afforded by the P32 mapping technique was also well suited to the fainter targets (generally BCD and irregular galaxies) in the sample, as it mitigated the effects of confusion with the foreground cirrus emission from the Milky Way. To reach the confusion limit, integration times were increased for optically faint targets by increasing the dimension of the spacecraft raster in Z, stepping in multiples of the detector pixel pitch so as to ensure that one row of the detector was always scanning through the target. This also improved the precision with which the flat field could be determined. Another problem in the detection of faint sources is the level of residual glitches. Here again the P32 technique was beneficial to the detection of faint sources as the inherent rapid sampling and redundancy allowed a deeper deglitch, with an efficient rejection of the longer lived responsivity fluctuations which often follow glitch events.

All galaxies were observed in three broadband filters: the C60 and C100 filters on the C100 detector and the C160 filter (which actually has a reference wavelength of 170 μm) on the C200 detector. The C100 filter was chosen in preference to the somewhat more sensitive C90 filter as it provided a more direct comparison with the *IRAS* 100 μm observations of the brighter galaxies in the sample. This was useful as a check of the calibration (see § 5). The observations of some galaxies were repeated as a result of operational problems or severe detector instabilities induced by radiation hits. In such cases only the data set of highest quality was used.

A total of 61 of the 63 galaxies were observed in the period 1996 May–July. The remaining two galaxies were observed in 1997 November. A summary of the basic observational parameters for each target is given in Table 2.

4. DATA REDUCTION

Data were reduced using procedures specifically developed for the analysis of data taken in the "P32" Astronomical Observing Template. These procedures are fully described by R. J. Tuffs & C. Gabriel (2002, in preparation); here we only outline the major aspects relevant to the present analysis of the Virgo Cluster galaxy data. The most

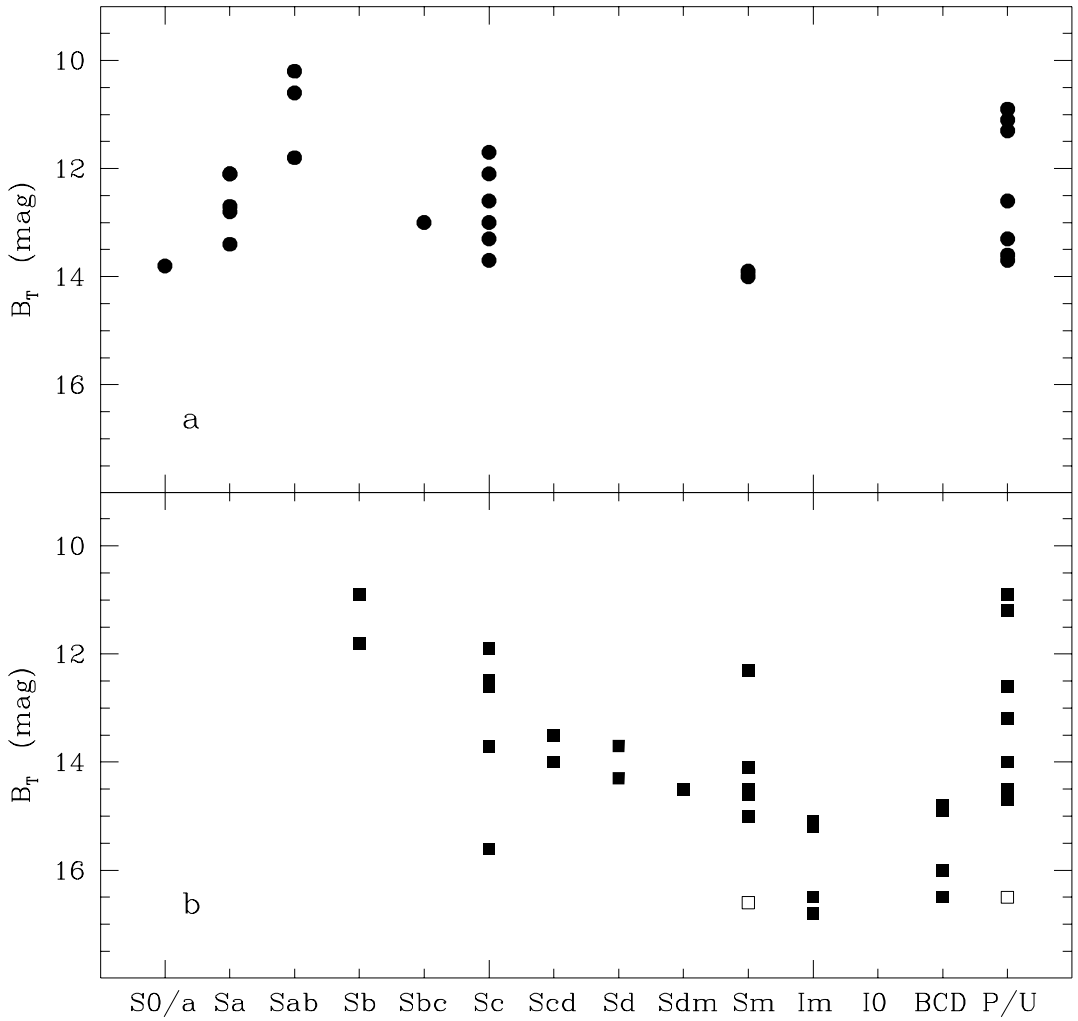

FIG. 2.—Galaxy bivariate distribution in the plane defined by morphological type and total apparent magnitude B_T, as listed in the VCC, for (*a*) the core subsample and (*b*) the periphery subsample. In each panel, the last morphological bin "P/U" contains either peculiar galaxies or objects of uncertain morphology. Circles and squares denote objects in the core and periphery subsamples, respectively. Open squares denote galaxies in the cluster periphery subsample not observed by ISOPHOT (see text).

important functionality of this new software is the correction of the transient response behavior of the Ge:Ga photoconductor detectors of ISOPHOT. As we show below in the context of the present observations, failure to correct for this effect in data taken in the "P32" mode can give rise to serious signal losses and distortions in the derived brightness profiles through the galaxies.

In this paper the data reduction was made outside of the standard PIA (ISOPHOT Interactive Analysis package; Gabriel et al. 1997) program. However, most of the basic operations needed for a photometric calibration of ISOPHOT data (dark current subtraction, correction for integration ramp and signal nonlinearity effects, the reset interval correction, and the conversion of engineering units in V s^{-1} into astronomical units of MJy sr^{-1}) utilized subroutines and calibration data sets taken from the standard PIA package. The only exception was the correction for vignetting (see R. J. Tuffs & C. Gabriel 2002, in preparation). In this work, the calibration is based on the V8.1 release of PIA. There were three principle steps involved in the reduction of "P32" data of the Virgo galaxies: signal conditioning, transient correction, and calculation of calibrated transient-corrected maps.

4.1. *Signal Conditioning*

The first step, which is a noniterative process applied individually to each detector pixel, is signal conditioning. This aimed to provide a signal time line in engineering units free of certain instrumental artifacts, but retaining the complete signature of the transient response of the detector pixel to the illumination history at the full time resolution of the input data. At this stage, the data were corrected for integration ramp nonlinearity effects, and an orbit-dependent dark current was removed. The signal nonlinearity correction was not applied prior to the responsivity drift correction.

Information on the actual pointing history of the spacecraft during the observation was extracted and interpolated to the time of each elementary data sample taken during the galaxy observation. This was used to define a rectangular grid of pointing directions on the sky covered by the occurring combinations of chopper and spacecraft pointing positions. Here the grid spacing was chosen such that the pointing directions were within typically 1″ of the center of each grid pixel. As the grid pixels are ~15″ and 31″ wide in the spacecraft Y coordinate, this removes any need for interpolation or gridding functions when making maps of the

TABLE 2

LOGBOOK OF THE OBSERVATIONS

VCC	TDT[a]	Filter	Raster[b] $N_Y \times N_Z$	α(2000.0)	δ(2000.0)	θ^c (deg)	T_{int}[d] (s)
1.....	22500605	C60	2 × 3	12 08 20.02	13 41 00.2	21.42	864
	22500605	C100	2 × 3	12 08 20.02	13 41 00.2	21.42	864
	22500606	C160	3 × 2	12 08 20.02	13 41 00.2	21.39	328
17.....	22500607	C60	2 × 3	12 10 01.87	14 21 42.5	21.36	864
	22500607	C100	2 × 3	12 10 01.87	14 21 42.5	21.45	864
	22500608	C160	3 × 2	12 10 01.87	14 21 42.5	21.35	328
24.....	23501521	C60	2 × 3	12 10 36.15	11 45 36.6	19.77	864
	23501521	C100	2 × 3	12 10 36.15	11 45 36.6	19.69	864
	23501522	C160	3 × 2	12 10 36.15	11 45 36.6	19.76	328
66.....	23501529	C60	6 × 1	12 12 46.87	10 52 06.9	20.07	820
	23501529	C100	6 × 1	12 12 46.87	10 52 06.9	20.10	820
	23501530	C160	6 × 1	12 12 46.87	10 52 07.0	20.09	328
81.....	22500609	C60	2 × 3	12 13 26.18	14 46 19.3	21.36	864
	22500609	C100	2 × 3	12 13 26.18	14 46 19.2	21.32	864
	22500610	C160	4 × 2	12 13 26.18	14 46 19.3	21.41	378
87.....	22500611	C60	2 × 3	12 13 40.52	15 27 13.2	21.33	864
	22500611	C100	2 × 3	12 13 40.52	15 27 13.2	21.43	864
	22500612	C160	4 × 2	12 13 40.52	15 27 13.2	21.27	378
92.....	22500619	C60	6 × 1	12 13 48.34	14 54 07.1	21.42	820
	22500619	C100	6 × 1	12 13 48.34	14 54 07.0	21.43	820
	22500620	C160	6 × 1	12 13 48.34	14 54 07.1	21.40	304
130.....	22500443	C60	2 × 3	12 15 04.23	09 45 13.6	22.31	1056
	22500443	C100	2 × 3	12 15 04.23	09 45 13.6	22.23	1056
	22500444	C160	3 × 2	12 15 04.23	09 45 13.6	22.27	424
152.....	22500445	C60	3 × 1	12 15 31.21	09 35 07.6	22.28	768
	22500445	C100	3 × 1	12 15 31.21	09 35 07.6	22.30	768
	22500446	C160	3 × 2	12 15 31.21	09 35 07.7	22.31	328
159.....	22500433	C60	2 × 3	12 15 41.50	08 17 07.7	22.47	864
	22500433	C100	2 × 3	12 15 41.50	08 17 07.7	22.53	864
	22500434	C160	3 × 2	12 15 41.50	08 17 07.7	22.46	328
169.....	22500441	C60	2 × 3	12 15 56.39	09 38 55.8	22.28	1056
	22500441	C100	2 × 3	12 15 56.39	09 38 55.8	22.28	1056
	22500442	C160	3 × 2	12 15 56.39	09 38 55.8	22.32	424
318.....	22500439	C60	2 × 3	12 19 02.91	08 51 26.8	22.45	864
	22500439	C100	2 × 3	12 19 02.91	08 51 26.8	22.46	864
	22500440	C160	3 × 2	12 19 02.91	08 51 26.9	22.46	328
459.....	23402367	C60	2 × 3	12 21 11.46	17 38 15.5	18.54	864
	23402367	C100	2 × 3	12 23 37.65	17 32 28.5	18.69	864
	23402368	C160	3 × 2	12 21 11.46	17 38 15.5	18.49	328
460.....	23402369	C60	5 × 1	12 21 13.18	18 23 03.4	18.29	781
	23402369	C100	5 × 1	12 21 13.18	18 23 03.3	18.29	781
	23402370	C160	5 × 1	12 21 13.18	18 23 03.4	18.29	283
655.....	23402365	C60	3 × 1	12 23 37.65	17 32 28.5	18.69	768
	23402365	C100	3 × 1	12 23 37.65	17 32 28.5	18.68	768
	23402366	C160	4 × 2	12 23 37.65	17 32 28.5	18.67	378
664.....	22500181	C60	3 × 2	12 23 44.26	12 28 40.6	22.32	967
	22500181	C100	3 × 2	12 23 44.26	12 28 40.6	22.30	967
	22500182	C160	4 × 2	12 23 44.26	12 28 40.7	22.32	378
666.....	23402359	C60	2 × 3	12 23 46.13	16 47 28.6	18.96	1056
	23402359	C100	2 × 3	12 23 46.13	16 47 28.6	18.88	1056
	23402360	C160	3 × 2	12 23 46.13	16 47 28.6	18.91	424
692.....	22500179	C60	4 × 1	12 24 01.68	12 12 16.6	22.37	806
	22500179	C100	4 × 1	12 24 01.68	12 12 16.7	22.38	806
	22500180	C160	3 × 2	12 24 01.68	12 12 16.8	30.65	328
836.....	22500183	C60	4 × 1	12 25 45.91	12 39 41.5	22.40	806
	22500183	C100	4 × 1	12 25 45.91	12 39 41.5	22.40	806
	22500184	C160	5 × 1	12 25 45.91	12 39 41.4	22.41	283
848.....	22500207	C60	2 × 3	12 25 52.78	05 48 29.5	22.92	864
	22500207	C100	2 × 3	12 25 52.78	05 48 29.5	22.90	864
	22500208	C160	4 × 2	12 25 52.78	05 48 29.5	22.96	378
857.....	23402363	C60	5 × 1	12 25 55.94	18 12 47.4	18.62	821
	23402363	C100	5 × 1	12 25 55.94	18 12 47.4	18.64	821
	23402364	C160	6 × 1	12 25 55.94	18 12 47.4	18.63	328
873.....	22500191	C60	3 × 1	12 26 06.82	13 06 47.5	22.37	768

TABLE 2—*Continued*

VCC	TDT[a]	Filter	Raster[b] $N_Y \times N_Z$	α(2000.0)	δ(2000.0)	θ^c (deg)	T_{int}[d] (s)
	22500191	C100	3 × 1	12 26 06.82	13 06 47.5	22.37	768
	22500192	C160	5 × 1	12 26 06.81	13 06 47.4	22.35	283
890.....	22500205	C60	2 × 3	12 26 20.86	06 40 05.7	22.87	864
	22500205	C100	2 × 3	12 26 20.86	06 40 05.7	22.95	864
	22500206	C160	3 × 2	12 26 20.86	06 40 05.7	22.92	328
912.....	22500185	C60	4 × 1	12 26 32.06	12 36 41.7	22.42	806
	22500185	C100	4 × 1	12 26 32.06	12 36 41.7	22.43	806
	22500186	C160	4 × 1	12 26 32.06	12 36 41.7	22.43	278
971.....	22500209	C60	4 × 1	12 27 09.53	05 52 48.1	22.96	806
	22500209	C100	4 × 1	12 27 09.53	05 52 48.0	22.98	806
	22500210	C160	3 × 1	12 27 09.53	05 52 48.0	22.92	253
984.....	22500187	C60	3 × 2	12 27 14.00	12 44 06.3	22.44	967
	22500187	C100	3 × 2	12 27 14.00	12 44 06.2	22.45	967
	22500188	C160	3 × 1	12 27 14.00	12 44 06.1	22.43	253
1001.....	61300103	C100	2 × 3	12 27 24.65	13 43 00.3	16.30	1104
	61300104	C160	3 × 2	12 27 24.65	13 43 00.3	16.33	668
1002.....	22500217	C60	4 × 1	12 27 26.27	06 15 42.3	22.94	806
	22500217	C100	4 × 1	12 27 26.27	06 15 42.2	22.94	806
	22500218	C160	4 × 1	12 27 26.27	06 15 42.2	22.96	278
1003.....	22500175	C60	5 × 1	12 27 26.21	11 06 30.1	22.61	781
	22500175	C100	5 × 1	12 27 26.21	11 06 30.3	22.62	781
	22500176	C160	5 × 1	12 27 26.20	11 06 30.2	22.61	303
1043.....	22500189	C60	10 × 1	12 27 45.72	13 00 30.3	22.45	976
	22500189	C100	10 × 1	12 27 45.72	13 00 30.3	22.44	976
	22500190	C160	9 × 1	12 27 45.72	13 00 30.3	22.43	367
1047.....	22500173	C60	2 × 3	12 27 53.62	12 17 36.5	22.53	864
	22500173	C100	2 × 3	12 27 53.62	12 17 36.5	22.49	864
	22500174	C160	3 × 1	12 27 53.62	12 17 36.4	22.50	253
1110.....	23402371	C60	6 × 1	12 28 29.47	17 05 06.8	19.07	1168[e]
	23402371	C100	6 × 1	12 28 29.47	17 05 06.7	19.03	1168[e]
	23402372	C160	5 × 1	12 28 29.47	17 05 06.7	19.05	897[e]
1121.....	61600117	C100	2 × 3	12 28 41.77	11 07 54.8	16.73	1104
	61600118	C160	3 × 2	12 28 41.74	11 07 54.9	16.74	668
1158.....	19900549	C60	4 × 2	12 29 03.01	13 11 07.2	28.97	983[e]
	19900549	C100	4 × 2	12 29 03.01	13 11 07.1	28.96	983[e]
	19900550	C160	4 × 1	12 29 03.00	13 11 07.0	28.96	278[e]
1189.....	22500201	C60	2 × 3	12 29 28.53	06 46 19.3	22.99	864
	22500201	C100	2 × 3	12 29 28.53	06 46 19.3	22.95	864
	22500202	C160	4 × 2	12 29 28.53	06 46 19.3	22.98	378
1196.....	19900545	C60	2 × 3	12 29 31.05	14 02 55.3	29.29	864[e]
	19900545	C100	2 × 3	12 29 31.05	14 02 55.3	29.25	864[e]
	19900546	C160	3 × 2	12 29 31.05	14 02 55.3	29.25	328[e]
1217.....	22500177	C60	2 × 3	12 29 43.44	11 24 07.5	22.78	864
	22500177	C100	2 × 3	12 29 43.44	11 24 07.4	22.84	864
	22500178	C160	4 × 2	12 29 43.44	11 24 07.5	22.70	378
1253.....	19900547	C60	5 × 1	12 30 02.87	13 38 07.5	29.20	821[e]
	19900547	C100	5 × 1	12 30 02.87	13 38 07.5	29.19	821[e]
	19900548	C160	5 × 1	12 30 02.86	13 38 07.5	29.17	328[e]
1326.....	22500335	C60	3 × 1	12 30 57.15	11 29 02.0	22.66	768
	22500335	C100	3 × 1	12 30 57.15	11 29 02.0	22.66	768
	22500336	C160	3 × 1	12 30 57.15	11 29 02.0	22.66	253
1368.....	22500333	C60	2 × 3	12 31 32.49	11 37 26.5	22.62	864
	22500333	C100	2 × 3	12 31 32.49	11 37 26.5	22.60	864
	22500334	C160	4 × 1	12 31 32.49	11 37 26.4	22.69	278
1379.....	23402683	C60	3 × 1	12 31 39.43	16 51 14.5	19.26	768
	23402683	C100	3 × 1	12 31 39.43	16 51 14.4	19.27	768
	23402684	C160	3 × 1	12 31 39.43	16 51 14.4	19.26	253
1410.....	23402681	C60	2 × 3	12 32 03.42	16 41 14.8	19.33	864
	23402681	C100	2 × 3	12 32 03.42	16 41 14.8	19.36	864
	23402682	C160	3 × 2	12 32 03.42	16 41 14.8	19.32	328
1412.....	22500331	C60	5 × 1	12 32 05.53	11 10 38.7	22.73	821
	22500331	C100	5 × 1	12 32 05.53	11 10 38.7	22.73	821
	22500332	C160	6 × 1	12 32 05.53	11 10 38.7	22.75	328
1419.....	19900551	C60	2 × 2	12 32 10.56	13 25 14.8	29.38	839[e]
	19900551	C100	2 × 2	12 32 10.56	13 25 14.8	29.35	839[e]

TABLE 2—*Continued*

VCC	TDT[a]	Filter	Raster[b] $N_Y \times N_Z$	α(2000.0)	δ(2000.0)	θ[c] (deg)	T_{int}[d] (s)
	19900552	C160	4 × 1	12 32 10.56	13 25 14.7	29.35	278[e]
1450	19900561	C60	3 × 1	12 32 42.21	14 02 57.1	29.50	768[e]
	19900561	C100	3 × 1	12 32 42.21	14 02 57.2	29.55	768[e]
	19900562	C160	5 × 1	12 32 42.21	14 02 57.1	29.56	303[e]
1552	19900553	C60	4 × 1	12 34 15.87	13 04 34.0	29.43	806[e]
	19900553	C100	4 × 1	12 34 15.87	13 04 34.0	29.43	806[e]
	22600876	C160	5 × 1	12 34 15.86	13 04 34.0	22.42	303[e]
1554	22500213	C60	3 × 1	12 34 19.41	06 28 10.1	23.05	768
	22500213	C100	3 × 1	12 34 19.41	06 28 10.1	23.08	768
	22500214	C160	4 × 1	12 34 19.41	06 28 10.0	23.09	262
1569	19900543	C60	2 × 3	12 34 31.38	13 30 22.3	29.64	864[e]
	19900543	C100	2 × 3	12 34 31.38	13 30 22.3	29.56	864[e]
	19900544	C160	3 × 2	12 34 31.38	13 30 22.3	29.60	328[e]
1575	22500215	C60	3 × 1	12 34 39.08	07 09 40.4	23.08	768
	22500215	C100	3 × 1	12 34 39.08	07 09 40.4	23.08	768
	22500216	C160	3 × 1	12 34 39.08	07 09 40.3	23.08	253
1581	22500211	C60	2 × 3	12 34 44.63	06 18 10.4	23.10	864
	22500211	C100	2 × 3	12 34 44.63	06 18 10.4	23.15	864
	22500212	C160	3 × 2	12 34 44.63	06 18 10.4	23.12	328
1673/76 ...	22500325	C60	4 × 5	12 36 33.46	11 14 56.6	22.88	1422
	22500325	C100	4 × 5	12 36 33.46	11 14 56.6	22.94	1422
	22500326	C160	8 × 3	12 36 33.46	11 14 56.6	22.93	682
1675	22802737	C60	2 × 3	12 36 34.65	08 03 17.6	22.57	864
	22802737	C100	2 × 3	12 36 34.65	08 03 17.6	22.59	864
	22802738	C160	3 × 2	12 36 34.65	08 03 17.6	22.49	328
1678	22500513	C60	3 × 2	12 36 37.31	06 37 17.6	23.13	967
	22500513	C100	3 × 2	12 36 37.31	06 37 17.6	23.10	967
	22500514	C160	4 × 1	12 36 37.30	06 37 17.5	23.10	278
1686	19900557	C60	3 × 3	12 36 43.87	13 15 29.7	29.73	1164[e]
	19900557	C100	3 × 3	12 36 43.87	13 15 29.7	15.33	1164[e]
	19900558	C160	5 × 1	12 36 43.87	13 15 29.6	29.70	303[e]
1690	19900559	C60	12 × 1	12 36 49.88	13 09 53.7	29.69	1054[e]
	19900559	C100	12 × 1	12 36 49.88	13 09 53.7	29.68	1054[e]
	19900560	C160	10 × 1	12 36 49.88	13 09 53.6	29.69	388[e]
1699	22500511	C60	2 × 3	12 37 02.43	06 55 47.9	23.07	864
	22500511	C100	2 × 3	12 37 02.44	06 55 47.9	23.08	864
	22500512	C160	4 × 2	12 37 02.44	06 55 47.9	23.09	378
1725	22802735	C60	2 × 3	12 37 41.11	08 33 30.4	22.48	864
	22802735	C100	2 × 3	12 37 41.11	08 33 30.4	22.44	864
	22802736	C160	4 × 2	12 37 41.11	08 33 30.5	22.48	378
1726	22500509	C60	2 × 3	12 37 44.38	07 06 12.4	23.20	864
	22500509	C100	2 × 3	12 37 44.38	07 06 12.4	23.20	864
	22500510	C160	4 × 2	12 37 44.38	07 06 12.4	23.12	378
1727	22500329	C60	5 × 1	12 37 43.47	11 49 06.3	22.95	781
	22500329	C100	5 × 1	12 37 43.48	11 49 06.3	22.95	781
	22500330	C160	6 × 1	12 37 43.48	11 49 06.2	22.95	304
1730	22500521	C60	2 × 2	12 37 48.90	05 22 06.5	23.16	839
	22500521	C100	2 × 2	12 37 48.90	05 22 06.5	23.15	839
	22500522	C160	4 × 2	12 37 48.90	05 22 06.5	23.16	378
1750	22500507	C60	2 × 3	12 38 14.98	06 59 42.8	23.18	1056
	22500507	C100	2 × 3	12 38 14.98	06 59 42.8	23.11	1056
	22500508	C160	3 × 2	12 38 14.98	06 59 42.8	23.15	424
1757	22600875	C60	2 × 3	12 38 17.99	13 06 36.8	22.59	864[e]
	22600875	C100	2 × 3	12 38 17.99	13 06 36.8	22.67	864[e]
	19900556	C160	4 × 2	12 38 17.99	13 06 36.8	29.83	378[e]

NOTE.—Units of right ascension are hours, minutes, and seconds, and units of declination are degrees, arcminutes, and arcseconds.

[a] Target dedicated time (TDT) identifier.

[b] Raster pointing pattern (in spacecraft Y and Z).

[c] Position angle (θ) of the spacecraft Y-axis (positive east from north).

[d] On-target integration time (T_{int}).

[e] Repeated observation.

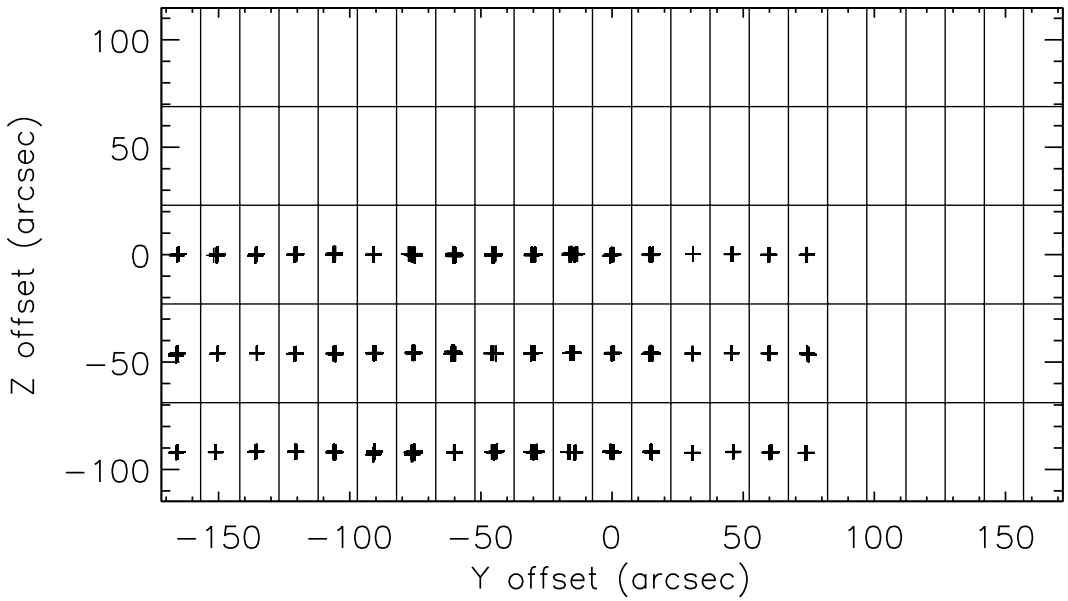

FIG. 3.—Pointing directions observed toward VCC 1 at 60 μm in detector pixel 1. The spacecraft raster dimension was 2×3 in $Y \times Z$. Each pointing direction for 3509 individual data samples for the central pixel of the C100 detector array is plotted as a cross. The rectangular grid is the "P32 natural grid" (see text) for this observation, on which the sky brightness distribution is to be solved. The grid sampling is $14''.94 \times 45''.95$. The registration of chopper and spacecraft pointing and the inherent pointing stability of *ISO* allow the data samples to be typically within $1''$ of the center of each pixel of the P32 natural grid.

sky brightness distribution. We refer to this grid of sky directions as the "P32 natural grid." An example of the actual pointing directions viewed in detector pixel 1 in an observation with the C100 detector is given in Figure 3.

The last part of the signal conditioning was the application of P32 specific deglitching procedures to remove spikes and longer lived fluctuations in detector responsivity from the data time line. The spike detector was operated individually on the residuals of the data remaining on each chopper plateau after fitting a polynomial to preserve the slower varying transient effects. For bright compact sources observed with the C100 detector, there was evidence for spontaneous glitching when the chopper traversed the direction of peak brightness. Since laboratory investigations on Ge:Ga photoconductors (see Sclar 1984) have shown that this glitching should be preserved as signal, a brightness-dependent threshold for the spike detector was employed to prevent serious signal loss through this effect. Lastly, longer lived "tails" in the responsivity of detector pixels, often seen following a spike, were identified and flagged by analyzing the temporal development of the average level of each chopper plateau viewing a particular sky direction on a given spacecraft pointing. This procedure, which utilizes the redundancy afforded by the P32 technique, is the most crucial step determining the instrumental sensitivity, which in the case of the observations of the Virgo galaxies is limited by the degree to which the stochastic undulations in detector responsivity can be removed. In general, removal of these artifacts was virtually complete for the C200 detector but could only partially be achieved for the C100 detector.

4.2. *Transient Correction*

Following signal conditioning, the second major step in the data reduction is transient correction. This is an iterative process to determine the most likely sky brightness distribution giving rise to the observed signal time line. It is a nonlinear optimization problem with the values of sky brightness distribution at each point of the P32 natural grid as variables. Iterations are performed involving successive comparisons between the input data time line and a time line predicted from the convolution of a nonlinear detector model with a trial illumination history derived from a trial sky brightness distribution.

The basis for the solution is the empirical model for the transient behavior of the ISOPHOT C100 and C200 photoconductor detectors described in R. J. Tuffs & C. Gabriel (2002, in preparation). This involves the superposition of two exponentials, each with illumination-dependent time constants. The model also incorporates illumination-dependent jump factors and responsivity coefficients. Each detector pixel has its own constants. As discussed by R. J. Tuffs & C. Gabriel, this model adequately represents the detector response on timescales greater than a few seconds but only approximately describes the so-called hook response. This leads to an overcorrection in the photometry (downward or upward, respectively, for decreasing or increasing illumination steps) when the chopper dwell time is shorter than a few seconds. This was the case for the P32 observations of Virgo galaxies which in almost all cases had chopper dwell times of 0.6 s. Because of the illumination dependence of the detector time constants and jump factors, the effect is more pronounced for decreasing than for increasing illumination steps. For bright sources with a high contrast to the background this induces an asymmetry and a narrowing of the derived brightness profile through a point source compared to the nominal point-spread function. Where this was a blatant effect in the drift-corrected data time line, data were censored out manually.

Figure 4 shows an example of a brightness profile through the faint standard star HR 1654 at 100 μm, for data processing with and without the responsivity correction. The star

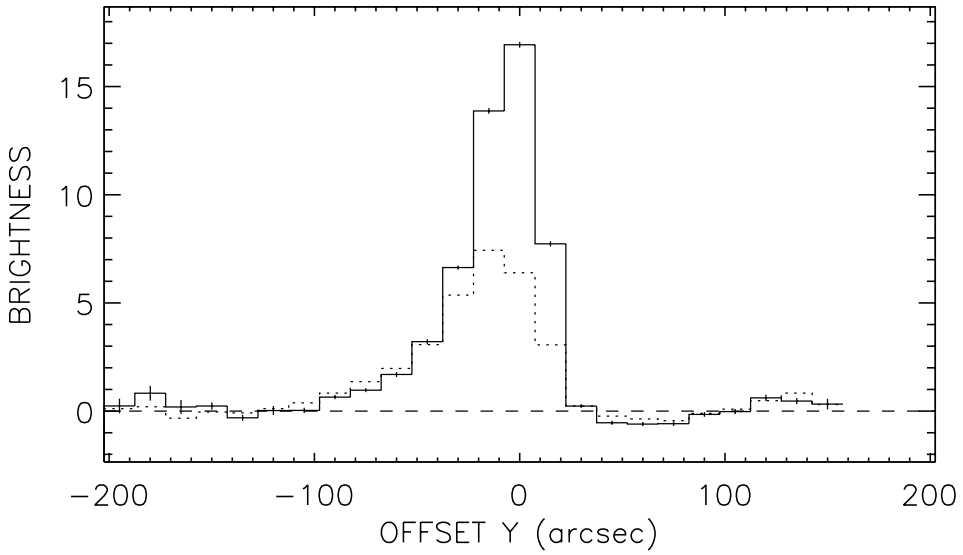

FIG. 4.—Brightness profiles along the *Y* spacecraft scanning direction (raster and chopper scan from right to left) through the standard star HR 1654 at 100 μm. The solid line represents data analyzed in the same manner as the target Virgo Cluster galaxies, while the dotted line represents data with identical processing but without the responsivity drift correction.

has a flux density of 0.52 Jy which would correspond to a medium brightness Virgo galaxy in the sample. Some 95% of the flux density has been recovered by the transient correction procedure. Without the correction some 30% of the integrated emission is missing and 50% of the peak response. The local minimum near 60″ in the *Y* offset is a typical hook response artifact where the algorithm has overshot the true solution after passing through the source. The actual corrections in integrated flux densities for Virgo galaxies depend on the source brightness, the source/background ratio, and the dwell time on each pointing direction, so there is no fixed correction factor for the photometry. As a rule of thumb, though, brighter more compact galaxies have larger corrections than extended faint sources.

The final part of the transient correction procedure is a reassignment of the uncertainties in the photometry. This is done by examining the scatter in the solutions obtained for each chopper plateau and is a measure of the irreproducibility of the solution caused by imperfections in the detector model and/or glitch-induced stochastic undulations in the detector responsivity (which, like the white detector noise, are amplified by the transient correction procedure). This procedure yields a more representative measure of the true random uncertainty in the maps than uncertainties derived from the original fits to the integration ramps.

4.3. *Calculation of Calibrated Transient-corrected Maps*

This last stage in the processing starts with the conversion of the transient-corrected data from V s^{-1} to MJy sr^{-1}. For the Virgo Cluster galaxies the conversion factors were found individually for each galaxy using the average of the responses for each detector pixel to the fine calibration source exposures made before and after each raster in each filter. Thereafter a time-dependent flat field was performed, by examining the time dependence of the detector response to the background directions viewed at the most negative and most positive offsets in *Y* from the map center. A flat sky background emission was assumed. For maps with a single spacecraft raster leg, only a linear time dependence could be fitted. The deeper maps with three scan legs could be fitted with a cubic polynomial.

Maps were made from the transient-corrected, calibrated, and flat-fielded data through a weighted co-addition of the primitive data samples at the full time resolution at each point of the P32 natural grid. Data taken on slews were not used. No gridding function was employed, so that the full angular resolution inherent to the data was preserved. This also means that the measurements at different positions on the map grid are from entirely independent data sets. In cases in which there was full detector pixel redundancy in the C100 array (for faint galaxies with at least three scan legs), the co-addition of the data was done first for individual pixels, producing a map cube of nine maps. Over the region of the P32 natural grid where all nine maps had data, data from the extreme two detector pixels in the map cube were not used when combining data from all pixels. This acted as a further filter for the glitch-induced undulations in the signal which is the major instrumental source of error. However, this artifact could only be partially removed in this fashion. Many of the final maps appear to exhibit spatially correlated noise at a level greater than predicted by a simple error propagation analysis, which we attribute to residual glitch tails in the data enduring over a series of chopper positions.

The final step is the subtraction of the background. This was done by subtracting a tilted plane obtained from a fit to the extremities of the map (external to the extent of the optical galaxy). In principle, this should provide a better statistical measure of the source brightness near the map center than subtracting individual baselines from each map row.

5. EVALUATION OF CALIBRATION

The data reduction procedures outlined in § 4 produced maps of Virgo Cluster galaxies in surface brightness units calibrated on the *ISO* flux scale. When comparing *ISO* data

with those from other observatories, account should be taken of possible systematic variations in the absolute calibration scale. This section compares the *ISO* photometry for the Virgo survey with that from *COBE*-DIRBE and *IRAS*. This is done firstly by statistically comparing the surface brightnesses of the backgrounds measured by ISOPHOT-C with predictions for these backgrounds derived from the *COBE*-DIRBE archives. This provides information about the calibration of surface brightness in each of the ISOPHOT C60, C100, and C160 bands. Secondly, a statistical comparison of integrated flux densities of the target galaxies in the C60 and C100 bands with *IRAS* measurements in the *IRAS* 60 and 100 μm bands is made. This provides information about the calibration of discrete sources. On the basis of the analysis presented below we decided to calibrate the *ISO* data on the *COBE*-DIRBE flux scale. We give the procedure for the conversion of the *ISO* brightnesses to the *COBE*-DIRBE flux scale, as well as conversion factors from *COBE*-DIRBE to the *ISO* and *IRAS* flux scales appropriate for the observations of Virgo Cluster galaxies in the P32 mode.

5.1. *Comparison of ISO and COBE-DIRBE Background Measurements*

Background brightnesses were derived for the 63 VCC galaxies observed by ISOPHOT in each of the *COBE*-DIRBE bands. The procedure adopted was to average pixels on the DIRBE weekly maps in a circle of radius 1°.5 centered on each galaxy, after interpolation to the epoch of each ISOPHOT measurement. The average of these brightnesses was then used to construct a color-corrected SED of the typical background emission encountered in the cluster in the 25, 60, 100, 140, and 240 μm DIRBE bands (Fig. 5).

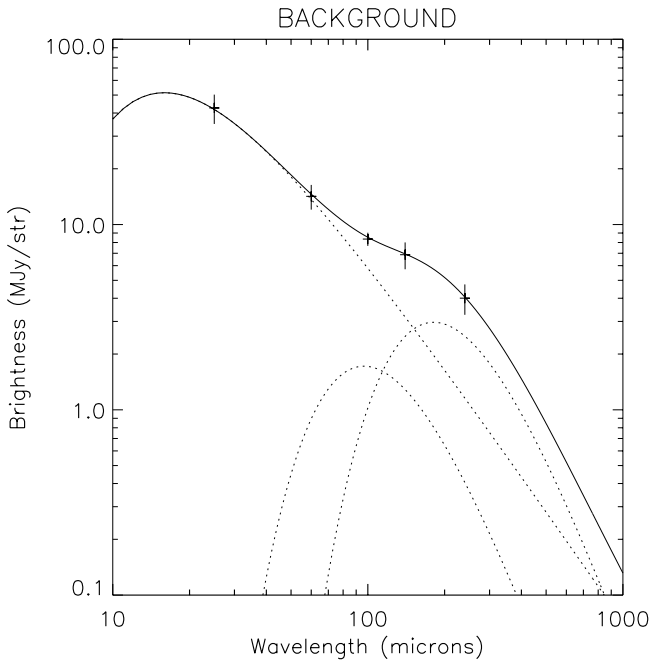

FIG. 5.—SED of the background emission seen toward the positions of the target galaxies, as measured by *COBE*-DIRBE. The vertical bars delineate the 1 σ spread in DIRBE brightnesses measured at the target galaxies, and the horizontal line denotes the average of these measurements. The solid line represents a fit to the average brightnesses composed of the sum of three spectral components denoted by the three dotted curves: a blackbody spectrum with $T = 320$ K for the zodiacal component and modified ($m = 2$) blackbody spectra with $T = 30$ and 16 K for the foreground Galactic dust emission. The DIRBE data were color-corrected according to the fitted SED.

Next, the ISOPHOT measurements of the background toward each galaxy were extracted as weighted averages of the P32 maps outside the region enclosed by the 25.5 mag blue isophote and color-corrected according to the fitted SED of Figure 5. The color-corrected *ISO* backgrounds are plotted versus the color-corrected DIRBE measurements toward each galaxy for each ISOPHOT filter in Figure 6. Though a good correlation is seen between *ISO* and *COBE*-DIRBE at 60 μm, there is a scatter in the ratios, the dispersion becoming more pronounced with increasing wavelength. This might be due either to variations in detector responsivity between different ISOPHOT observations or to the effect of structured Cirrus emission. We believe that the latter is the most likely explanation, as responsivity variations would be expected to affect both the C60 and C100 measurements in equal measure. Furthermore, particularly in the C160 band, measurements with the highest ISOPHOT/DIRBE ratios are those with the largest dispersion in the background signal between different detector pixels, which one would expect when viewing regions of brighter than average structured Cirrus. Thus, the length of the 1 σ bars in the C160 *ISO* versus DIRBE comparison in Figure 6*c* may give an indication of the level of Cirrus confusion in the C160 band.

The systematic differences in the response of ISOPHOT and *COBE*-DIRBE to the backgrounds are summarized in Table 3. The third column of the table gives brightness values for the fit (Fig. 5) to the mean background, interpolated to the reference wavelengths of the ISOPHOT C60, C100, and C160 filters. The fourth column gives the mean of the ratios of the color-corrected responses of the two instruments to the backgrounds.

Prior to further analysis all *ISO* data were multiplied by factors of 1.016, 1.185, and 0.885 in the C60, C100, and C160 bands, respectively, in order to bring the *ISO* measurements onto the *COBE* flux scale. This was done primarily because of the remaining intrinsic uncertainties in the absolute *ISO* calibration. In particular, uncertainties in the ramp nonlinearity correction for short reset intervals make this approach almost unavoidable. The adoption of the *COBE* flux scale also provides a basis for cross calibrating the C100 and C160 detectors, since the spectral coverage of the DIRBE instrument encompasses that of ISOPHOT. The adoption of the *COBE*-DIRBE flux scale raises appreciably the 100/170 color temperature of the galaxies in the survey compared with the pure *ISO* calibration.

This procedure based on the respective responses of *ISO* and *COBE*-DIRBE to a smooth background does not necessarily imply a correct adoption of the *COBE*-DIRBE flux scale for discrete sources. In common with the flux scales of *IRAS* and *COBE*-DIRBE, the *ISO* flux scale is fundamentally based on staring observations of pointlike sources (stars, asteroids, and planets in the case of ISOPHOT-C), which are subsequently converted into a calibration of surface brightness using measured values for the beam solid angles. To check the validity of the conversion of the *ISO* flux scale to the *COBE*-DIRBE flux scale, as described above, a comparison was made between the response of *ISO* and *IRAS* to bright Virgo Cluster galaxies in their respective 60 and 100 μm bandpasses.

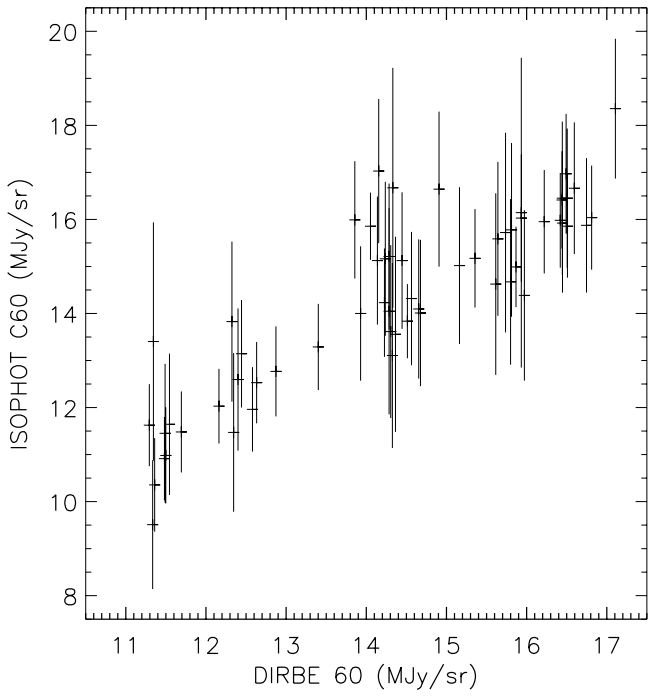

FIG. 6*a*

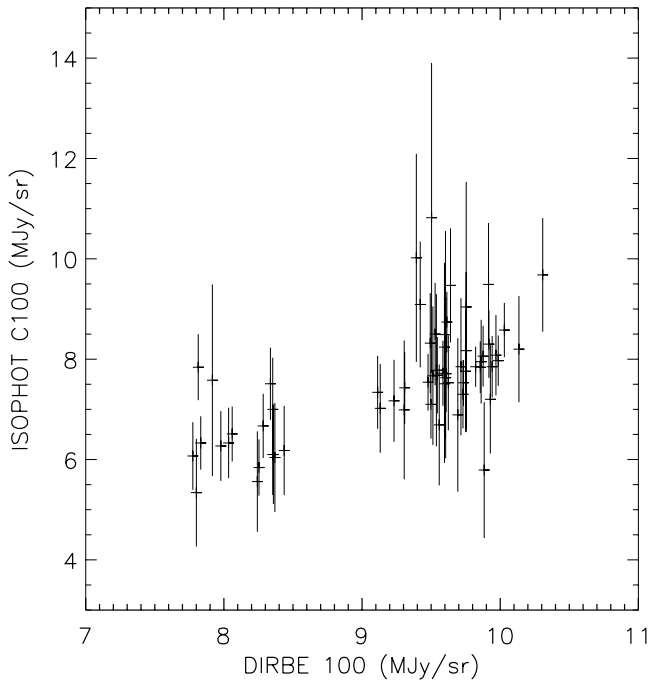

FIG. 6*b*

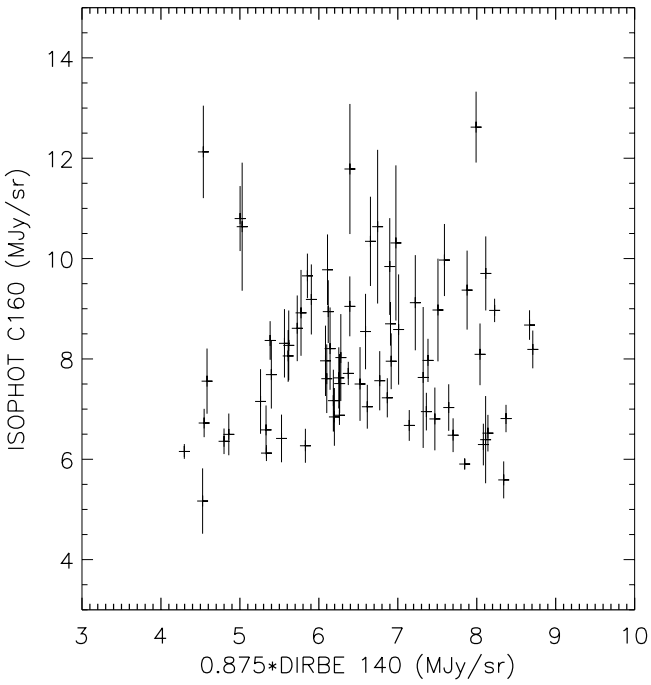

FIG. 6*c*

FIG. 6.—*ISO* backgrounds in the three ISOPHOT filters vs. color-corrected brightnesses derived from DIRBE weekly maps in the 60, 100, and 140 μm bands toward the positions of each target galaxy. The DIRBE measurements were interpolated to the epoch of each *ISO* observation. Color corrections were applied according to the fit to the mean DIRBE SED of Fig. 5. For the C160 filter, the DIRBE data were multiplied by 0.875, which is the factor by which the fit to the color-corrected background SED decreases between the DIRBE reference wavelength (140 μm) and the reference wavelength of the C160 filter (170 μm). The vertical bars represent the 1 σ dispersion in the response of individual detector pixels on ISOPHOT-C to the background.

5.2. *Comparison of ISO and IRAS Photometry of Bright Galaxies*

A total of 33 of the 63 galaxies in the *ISO* sample were detected by *IRAS*. Although most of these sources were resolved by *ISO*, they are sufficiently compact (typical IR extent of order of the FWHM of the *ISO* point-spread function) to provide an objective check of the response of the C100 detector to discrete sources. Spatially integrated fluxes were extracted from the *ISO* maps using the fitting procedure described in § 6 and plotted against the *IRAS* values at 60 and 100 μm from Table 1 in Figures 7*a* and 7*b*.

TABLE 3
COMPARISON OF *ISO* AND DIRBE RESPONSE TO THE BACKGROUND

Filter	λ_ref (μm)	Brightness (MJy sr^{-1})	*ISO*/DIRBE
C60	60	14.59	0.984
C100	100	8.54	0.844
C160	170	6.07	1.130

Except for a few bright galaxies, a good linear correlation is seen between the *ISO* and *IRAS* fluxes, consistent with values from the ratio of fluxes measured by *ISO* to those measured by *IRAS* of $ISO/IRAS = 0.95$ and 0.82 at 60 and 100 μm, respectively. The bright galaxies with *ISO*/*IRAS* ratios well below the correlation were extended objects not well covered in the cross-scan direction. In these cases we attribute the shortfall in integrated flux measured by *ISO* to the presence of extended emission outside the perimeter of the *ISO* maps, which could not be fully recovered in the integration of the Gaussian model fits (§ 6).

The mean ratio *ISO*/*IRAS* for the galaxies in our sample corresponds to the response of *ISO* to discrete sources relative to that of *IRAS*, where the *ISO* measurements have been scaled onto the *COBE*-DIRBE flux scale. These ratios for discrete sources can be compared to the ratios *COBE*-DIRBE/*IRAS* for the background, derived using Table IV.D.1 of Wheelock et al. (1994). These background ratios are *COBE*-DIRBE/*IRAS* $= 0.87 \pm 0.05$ and 0.72 ± 0.07 in the 60 and 100 μm bands, respectively. Thus, the ratios for the background *COBE*-DIRBE/*IRAS* are the same (within the statistical uncertainties) as the ratios *ISO*/*IRAS* for discrete sources (0.95 and 0.82, after scaling the *ISO* measurements onto the *COBE*-DIRBE flux scale). This validates the basic assumption used to convert the *ISO* measurements to the *COBE*-DIRBE flux scale, namely, that the scaling factors *COBE*-DIRBE/*ISO* derived from background measurements are also valid for discrete sources.

Finally, we note that Odenwald, Newmark, & Smoot (1998) found the color-corrected ratio *COBE*-DIRBE/*IRAS* for bright galaxies measured by *COBE*-DIRBE to be 0.94 ± 0.12 and 1.13 ± 0.16 in the 60 and 100 μm bands, respectively. A good agreement with the *ISO*/*IRAS* ratios for Virgo galaxies presented here is found in the 60 μm band, but there is a marginal discrepancy in the 100 μm band, where the Odenwald et al. (1998) results would suggest that the *COBE*-DIRBE/*IRAS* response is significantly greater for discrete sources than for the smooth background. We have no explanation for this discrepancy. However, we do not make explicit use of the *COBE*/DIRBE response to discrete sources in converting the *ISO* data to the *COBE*-DIRBE flux scale.

6. EXTRACTION OF PHOTOMETRY

There are two methods to extract the photometry from the data, namely, by integrating the raw background-subtracted maps or by fitting a model to the data and then inte-

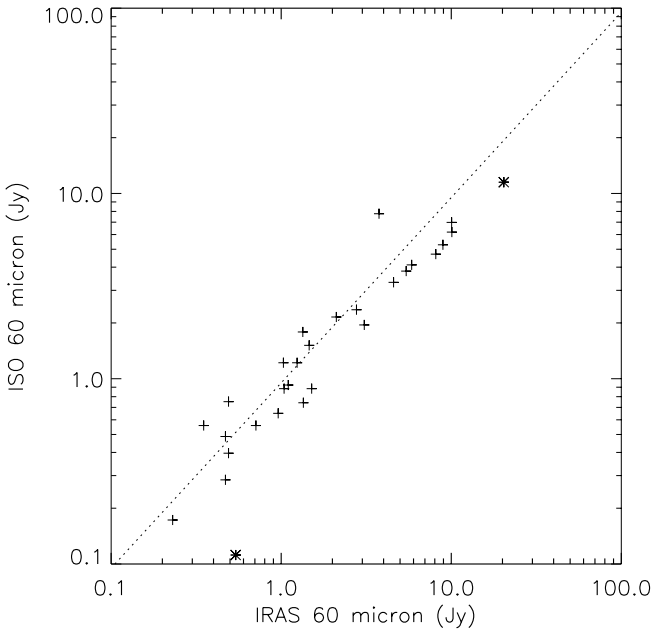

FIG. 7*a*

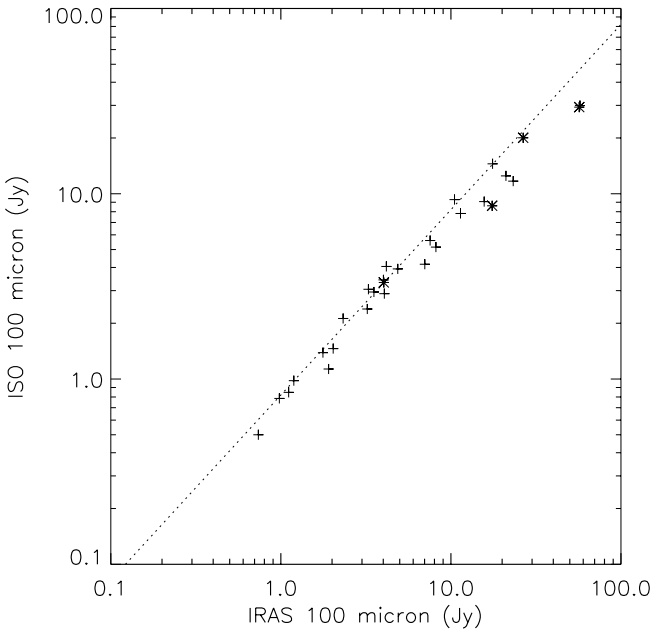

FIG. 7*b*

FIG. 7.—(*a*) Integrated and color-corrected flux densities of galaxies measured in the *ISO* C60 filter vs. integrated and color-corrected flux densities measured by *IRAS* in its 60 μm band. The color correction factors were applied assuming that the SED of the galaxies could be approximated by the superposition of two modified ($m = 2$) Planck curves with temperatures 16 and 30 K with the same relative amplitude as used in Fig. 5 for the fitting of the foreground dust emission from the Milky Way seen toward the Virgo Cluster. (*b*) Same as (*a*), but for the *ISO* C100 filter and the *IRAS* 100 μm band. The *ISO* data represent the spatial integration of Gaussian components fitted as described in § 6 and scaled to the *COBE* flux scale as described in § 5. In each panel the dotted line is not a fit to the correlation but represents the relation (*a*) $ISO/IRAS = 0.95$ and (*b*) $ISO/IRAS = 0.82$ obtained in § 5.2. The asterisks represent the integrated emission on the maps of (*a*) VCC 1253 and VCC 1673 and (*b*) VCC 873, VCC 1379, VCC 1673, and VCC 1690, rather than the integration of the model fits. The galaxies plotted with asterisks have large χ^2 for the model fit (see Table 4).

grating the model to infinity. We applied both methods to our data and show that for this kind of observation the integration of the model to infinity is a more accurate method. Parameters for the model fits are given in Tables 4, 5, and 6. The integrated photometry (for both the integrations of the models and the maps) is given in Table 7.

6.1. *The Integration of the Raw Maps*

The raw integration of the background-subtracted maps has some major disadvantages which make this method less desirable for such analysis. First of all, the raw integration of the map will be affected by noise, especially for low surface brightness objects. Secondly, this method will not take into consideration any emission that was not included in the scan. This would affect mainly large objects and especially galaxies with large disks scanned along the minor axis, where the map covered only the central part of the galaxy. The FIR emission beyond the scan is usually recovered when fitting a model to the data, except for some extreme cases in which the undersampling will also affect the reliability of finding the right parameters for the fit. We nevertheless give flux densities obtained from integration of the raw maps as a first approximation measurement (Table 7).

6.2. *The Integration of the Model Fit*

The model fit to the data is in principle a more accurate method for extracting the photometry, providing the model is a good description of the true brightness distribution. This method also solves the problems related to the integration of the raw maps. In all cases we fitted two-dimensional models to the maps, and all models were Gaussians. However, it was necessary to fit different combinations of models, according to the different morphologies encountered in the sample, such as single Gaussian fit, two Gaussian fit, multicomponent fit, and also a beam fit for pointlike sources. Based on the statistics given by the error analysis, we decided on a case-by-case basis which better fits the data. We adopted the fitting routines from MINUIT (CERN Program Library), which is a tool to find the minimum value of a multiparameter function and analyze the shape of the function around the minimum. This tool is especially suited to handle difficult problems, like those which can be encountered in our two-dimensional maps. It gives very robust results in computing the best-fit parameter values and uncertainties for nonlinear problems, taking into account correlations between parameters. This is important in order to have a reliable estimate of the errors in the fitting parameters, to put upper limits on the nondetection, and to detect the presence of a disk or nuclear component in the fit. The flux densities from integrating the model fit to infinity are listed in Table 7.

6.2.1. *Beam Fit*

The first step in deriving the photometry is to find a good model for the beam and to evaluate any departure between the model and the true beam. In an ideal case one would have an analytical description of the true beam shape and the integration under a fit to the observations of a true point source would give exactly the same flux density as of the real observation. Unfortunately, there is no analytical description of the true shape of the beam. Therefore, we describe the beam on the drift-corrected maps as a two-dimensional circular Gaussian. Because the Gaussian model differs in shape from the true beam profile, the integration to infinity of the best fit to maps is in general systematically different from the true flux densities. To account for this difference, it is necessary to correct the model-integrated fluxes by some correction factor, $f_{\rm corr}$. We refer to this correction as the "beam correction." To determine the value of $f_{\rm corr}$, we fitted simulated noiseless maps of 1 Jy point sources, sampled in exactly the same way as the *ISO* Virgo maps, with circular Gaussians. The widths of these Gaussian beam fit models were $\sigma = 18\farcs56$, $19\farcs95$, and $39\farcs49$ at 60, 100, and 170 μm, respectively, where FWHM $= 2.355\sigma$. In all cases the center of the Gaussian was fixed to the center of the map, such that the only free parameter of the fit was the amplitude of the Gaussian. An example of the model fit to the simulated beams is given in Figure 8. The flux densities obtained from integrating the model fit to infinity were 0.87, 0.84, and 0.87 Jy at 60, 100, and 170 μm, respectively. The flux densities are always below 1 Jy at all three wavelengths, as a result of the differences between the assumed Gaussian model and the simulated beam. Thus, a correction factor was assumed for all flux densities derived from model fits on point sources or on sources which include a pointlike source component. The correction factors were $f_{\rm corr} = 1.149$ at 60 and 170 μm and $f_{\rm corr} = 1.19$ at 100 μm, where the uncorrected flux densities derived from integrating the model fit have to be multiplied with $f_{\rm corr}$.

When fitting real Virgo maps of pointlike sources with two-dimensional circular Gaussians, we obtained an optimum width for the beam fit model of $\sigma = 17\farcs41$ at both 60 and 100 μm. The differences between these fit parameters and those obtained for simulated beams are due to the distortions induced in the beam profile by the responsivity drift correction procedure (see § 4.2). For a few cases we found the need to model the beam with a Gaussian having even a smaller width, $\sigma = 15\farcs41$ at 60 and 100 μm. The latter cases are indicated in all tables with the comment "Modified beam." The effect of decreasing the width of the beam is hardly apparent for the relatively fast C200 detector; therefore, at 170 μm we adopted the same width as for the simulated beams. Throughout this paper we refer to the two-dimensional circular Gaussian model with $\sigma = 17\farcs41$ at 60 and 100 μm and $\sigma = 39\farcs49$ at 170 μm as the "beam fit."

The flux densities derived from integrating the beam fit model to infinity were then multiplied with the beam correction factors derived from the simulated beams. Presumably these correction factors will give only lower limits for the integrated fluxes, as a result of the change in the width of the derived profiles at 60 and 100 μm. However, we expect the difference between the correction factors derived from simulated beams and the true correction factors which would need to be applied on real observations to be smaller than other uncertainties in the photometry, and we make no attempt to correct for this effect.

The beam fit was utilized for a few galaxies which appeared as point sources and was also utilized as a way of deriving upper limits for all our nondetections. All such cases are commented as either "Beam fit" or "Beam fit; nondetection" in the listing of fit parameters in Table 4. For all the other cases the data were fitted by a model which was convolved with the beam fit model. Model fits to the observed brightness profiles of all the Virgo galaxies from our sample are presented in Figure 9. The brightness scale has been transformed to the *COBE*-DIRBE scale as described in § 5.

TABLE 4

THE FITTING PARAMETERS

		One Gaussian Fit			Two Gaussian Fit						
VCC	λ (μm)	S (MJy sr^{-1})	$\epsilon(S)$ (MJy sr^{-1})	σ[a] (arcsec)	S_n[b] (MJy sr^{-1})	$\epsilon(S_n)$ (MJy sr^{-1})	S_d[c] (MJy sr^{-1})	$\epsilon(S_d)$ (MJy sr^{-1})	σ_d[d] (arcsec)	χ^2	Comments
1.....	60	2.05	0.33	4.38	...	...	...	...	...	0.70	
	100	2.39	0.31	9.87	...	...	...	...	...	0.52	
	170	0.79	0.11	52.19	...	...	...	...	...	0.59	
17.....	60	0.85	0.29	...	...	...	...	...	...	0.79	Beam fit; nondetection
	100	0.21	0.27	...	...	...	...	...	...	0.47	Beam fit; nondetection
	170	0.01	0.10	...	...	...	...	...	...	0.40	Beam fit; nondetection
24.....	60	0.68	0.31	...	...	...	...	...	...	0.59	Beam fit; nondetection
	100	0.79	0.29	...	...	...	...	...	...	0.25	Beam fit; nondetection
	170	0.47	0.13	0.09	...	...	...	...	...	0.24	
66.....	60	...	...	...	...	...	...	...	...	...	Multicomponent fit[e]
	100	...	...	...	...	...	...	...	...	...	Multicomponent fit[e]
	170	20.76	0.21	68.58	...	...	...	...	...	3.10	
81.....	60	0.26	0.27	...	...	...	...	...	...	0.57	Beam fit; nondetection
	100	0.18	0.24	...	...	...	...	...	...	0.33	Beam fit; nondetection
	170	1.12	0.09	59.96	...	...	...	...	...	0.70	
87.....	60	1.97	0.47	...	...	...	...	...	...	0.86	Beam fit
	100	2.82	0.46	...	...	...	...	...	...	0.47	Beam fit
	170	1.46	0.09	0.02	...	...	...	...	...	1.58	
92.....	60	...	...	...	57.05	2.12	9.43	1.26	53.53	0.21	
	100	...	...	...	65.93	3.76	27.46	1.12	72.67	0.90	
	170	42.39	0.53	117.29	...	...	...	...	...	0.20	
130.....	60	−0.42	0.34	...	...	...	...	...	...	0.54	Beam fit; nondetection
	100	1.23	0.32	0.07	...	...	...	...	...	0.28	
	170	0.31	0.08	5.26	...	...	...	...	...	0.31	
152.....	60	28.41	1.15	14.41	...	...	...	...	...	0.21	
	100	...	...	...	78.35	2.07	2.62	0.55	80.90	0.02	
	170	...	...	...	20.58	0.33	1.92	0.24	135.66	0.40	
159.....	60	0.22	0.27	...	...	...	...	...	...	0.43	Beam fit; nondetection
	100	0.11	0.27	...	...	...	...	...	...	0.29	Beam fit; nondetection
	170	0.60	0.10	...	...	...	...	...	...	0.76	Beam fit[f]
169.....	60	0.32	0.19	...	...	...	...	...	...	0.63	Beam fit; nondetection
	100	−0.13	0.34	...	...	...	...	...	...	0.34	Beam fit; nondetection
	170	−0.02	0.07	...	...	...	...	...	...	0.66	Beam fit; nondetection
318.....	60	2.84	0.31	0.01	...	...	...	...	...	0.65	
	100	3.02	0.29	27.29	...	...	...	...	...	0.16	
	170	2.60	0.12	33.87	...	...	...	...	...	0.53	
459.....	60	2.12	0.35	13.49	...	...	...	...	...	0.87	
	100	5.18	0.36	17.17	...	...	...	...	...	0.44	
	170	1.95	0.13	6.05	...	...	...	...	...	0.27	
460.....	60	62.62	1.71	11.41	...	...	...	...	...	0.72	Modified beam[g]
	100	...	...	...	121.00	4.06	8.51	0.53	77.18	0.20	Modified beam[g]
	170	...	...	...	26.08	1.92	5.49	1.23	78.65	0.18	
655.....	60	7.51	0.58	5.34	...	...	...	...	...	0.49	
	100	16.66	0.63	9.18	...	...	...	...	...	0.25	
	170	18.57	0.12	13.59	...	...	...	...	...	1.59	
664.....	60	...	...	...	6.14	0.76	1.31	0.43	52.38	0.88	
	100	...	...	...	5.90	0.93	2.67	0.72	34.38	0.76	
	170	3.75	0.10	0.01	...	...	...	...	...	0.78	
666.....	60	−0.50	0.20	...	...	...	...	...	...	1.08	Beam fit; nondetection
	100	0.35	0.20	...	...	...	...	...	...	0.41	Beam fit; nondetection
	170	−0.10	0.06	...	...	...	...	...	...	0.55	Beam fit; nondetection
692.....	60	7.11	0.51	15.56	...	...	...	...	...	0.81	
	100	...	...	...	13.70	1.29	3.45	1.00	39.81	0.78	
	170	...	...	...	7.54	0.20	0.82	0.14	144.89	2.13	
836.....	60	...	...	...	86.91	5.07	38.71	3.57	32.21	0.89	Modified beam[g]
	100	...	...	...	204.30	8.46	78.11	4.57	32.64	0.63	Modified beam[g]
	170	40.72	0.74	25.63	...	...	...	...	...	1.29	

TABLE 4—*Continued*

		One Gaussian Fit			Two Gaussian Fit						
VCC	λ (μm)	S (MJy sr^{-1})	$\epsilon(S)$ (MJy sr^{-1})	σ[a] (arcsec)	S_n[b] (MJy sr^{-1})	$\epsilon(S_n)$ (MJy sr^{-1})	S_d[c] (MJy sr^{-1})	$\epsilon(S_d)$ (MJy sr^{-1})	σ_d[d] (arcsec)	χ^2	Comments
848.....	60	0.45	0.27	...	...	...	...	...	...	0.64	Beam fit; nondetection
	100	0.81	0.25	0.05	...	...	...	...	...	0.30	
	170	...	...	...	0.75	0.16	0.48	0.10	137.07	0.44	
857.....	60	5.99	0.48	20.77	...	...	...	...	...	0.59	
	100	...	...	...	6.07	1.25	9.26	0.58	41.14	1.43	Modified beam[g]
	170	14.83	0.35	42.38	...	...	...	...	...	0.20	
873.....	60	32.98	0.73	34.57	...	...	...	...	...	1.00	
	100	...	...	...	...	...	...	...	...	...	Poor fit
	170	49.50	0.80	41.03	...	...	...	...	...	1.92	
890.....	60	0.40	0.27	...	...	...	...	...	...	0.62	Beam fit; nondetection
	100	0.38	0.24	...	...	...	...	...	...	0.41	Beam fit; nondetection
	170	0.37	0.12	18.77	...	...	...	...	...	0.28	
912.....	60	12.14	0.61	13.66	...	...	...	...	...	1.19	
	100	...	...	...	18.34	2.15	8.87	1.67	34.65	0.62	
	170	10.04	0.34	22.81	...	...	...	...	...	0.22	
971.....	60	4.53	0.39	17.38	...	...	...	...	...	0.67	
	100	10.62	0.46	24.39	...	...	...	...	...	0.60	
	170	4.29	0.29	33.38	...	...	...	...	...	0.14	
984.....	60	0.06	0.30	...	...	...	...	...	...	0.52	Beam fit; nondetection
	100	0.20	0.32	...	...	...	...	...	...	0.28	Beam fit; nondetection
	170	−0.15	0.24	...	...	...	...	...	...	0.23	Beam fit; nondetection
1001...	60	...	...	...	...	...	...	...	...	...	Not observed
	100	−0.05	0.14	...	...	...	...	...	...	0.69	Beam fit; nondetection
	170	0.52	0.06	42.32	...	...	...	...	...	0.73	
1002...	60	10.72	0.52	17.78	...	...	...	...	...	0.81	
	100	...	...	...	16.78	1.45	11.98	0.87	34.65	0.65	
	170	14.84	0.31	30.67	...	...	...	...	...	0.27	
1003...	60	16.25	0.84	5.58	...	...	...	...	...	0.91	
	100	...	...	...	43.84	1.44	1.98	0.38	108.49	0.20	
	170	12.37	0.24	0.01	...	...	...	...	...	0.54	
1043...	60	43.04	1.41	5.78	...	...	...	...	...	0.60	
	100	...	...	...	89.99	3.09	7.17	0.78	71.48	0.20	
	170	...	...	...	34.40	0.57	2.83	0.21	188.97	0.20	
1047...	60	0.33	0.28	...	...	...	...	...	...	0.84	Beam fit; nondetection
	100	−0.03	0.27	...	...	...	...	...	...	0.48	Beam fit; nondetection
	170	−0.31	0.31	...	...	...	...	...	...	0.22	Beam fit; nondetection
1110...	60	...	...	...	5.72	0.85	2.56	0.41	73.70	0.54	
	100	...	...	...	9.19	1.70	15.77	1.11	42.75	0.20	
	170	18.19	0.30	56.06	...	...	...	...	...	0.20	
1121...	60	...	...	...	...	...	...	...	...	...	Not observed
	100	0.33	0.18	...	...	...	...	...	...	0.26	Beam fit; nondetection
	170	...	...	...	...	...	...	...	...	...	Confusion limited
1158...	60	−0.25	0.31	...	...	...	...	...	...	0.65	Beam fit; nondetection
	100	0.21	0.34	...	...	...	...	...	...	0.32	Beam fit; nondetection
	170	−0.60	0.20	...	...	...	...	...	...	0.42	Beam fit; nondetection
1189...	60	2.53	0.31	16.24	...	...	...	...	...	0.97	
	100	5.93	0.27	18.64	...	...	...	...	...	0.77	
	170	4.20	0.12	11.22	...	...	...	...	...	0.63	
1196...	60	−0.19	0.30	...	...	...	...	...	...	0.33	Beam fit; nondetection
	100	0.20	0.28	...	...	...	...	...	...	0.19	Beam fit; nondetection
	170	...	...	...	...	...	...	...	...	...	Poor fit[h]
1217...	60	−0.03	0.30	...	...	...	...	...	...	0.51	Beam fit; nondetection
	100	0.08	0.26	...	...	...	...	...	...	0.34	Beam fit; nondetection
	170	−0.15	0.09	...	...	...	...	...	...	1.49	Beam fit; nondetection
1253...	60	2.60	0.85	...	...	...	...	...	...	0.62	
	100	9.79	1.07	14.10	...	...	...	...	...	0.35	
	170	3.66	0.29	19.29	...	...	...	...	...	0.43	
1326...	60	...	...	...	34.83	1.30	1.97	0.62	56.51	1.21	

TABLE 4—*Continued*

		One Gaussian Fit			Two Gaussian Fit						
VCC	λ (μm)	S (MJy sr^{-1})	$\epsilon(S)$ (MJy sr^{-1})	σ^{a} (arcsec)	$S_n{}^{b}$ (MJy sr^{-1})	$\epsilon(S_n)$ (MJy sr^{-1})	$S_d{}^{c}$ (MJy sr^{-1})	$\epsilon(S_d)$ (MJy sr^{-1})	$\sigma_d{}^{d}$ (arcsec)	χ^2	Comments
	100	...	...	...	36.85	0.91	1.29	0.18	95.09	0.39	
	170	6.35	0.65	23.84	...	...	...	...	...	0.68	
1368 ...	60	−0.39	1.14	...	...	...	...	...	...	1.14	Beam fit; nondetection
	100	0.41	0.19	...	...	...	...	...	...	0.61	Beam fit; nondetection
	170	0.87	0.21	...	...	...	...	...	...	0.85	Beam fit
1379 ...	60	6.95	0.39	37.76	...	...	...	...	...	1.93	
	100	...	...	...	9.52	1.01	10.59	0.69	51.71	5.84	
	170	13.20	0.41	39.05	...	...	...	...	...	0.87	
1410 ...	60	2.25	0.22	25.45	...	...	...	...	...	1.12	
	100	6.18	0.43	7.63	...	...	...	...	...	0.73	
	170	2.56	0.13	13.24	...	...	...	...	...	0.52	
1412 ...	60	−0.36	0.44	...	...	...	...	...	...	0.93	Beam fit; nondetection
	100	−0.37	0.53	...	...	...	...	...	...	1.11	Beam fit; nondetection
	170	2.41	0.27	27.95	...	...	...	...	...	1.44	Off-center emission
1419 ...	60	1.17	0.36	0.39	...	...	...	...	...	0.64	
	100	3.23	0.42	19.24	...	...	...	...	...	0.53	
	170	1.60	0.26	8.85	...	...	...	...	...	1.31	
1450 ...	60	8.72	0.64	18.28	...	...	...	...	...	0.84	
	100	...	...	...	23.49	1.64	7.86	0.96	39.35	1.31	
	170	11.18	0.37	30.00	...	...	...	...	...	0.23	
1552 ...	60	4.52	1.28	15.31	...	...	...	...	...	0.51	Modified beam[g]
	100	15.53	0.80	19.70	...	...	...	...	...	0.95	Modified beam[g]
	170	6.44	0.42	21.34	...	...	...	...	...	0.45	
1554 ...	60	...	...	...	...	...	...	...	...	...	Multicomponent fit[e]
	100	...	...	...	...	...	...	...	...	...	Multicomponent fit[e]
	170	34.24	0.60	28.55	...	...	...	...	...	0.52	
1569 ...	60	0.66	0.37	...	...	...	...	...	...	0.35	Beam fit; nondetection
	100	0.39	0.34	...	...	...	...	...	...	0.31	Beam fit; nondetection
	170	0.26	0.09	...	...	...	...	...	...	0.30	Beam fit; nondetection
1575 ...	60	17.17	0.71	11.39	...	...	...	...	...	1.25	
	100	...	...	...	24.42	2.32	5.54	1.71	29.78	0.75	
	170	8.40	0.43	25.17	...	...	...	...	...	0.33	
1581 ...	60	0.14	0.24	...	...	...	...	...	...	0.88	Beam fit; nondetection
	100	0.58	0.22	...	...	...	...	...	...	0.59	Beam fit; nondetection
	170	1.22	0.24	7.69	...	...	...	...	...	0.31	
1673 ...	60	...	...	...	...	...	...	...	...	...	
	100	...	...	...	...	...	...	...	...	...	
	170	...	...	...	...	...	...	...	...	...	Multicomponent fit[e]
1675 ...	60	0.80	0.25	14.40	...	...	...	...	...	0.74	
	100	−0.08	0.24	...	...	...	...	...	...	0.41	Beam fit; nondetection
	170	0.60	0.14	6.73	...	...	...	...	...	0.20	
1678 ...	60	1.59	0.32	...	...	...	...	...	...	0.84	Beam fit
	100	2.04	0.26	35.11	...	...	...	...	...	0.37	
	170	1.76	0.30	33.78	...	...	...	...	...	0.27	
1686 ...	60	7.86	1.18	7.09	...	...	...	...	...	0.93	
	100	10.74	0.55	23.35	...	...	...	...	...	0.78	
	170	5.72	0.38	17.39	...	...	...	...	...	0.81	
1690 ...	60	...	...	...	68.43	2.85	8.36	1.21	60.01	0.60	
	100	...	...	...	86.07	5.08	32.24	1.73	63.74	3.79	
	170	59.57	0.65	54.95	...	...	...	...	...	0.20	
1699 ...	60	5.14	0.14	6.26	...	...	...	...	...	0.78	
	100	5.28	0.32	16.19	...	...	...	...	...	0.50	
	170	1.89	0.10	0.03	...	...	...	...	...	0.44	
1725 ...	60	0.93	0.31	...	...	...	...	...	...	0.57	Beam fit
	100	5.11	0.81	6.38	...	...	...	...	...	0.36	
	170	1.88	0.11	0.03	...	...	...	...	...	0.41	
1726 ...	60	0.68	0.35	...	...	...	...	...	...	0.49	Beam fit; nondetection
	100	0.74	0.38	...	...	...	...	...	...	0.38	Beam fit; nondetection

TABLE 4—*Continued*

		One Gaussian Fit			Two Gaussian Fit						
VCC	λ (μm)	S (MJy sr^{-1})	$\epsilon(S)$ (MJy sr^{-1})	σ[a] (arcsec)	S_n[b] (MJy sr^{-1})	$\epsilon(S_n)$ (MJy sr^{-1})	S_d[c] (MJy sr^{-1})	$\epsilon(S_d)$ (MJy sr^{-1})	σ_d[d] (arcsec)	χ^2	Comments
	170	0.94	0.10	0.03	...	...	...	...	...	0.38	
1727...	60	...	...	...	21.36	1.49	11.67	0.77	55.87	2.32	
	100	...	...	...	...	...	...	...	...	...	Multicomponent fit[e]
	170	...	...	...	8.32	1.48	33.81	1.07	84.61	0.20	
1730...	60	...	...	...	14.69	2.25	7.18	1.53	28.46	0.46	Modified beam[g]
	100	...	...	...	31.35	3.19	21.69	2.06	27.14	0.48	Modified beam[g]
	170	...	...	...	16.79	0.97	1.86	0.89	52.01	0.76	
1750...	60	0.17	0.22	...	...	...	...	...	...	0.66	Beam fit; nondetection
	100	0.71	0.22	11.41	...	...	...	...	...	0.42	
	170	0.29	0.08	0.44	...	...	...	...	...	0.19	
1757...	60	1.89	0.23	3.87	...	...	...	...	...	1.69	
	100	6.71	0.24	18.38	...	...	...	...	...	0.99	
	170	3.27	0.13	11.38	...	...	...	...	...	0.29	

Note.—Table 4 is also available in machine-readable form in the electronic edition of the *Astrophysical Journal Supplement*.

[a] The width σ of the major axis of the elliptical Gaussian source model in arcsec, where the total width of the major axis of the fitted Gaussian is $\sigma^2_{\rm total} = \sigma^2 + \sigma^2_{\rm PSF}$. The FWHM of the source model is 2.354σ.

[b] The amplitude S_n of the nuclear component.

[c] The amplitude S_d of the disk component.

[d] The width σ_d of the disk major axis in arcsec, where the total width of the major axis of the fitted Gaussian for the disk component is $\sigma^2_{\rm total} = \sigma^2_d + \sigma^2_{\rm PSF}$.

[e] The parameters for the multicomponent fit are listed in Tables 5 and 6.

[f] VCC 159 shows evidence for faint extended emission at 160 μm, not fitted by the model. We only present a beam fit to the data, resulting in a lower limit for the derived flux.

[g] In some cases it was necessary to consider a narrower width for the beam fit model, namely, $\sigma = 15\farcs41$, FWHM $= 2.355\sigma$ (see § 6.2.1).

[h] VCC 1196 presents evidence for extended asymmetric emission, not fitted by the model. In this case the fluxes were derived only from the integration of the raw maps.

6.2.2. *One Gaussian Fit*

Most of our data were fitted by a two-dimensional elliptical Gaussian, obtained by convolving a model source brightness distribution for each galaxy with a beam fit model, as described in the previous section. The brightness distribution of the source was itself modeled as a two-dimensional elliptical Gaussian, constrained to have the position angle of the major axis as given by the *B*-band isophotal photometry from the VCC. Another constraint was to fix the major to minor axial ratio again from the optical data (the VCC). These constraints were needed because for most of the observations the map extent was only 2 or 3 pixels in the cross-scan direction, and also because of the undersampling problem, which made impossible a reliable determination of the orientation and width of the Gaussian in the cross-scan direction. Such a constraint would nevertheless affect the photometry in cases in which the FIR shape of the galaxies would not follow the optical shape of the galaxy.

The center of the Gaussian was fixed to the actual optical center of the galaxy. This was sometimes slightly offset from the geometrical center of the map as a result of pointing offsets of the telescope. In many cases the optical position within the map proved to be a poor representation of the actual center of the galaxy in the FIR maps. Therefore, an initial fitting routine was used to find the best position of the Gaussians, and this refined position was finally adopted for

TABLE 5

The Fitting Parameters for the Multicomponent Fits

		Main Nuclear/Disk Component					Other Components				
VCC	λ (μm)	$S1_n$[a] (MJy sr^{-1})	$\epsilon(S1_n)$ (MJy sr^{-1})	$S1_d$[b] (MJy sr^{-1})	$\epsilon(S1_d)$ (MJy sr^{-1})	$\sigma 1_d$[c] (arcsec)	$S2$ (MJy sr^{-1})	$\epsilon(S2)$ (MJy sr^{-1})	$\sigma 2$ (arcsec)	χ^2	Comments
66.....	60	8.33	1.35	7.60	0.91	52.40	8.55	0.76	4.63	1.12	
	100	11.47	1.95	18.21	1.11	56.23	5.49	0.91	...	2.21	
1554.....	60	54.22	2.22	10.50	1.10	31.23	24.81	1.64	18.60	4.36	Modified beam[d]
	100	29.57	2.87	27.61	1.51	35.04	28.59	1.72	25.29	10.21	Modified beam[d]
1727.....	100	17.78	4.92	29.78	1.26	43.51	14.61	0.72	59.42	0.15	Modified beam[d]

[a] The amplitude $S1_n$ of the nuclear component.

[b] The amplitude $S1_d$ of the disk component.

[c] The width $\sigma 1_d$ of the disk major axis in arcsec, where the total width of the major axis of the fitted Gaussian for the disk component is $\sigma 1^2_{\rm total} = \sigma 1^2_d + \sigma^2_{\rm PSF}$.

[d] In some cases it was necessary to consider a narrower beam for the fit, namely, a spherical Gaussian with the width $\sigma = 15\farcs41$, FWHM $= 2.355\sigma$ (see § 6.2.1).

TABLE 6
THE FITTING PARAMETERS FOR VCC 1673/VCC 1676

	VCC 1676					VCC 1673					
λ (μm)	$S1_n$ (MJy sr^{-1})	$\epsilon(S1_n)$ (MJy sr^{-1})	$S1_d$ (MJy sr^{-1})	$\epsilon(S1_d)$ (MJy sr^{-1})	$\sigma 1_d$ (arcsec)	$S2_n$ (MJy sr^{-1})	$\epsilon(S2_n)$ (MJy sr^{-1})	$S2_d$ (MJy sr^{-1})	$\epsilon(S2_d)$ (MJy sr^{-1})	$\sigma 2_d$ (arcsec)	χ^2
170	29.45	2.72	54.52	2.03	52.68	57.08	0.63	9.18	0.10	239.00	0.2

the fit. Larger shifts from the optical position were mainly found in the C160 maps, probably as a result of the undersampling of the maps coupled with variation in the responsivity within one map pixel. It is also not unreasonable to consider that parts of the shifts are due to real offsets of the optical from the FIR center of the galaxies. The fitted parameters are the amplitude and the width (σ) of the Gaussian. The parameters of the fit are listed in Table 4.

6.2.3. *Two Gaussian Fit*

In several cases there was evidence for a nuclear component plus a disk component, which we fitted using a superposition between a beam fit model and a two-dimensional elliptical Gaussian convolved with the beam fit model. In this case the position angle and axial ratio of the disk component were again fixed from the optical data, and the fitted parameters were the amplitude of the nuclear component (the beam fit model) and the amplitude and width of the elliptical Gaussian representing the disk. Again the parameters of the fit are listed in Table 4.

6.2.4. *Multicomponent Fit*

In a few cases some morphological features were observed in the maps, and therefore a more sophisticated fit was required. Thus, for VCC 66, the maps at 60 and 100 μm revealed the presence of a peripheral H II region complex, which we had to fit with a third Gaussian. The galaxies VCC 1554 and VCC 1727 also had to be fitted with a third Gaussian, this time to account for extended emission. The galaxies with multicomponent fits are marked in Table 4 as such, and the actual parameters of the fit are given in Table 5.

A special case is the interacting system VCC 1673/VCC 1676. At 60 and 100 μm the observations were twice as finely sampled in the cross-scan direction, resulting in a higher resolution map of the system. These maps could not be fitted by a model, as a result of the detailed morphologies, and are better suited to the direct integration of the raw maps. Therefore, this interacting pair is not included in Figure 9, but rather will be the object of a separate paper. At 170 μm the sky was undersampled in the cross-scan direction in the same way as for the rest of the galaxies, and thus a model including four Gaussians was considered. The parameters of this fit are given separately in Table 6.

6.2.5. *The χ^2 Statistics*

The χ^2 statistics reflects the random errors in the fit, being an indicator of the goodness of the fit. In our case χ^2 is also affected by the undersampling in the cross-scan direction. This effect appears simply because the pixel map is supposed to be uniformly illuminated, while our Gaussian model assumes an illumination variation within the pixel. This will be interpreted as a departure between the data and the fit, resulting in an increased χ^2. For low flux densities the χ^2 will be dominated by the random errors, and the effect of the undersampling is negligible. However, with increasing source brightness χ^2 will start to be dominated by the errors resulting from the undersampling, and thus artificially large numbers of the χ^2 will be obtained. This effect is illustrated in Figure 10 for the flux densities at 60 μm. As expected, for bright sources there is a good linear correlation between the flux densities derived from integrating the model to infinity and the χ^2 of the fit. For faint sources we expect the χ^2 to be dominated by random errors, and thus a scatter diagram is obtained on the left-hand side of the plot. For bright sources the real departure between the Gaussian model and the data is given by the scatter in the linear correlation. Thus, for bright sources, the values of the χ^2 had to be corrected for the undersampling effect. The following correlations were used for the correction:

$$\chi^2 = 0.70F_{\text{model}}\text{–}0.5 \quad \text{at } 60\ \mu\text{m}\,, \tag{1}$$

$$\chi^2 = 0.40F_{\text{model}}\text{–}0.2 \quad \text{at } 100\ \mu\text{m}\,, \tag{2}$$

$$\chi^2 = 0.25F_{\text{model}}\text{–}0.2 \quad \text{at } 170\ \mu\text{m}\,. \tag{3}$$

The values of the χ^2 corrected for the undersampling effect are listed in Table 4 (and in Tables 5 and 6 for the multicomponent fit).

6.2.6. *Upper Limits*

In all cases in which we had nondetections we derived upper limits based on beam fits to the data, on the assumption that the galaxy which escaped detection was a pointlike source. The upper limits are thus the flux densities corresponding to the 3 σ uncertainties in the amplitude of the beam fit model, where the center of the Gaussian model was fixed, as described in the previous section. These cases are marked in Table 4 as "Beam fit; nondetection."

We note that the assumption that the undetected galaxies are pointlike sources may not always be true. For low surface brightness extended galaxies the upper limits obtained with our method could be lower than the actual integrated flux density.

7. DETECTION STATISTICS AND BASIC FIR PROPERTIES OF THE SAMPLE

From the observed 63 galaxies (61 galaxies observed at all three FIR wavelengths and two galaxies observed only at 100 and 170 μm) we have detected 54 (85.7%) galaxies at least at one wavelength and 40 (63.5%) galaxies at all three wavelengths. Nine (14.3%) galaxies were not detected at two

TABLE 7

THE PHOTOMETRY

VCC	λ (μm)	$F_{\rm model}$[a] (Jy)	$\epsilon(F_{\rm model})$ (Jy)	$F_{\rm map}$[b] (Jy)	$\epsilon(F_{\rm map})$ (Jy)	$B_{\rm backgr}$[c] (MJy sr^{-1})	f_B[d]	Notes
1.....	60	0.10	0.02	−0.05	0.06	15.87	0.037	
	100	0.14	0.02	0.21	0.06	8.92	0.042	
	170	0.33	0.05	0.31	0.18	7.46	0.042	
17.....	60	<0.04	...	0.11	0.08	14.80	0.037	
	100	<0.03	...	−0.09	0.08	9.10	0.033	
	170	<0.07	...	0.01	0.19	7.94	0.036	
24.....	60	<0.04	...	0.11	0.06	16.77	0.030	
	100	<0.04	...	−0.08	0.06	9.72	0.043	
	170	0.12	0.03	0.04	0.05	5.42	0.020	
66.....	60	2.47	0.21	2.96	0.30	19.40	0.027	
	100	5.09	0.28	5.32	0.43	11.47	0.039	
	170	11.27	0.03	10.64	0.21	6.02	0.039	
81.....	60	<0.04	...	0.02	0.06	14.84	0.052	
	100	<0.03	...	0.09	0.07	9.09	0.060	
	170	0.77	0.06	0.90	0.23	7.73	0.038	
87.....	60	0.10	0.02	0.10	0.08	14.79	0.034	
	100	0.15	0.02	0.26	0.12	8.50	0.038	
	170	0.38	0.02	0.06	0.11	7.69	0.023	
92.....	60	4.70	0.26	4.64	0.13	16.02	0.036	
	100	11.46	0.38	10.41	0.21	9.86	0.040	
	170	40.29	0.50	26.16	0.41	10.05	0.028	
130.....	60	<0.05	...	0.19	0.05	17.38	0.030	
	100	0.07	0.02	−0.03	0.05	9.30	0.026	
	170	0.08	0.02	0.00	0.14	5.45	0.042	
152.....	60	1.87	0.08	1.98	0.09	17.93	0.025	
	100	5.48	0.29	3.88	0.10	11.25	0.043	
	170	8.38	0.38	6.80	0.21	6.06	0.045	
159.....	60	<0.04	...	−0.00	0.04	16.95	0.023	
	100	<0.04	...	0.02	0.06	9.44	0.021	
	170	0.16	0.03	0.49	0.21	6.12	0.044	
169.....	60	<0.03	...	−0.14	0.05	16.89	0.021	
	100	<0.05	...	−0.01	0.05	9.55	0.025	
	170	<0.05	...	−0.18	0.14	5.71	0.043	
318.....	60	0.13	0.01	0.13	0.09	16.82	0.031	
	100	0.35	0.03	0.67	0.11	9.30	0.017	
	170	0.96	0.04	1.07	0.23	5.97	0.049	
459.....	60	0.13	0.02	0.51	0.06	13.24	0.023	
	100	0.38	0.03	0.79	0.18	7.50	0.037	
	170	0.50	0.03	0.45	0.11	6.59	0.042	
460.....	60	3.29	0.09	4.05	0.48	14.61	0.041	
	100	9.11	0.33	7.62	0.47	8.98	0.084	
	170	11.25	1.10	9.57	0.28	7.79	0.036	
655.....	60	0.42	0.03	0.46	0.08	12.64	0.025	
	100	1.11	0.04	1.01	0.06	7.43	0.037	
	170	5.36	0.03	5.41	0.12	5.70	0.045	
664.....	60	0.75	0.15	0.83	0.14	15.13	0.033	
	100	0.77	0.13	1.12	0.10	8.92	0.020	
	170	0.97	0.03	0.85	0.18	5.16	0.026	
666.....	60	<0.03	...	0.07	0.05	13.49	0.025	
	100	<0.03	...	0.12	0.06	7.71	0.028	
	170	<0.04	...	0.03	0.09	5.11	0.037	
692.....	60	0.54	0.04	0.56	0.09	14.89	0.035	
	100	1.43	0.21	1.37	0.09	8.65	0.031	
	170	3.91	0.09	3.12	0.28	4.45	0.033	
836.....	60	7.03	0.38	7.35	0.18	17.62	0.051	
	100	14.22	0.50	14.43	0.26	9.04	0.070	
	170	11.63	0.21	12.18	0.28	6.14	0.015	
848.....	60	<0.06	...	0.19	0.04	17.61	0.028	
	100	0.05	0.01	0.16	0.03	10.17	0.021	
	170	1.41	0.26	1.06	0.37	6.34	0.044	
857.....	60	0.65	0.05	0.79	0.13	12.71	0.022	
	100	2.83	0.17	2.72	0.12	7.19	0.037	
	170	7.76	0.18	6.76	0.21	5.24	0.037	
873.....	60	3.82	0.08	4.65	0.20	15.98	0.030	

TABLE 7—*Continued*

VCC	λ (μm)	$F_{\rm model}$[a] (Jy)	$\epsilon(F_{\rm model})$ (Jy)	$F_{\rm map}$[b] (Jy)	$\epsilon(F_{\rm map})$ (Jy)	$B_{\rm backgr}$[c] (MJy sr^{-1})	f_B[d]	Notes
	100	...	...	8.61	0.18	10.06	0.081	Poor fit
	170	17.72	0.29	17.34	0.28	6.52	0.023	
890	60	<0.04	...	−0.04	0.06	17.38	0.033	
	100	<0.03	...	0.08	0.06	9.84	0.027	
	170	0.12	0.04	0.10	0.05	5.98	0.039	
912	60	0.83	0.04	1.03	0.09	14.39	0.045	
	100	2.34	0.28	2.50	0.08	7.93	0.060	
	170	2.82	0.10	2.78	0.12	5.17	0.032	
971	60	0.29	0.02	0.17	0.12	16.75	0.023	
	100	0.83	0.04	0.97	0.10	9.57	0.033	
	170	1.38	0.09	1.31	0.19	6.07	0.040	
984	60	<0.04	...	−0.16	0.13	15.04	0.027	
	100	<0.04	...	0.09	0.10	8.93	0.025	
	170	<0.17	...	−0.07	0.09	5.06	0.020	
1001	60	...	...	...	...	...	...	Not observed
	100	<0.02	...	−0.03	0.03	8.28	0.066	
	170	0.23	0.03	0.25	0.05	4.99	0.027	
1002	60	0.94	0.05	0.88	0.10	17.34	0.021	
	100	3.36	0.20	3.37	0.09	8.53	0.050	
	170	5.30	0.11	5.35	0.16	6.53	0.050	
1003	60	0.87	0.04	0.75	0.30	17.59	0.033	
	100	3.94	0.32	3.16	0.23	11.22	0.040	
	170	3.12	0.06	2.50	0.12	4.88	0.013	
1043	60	2.36	0.07	2.61	0.64	16.75	0.015	
	100	7.67	0.35	7.08	0.52	10.77	0.046	
	170	16.72	0.59	13.04	0.78	5.53	0.027	
1047	60	<0.04	...	−0.15	0.12	13.85	0.050	
	100	<0.04	...	−0.20	0.11	8.41	0.032	
	170	<0.21	...	−0.11	0.12	4.12	0.063	
1110	60	1.79	0.24	1.43	0.18	13.89	0.029	
	100	4.08	0.27	4.23	0.32	9.29	0.028	
	170	10.01	0.17	9.41	0.23	6.86	0.038	
1121	60	...	...	...	...	...	...	Not observed
	100	<0.02	...	0.04	0.04	9.42	0.035	
	170	...	...	−0.12	0.07	4.90	0.012	Confusion limited
1158	60	<0.04	...	0.59	0.21	12.13	0.025	
	100	<0.05	...	0.09	0.20	7.32	0.048	
	170	<0.14	...	−0.11	0.11	4.86	0.009	
1189	60	0.18	0.02	0.31	0.07	16.86	0.023	
	100	0.49	0.02	0.43	0.07	9.29	0.022	
	170	1.16	0.03	1.15	0.27	5.60	0.033	
1196	60	<0.04	...	−0.14	0.11	12.10	0.043	
	100	<0.04	...	0.07	0.10	8.30	0.049	
	170	...	...	1.24	0.32	6.92	0.025	Poor fit
1217	60	<0.04	...	−0.20	0.11	14.62	0.019	
	100	<0.03	...	0.10	0.10	9.14	0.033	
	170	<0.07	...	0.08	0.09	5.35	0.021	
1253	60	0.14	0.04	0.16	0.14	12.30	0.043	
	100	0.81	0.09	0.80	0.15	7.16	0.060	
	170	1.13	0.09	1.01	0.11	5.14	0.068	
1326	60	2.36	0.19	2.52	0.06	14.33	0.051	
	100	2.89	0.14	2.48	0.09	9.22	0.065	
	170	2.98	0.31	1.93	0.21	8.60	0.030	
1368	60	<0.15	...	0.02	0.07	16.07	0.034	
	100	<0.03	...	0.03	0.07	10.07	0.040	
	170	0.20	0.05	0.29	0.25	8.47	0.060	
1379	60	1.14	0.06	1.16	0.11	12.12	0.049	
	100	3.27	0.19	3.32	0.11	6.33	0.067	
	170	4.98	0.15	4.65	0.21	6.66	0.023	
1410	60	0.22	0.02	0.39	0.10	13.31	0.040	
	100	0.36	0.03	0.44	0.09	7.50	0.028	
	170	0.69	0.04	0.67	0.12	6.42	0.032	
1412	60	<0.06	...	0.03	0.26	15.98	0.032	
	100	<0.07	...	0.08	0.19	10.36	0.023	
	170	0.71	0.08	0.63	0.32	9.66	0.038	Off-center emission

TABLE 7—*Continued*

VCC	λ (μm)	$F_{\rm model}$[a] (Jy)	$\epsilon(F_{\rm model})$ (Jy)	$F_{\rm map}$[b] (Jy)	$\epsilon(F_{\rm map})$ (Jy)	$B_{\rm backgr}$[c] (MJy sr^{-1})	f_B[d]	Notes
1419	60	0.06	0.02	0.04	0.15	11.60	0.031	
	100	0.28	0.04	0.18	0.07	7.23	0.044	
	170	0.44	0.07	0.17	0.19	5.51	0.046	
1450	60	0.74	0.05	0.75	0.08	10.05	0.048	
	100	2.99	0.23	2.93	0.13	6.59	0.060	
	170	3.96	0.13	3.95	0.18	7.18	0.057	
1552	60	0.29	0.08	0.38	0.14	11.53	0.027	
	100	1.08	0.06	1.19	0.13	7.23	0.054	
	170	1.94	0.13	1.67	0.23	6.33	0.035	
1554	60	5.56	0.25	5.11	0.26	17.06	0.068	
	100	9.07	0.36	8.20	0.22	10.71	0.092	
	170	10.65	0.19	10.21	0.46	7.14	0.013	
1569	60	$<$0.05	...	0.28	0.11	10.94	0.032	
	100	$<$0.05	...	0.19	0.11	7.81	0.032	
	170	$<$0.06	...	0.05	0.05	5.40	0.023	
1575	60	1.11	0.05	1.36	0.07	15.50	0.040	
	100	2.08	0.27	2.05	0.12	8.16	0.074	
	170	2.74	0.14	2.52	0.19	6.35	0.027	
1581	60	$<$0.03	...	$-$0.04	0.05	16.94	0.028	
	100	$<$0.03	...	0.01	0.04	9.68	0.064	
	170	0.33	0.06	0.31	0.11	6.44	0.038	
1673/1676 ..	60	...	...	11.32	0.19	17.99	0.030	Interacting
	100	...	...	29.34	0.46	12.82	0.095	System
	170	96.85	1.56	85.21	0.78	8.21	0.075	
1675	60	0.05	0.01	0.09	0.06	15.84	0.019	
	100	$<$0.03	...	0.03	0.07	9.15	0.028	
	170	0.16	0.04	0.30	0.07	6.39	0.054	
1678	60	0.08	0.01	0.73	0.16	16.67	0.039	
	100	0.43	0.05	0.48	0.15	9.20	0.052	
	170	0.68	0.12	0.66	0.12	7.10	0.048	
1686	60	0.45	0.08	0.32	0.17	12.28	0.025	
	100	1.13	0.06	1.50	0.15	7.90	0.032	
	170	1.49	0.10	1.47	0.23	7.29	0.052	
1690	60	6.20	0.41	7.12	0.46	14.16	0.063	
	100	16.00	0.67	20.05	0.73	8.90	0.032	
	170	29.16	0.32	28.62	0.53	8.35	0.072	
1699	60	0.27	0.04	0.77	0.13	16.61	0.045	
	100	0.39	0.02	0.98	0.12	9.30	0.058	
	170	0.49	0.03	0.49	0.28	7.12	0.035	
1725	60	0.05	0.01	$-$0.05	0.06	16.03	0.023	
	100	0.30	0.05	0.45	0.08	8.80	0.032	
	170	0.48	0.03	0.45	0.19	6.08	0.092	
1726	60	$<$0.05	...	0.33	0.07	16.47	0.035	
	100	$<$0.05	...	0.14	0.08	9.76	0.068	
	170	0.24	0.03	0.49	0.27	6.62	0.041	
1727	60	4.16	0.22	3.91	0.33	16.90	0.026	
	100	12.34	0.41	10.90	0.36	11.87	0.069	
	170	29.19	1.20	22.91	0.35	9.38	0.055	
1730	60	1.52	0.22	2.22	0.15	15.20	0.042	
	100	3.64	0.26	4.41	0.12	6.86	0.078	
	170	5.46	0.55	5.32	0.12	7.84	0.049	
1750	60	$<$0.03	...	0.22	0.05	15.45	0.044	
	100	0.04	0.01	0.28	0.05	8.90	0.070	
	170	0.08	0.02	0.11	0.04	6.02	0.043	
1757	60	0.10	0.01	$-$0.42	0.09	14.04	0.023	
	100	0.50	0.02	1.02	0.10	8.32	0.042	
	170	0.79	0.03	0.79	0.12	6.47	0.064	

NOTE.—Table 7 is also available in machine-readable form in the electronic edition of the *Astrophysical Journal Supplement*.

[a] The flux $F_{\rm model}$ derived from integrating the model fit to infinity. The upper limits are indicated with a "$<$" sign in front.

[b] The flux $F_{\rm map}$ derived from integrating the raw maps.

[c] The average background brightness $B_{\rm backgr}$.

[d] The 1 σ fractional uncertainty f_B in the background brightness, determined from the spread in the response of individual detector pixels to the background at the ends of the scans.

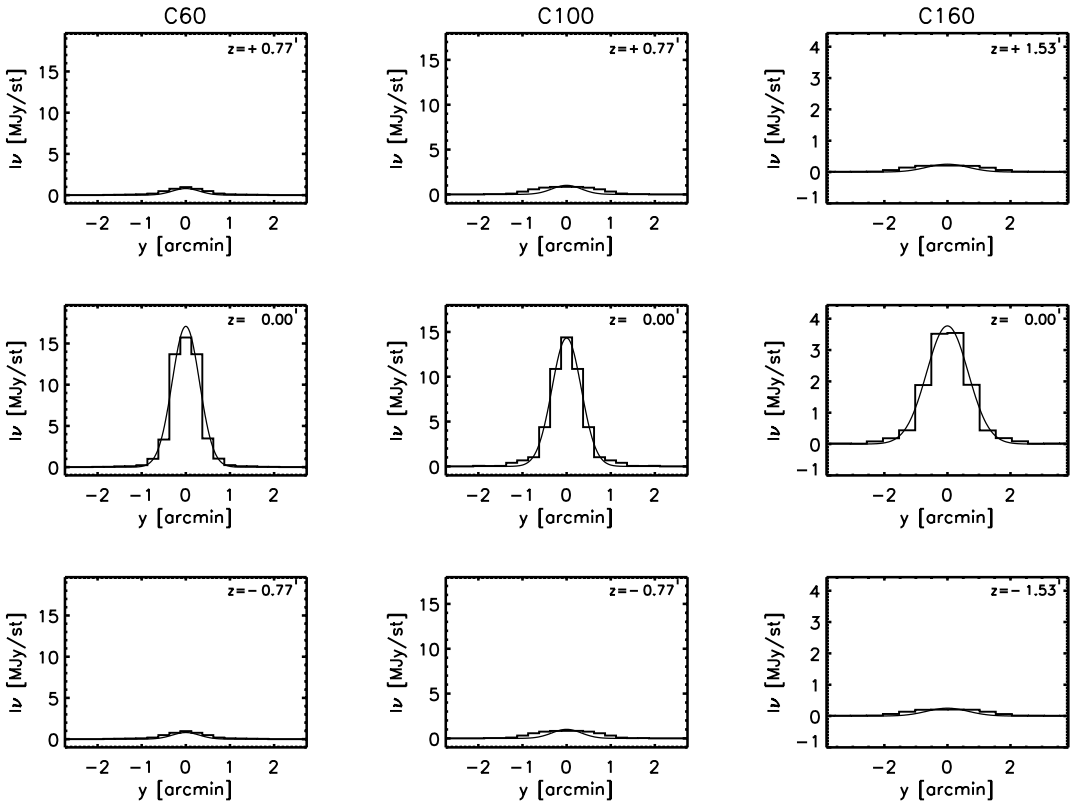

FIG. 8.—Example of a beam fit on simulated noiseless maps of 1 Jy point sources, sampled in exactly the same way as the *ISO* Virgo maps. The simulated beams are plotted as histograms, while the model fits are plotted as solid lines. The left, middle, and right panels give the fits to the 60, 100, and 170 μm maps, respectively. The middle panels give the fits to the central map row (the profile along the scan direction), while the upper and the lower panels give the fits to the neighboring map rows. The shift in cross-scan direction z between the central and the neighboring rows is indicated in each panel.

wavelengths, namely, at 60 and 100 μm, and five (7.9%) galaxies were not detected at one wavelength. The nine galaxies not detected at any wavelength are mainly early-type spirals, of SB0 (VCC 984), SBa (VCC 1047), or Sa (VCC 1158) Hubble type, and Im irregulars (VCC 17, VCC 169, VCC 666, VCC 1121). There is also one SBm (VCC 1217) and one Scd: (VCC 1569) which escaped detection. The nondetected early-type spirals are bright objects ($12.1 < B_T < 12.8$) in the cluster core, while three of the nondetected Im are faint galaxies ($15.2 < B_T < 16.8$) in the cluster periphery. The statistics of the detections at each wavelength are given in Table 8.

The faintest B-band galaxy from our sample which was detected at least at one FIR wavelength was VCC 1001. This is an Im galaxy in the cluster core with $B_T = 16.6$ and was detected only at 170 μm. (The galaxy was not observed at 60 μm and was not detected at 100 μm.) The derived flux at 170 μm is 0.23 ± 0.03 Jy. The galaxy has an extremely cold dust emission, and we will discuss its properties in a subsequent paper. The faintest B-band galaxies from our sample which were detected at least at two FIR wavelengths were VCC 130 and VCC 1750, two BCDs in the cluster periphery with $B_T = 16.5$. Both galaxies were detected only at 100 and 170 μm. VCC 1750 reached 0.04 ± 0.01 and 0.08 ± 0.02 Jy at 100 and 170 μm, respectively.

The faintest detected emission at 60 μm is 0.05 ± 0.01 Jy (detected in VCC 1675, a peculiar galaxy in the cluster periphery, and in VCC 1725, an Sm/BCD galaxy also in the

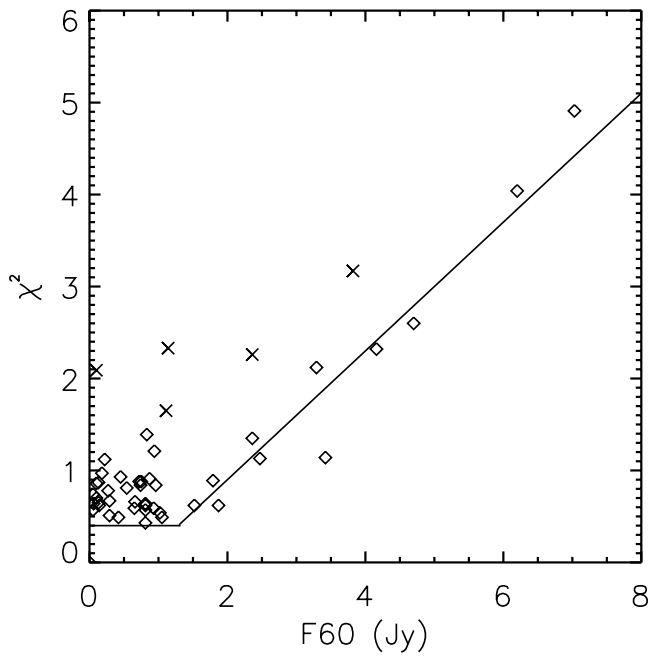

FIG. 9.—Model fits to the observed brightness profiles of all the Virgo galaxies from our sample (except for the interacting system VCC 1673/VCC 1676; see § 6.2.4). Statistical uncertainties for selected map pixels near the extremities and center of the scans are indicated by the 3 σ error bars. The legend is as in Fig. 8.

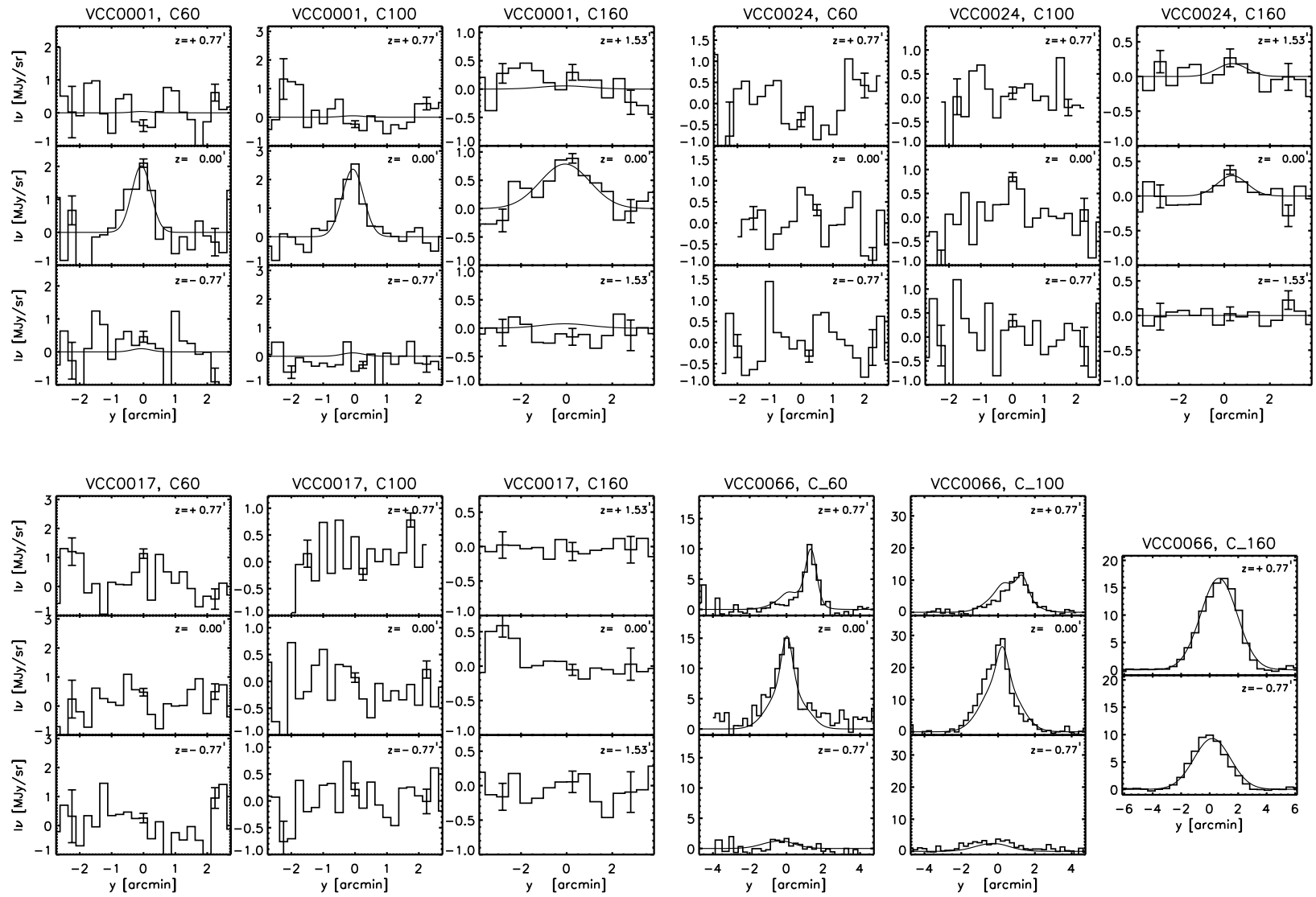

FIG. 10.—Uncorrected χ^2 values derived from fitting the Gaussian models to the maps vs. the corresponding flux densities at 60 μm obtained from integrating the model fit to infinity. The data were plotted as diamonds, except for those galaxies for which the model was an imperfect fit to the data, which were plotted as crosses. The solid line rising for $F_{60} > 1.5$ Jy represents the linear correlations between flux and χ^2, as a result of systematic errors due to the oversampling in cross-scan direction. For faint flux densities χ^2 is dominated by systematic errors, producing a clumpy distribution at the left-hand side of the plot, with a lower envelope, which we traced by a solid line to guide the eyes.

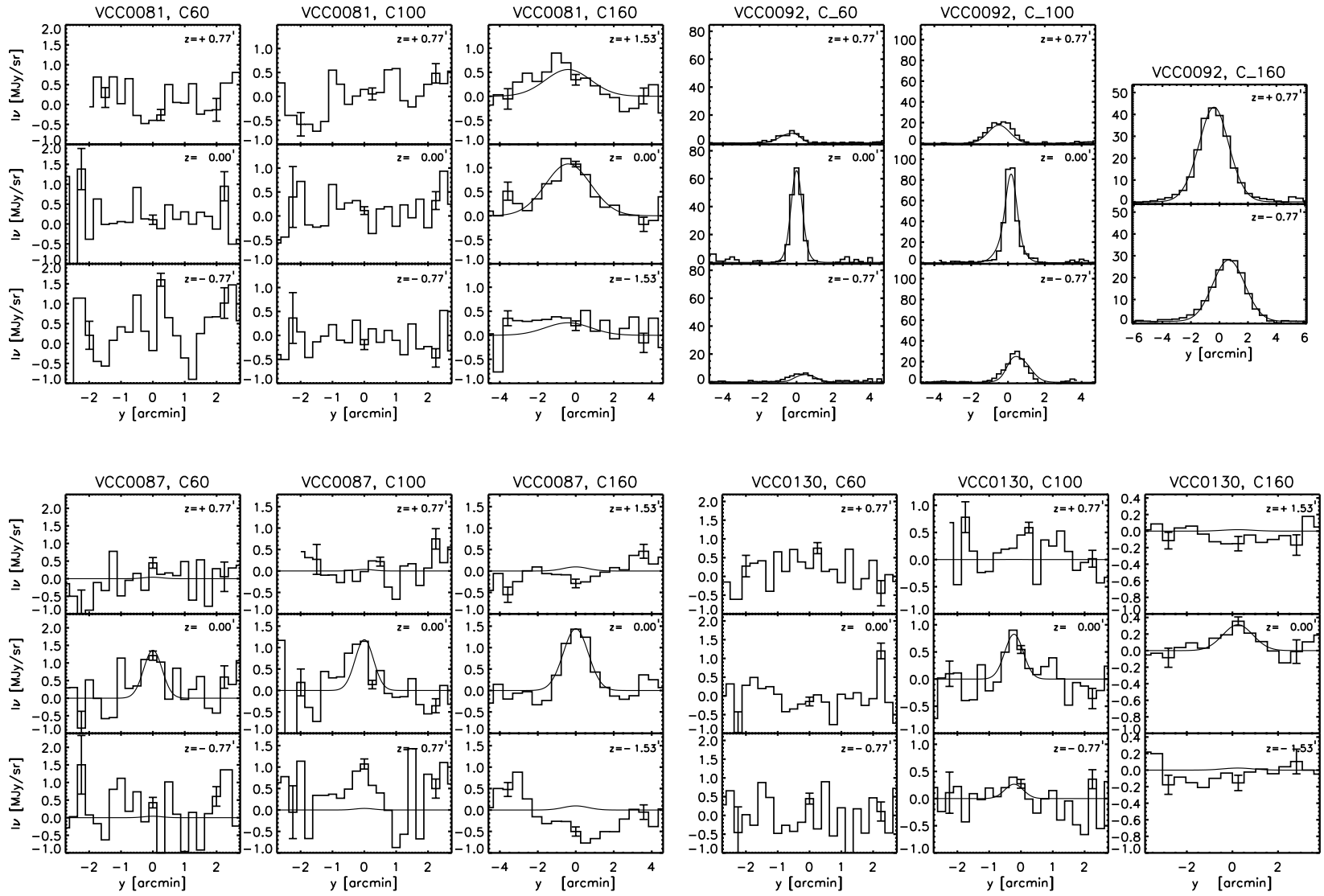

FIG. 10.—*Continued*

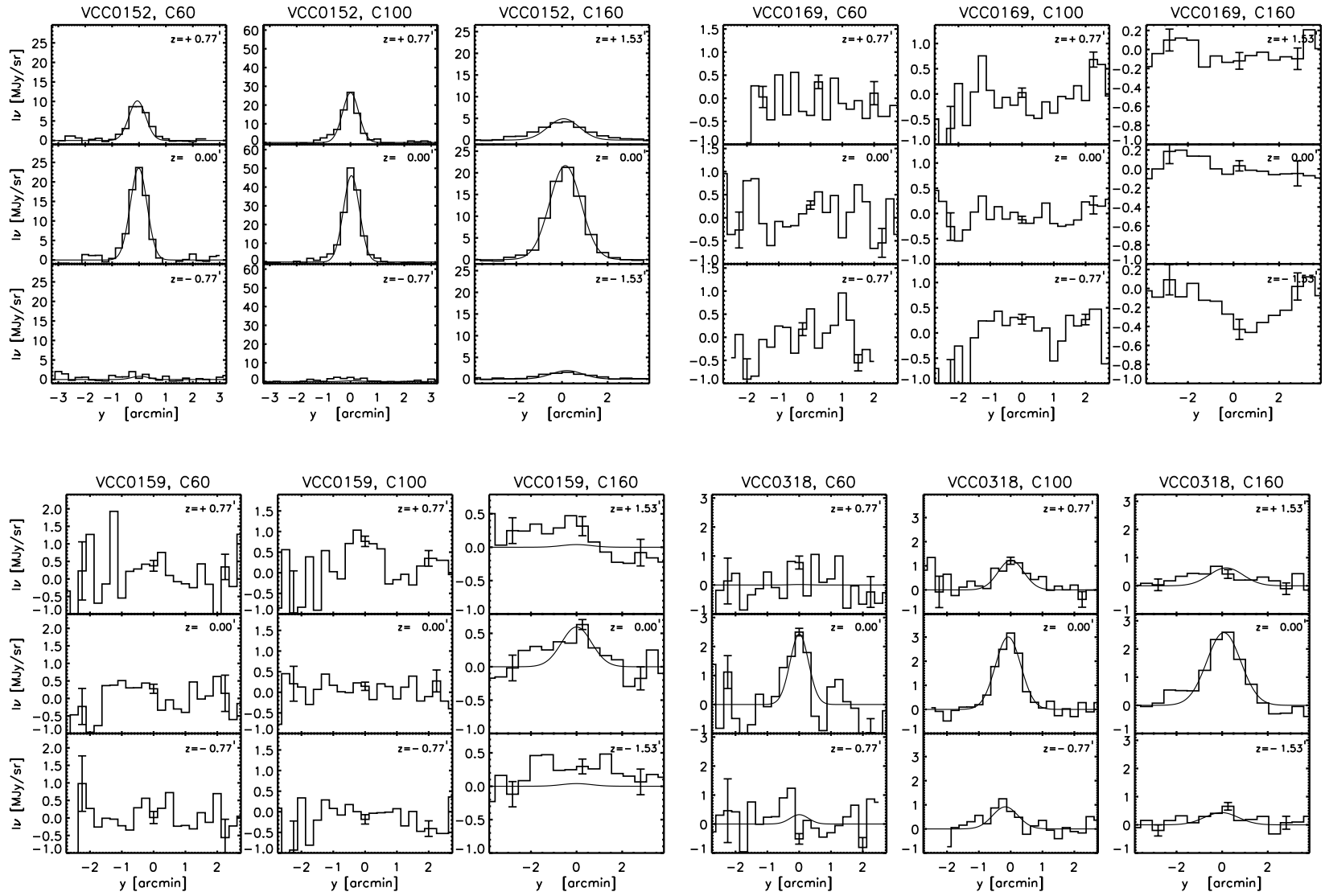

FIG. 10.—*Continued*

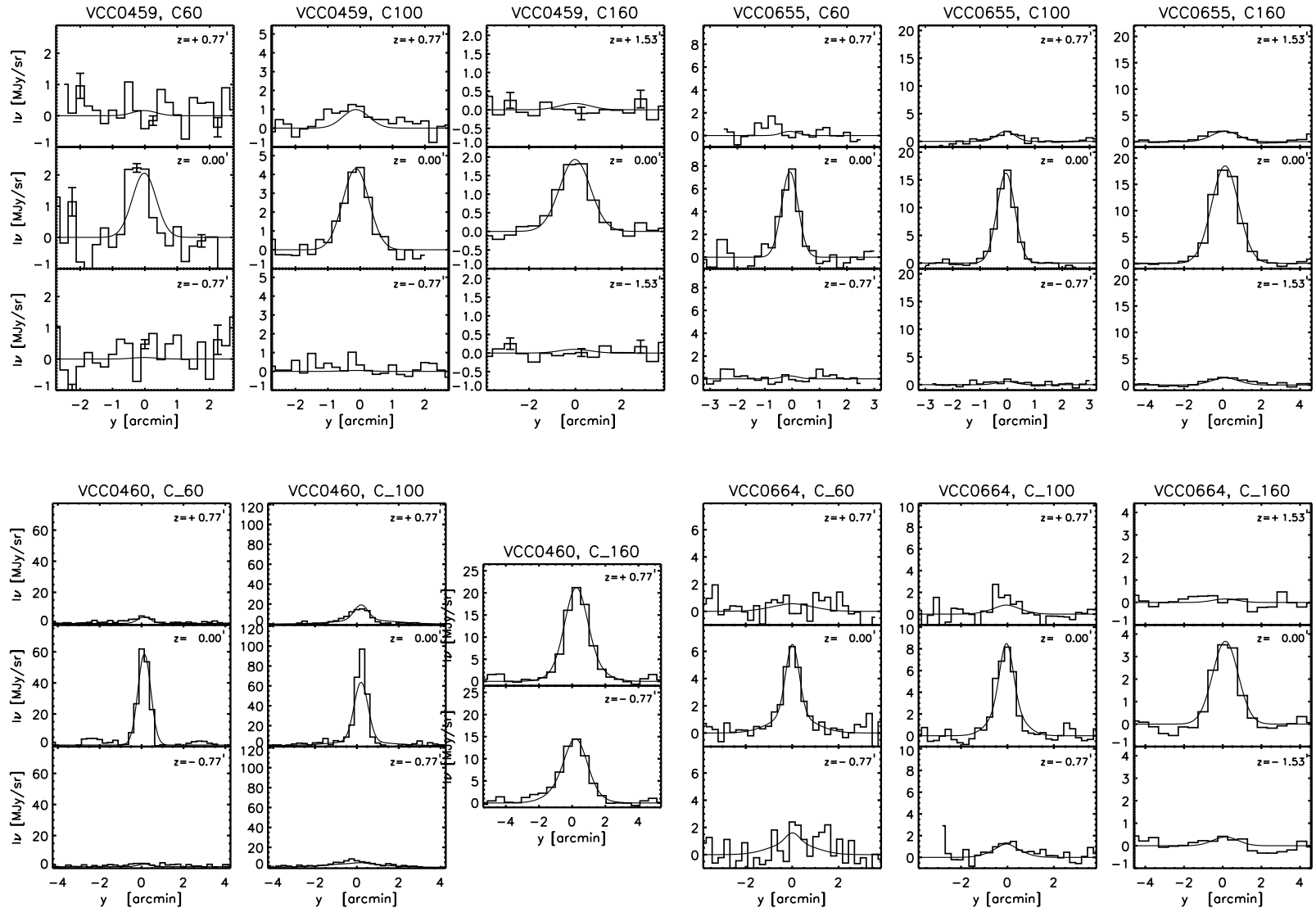

FIG. 10.—*Continued*

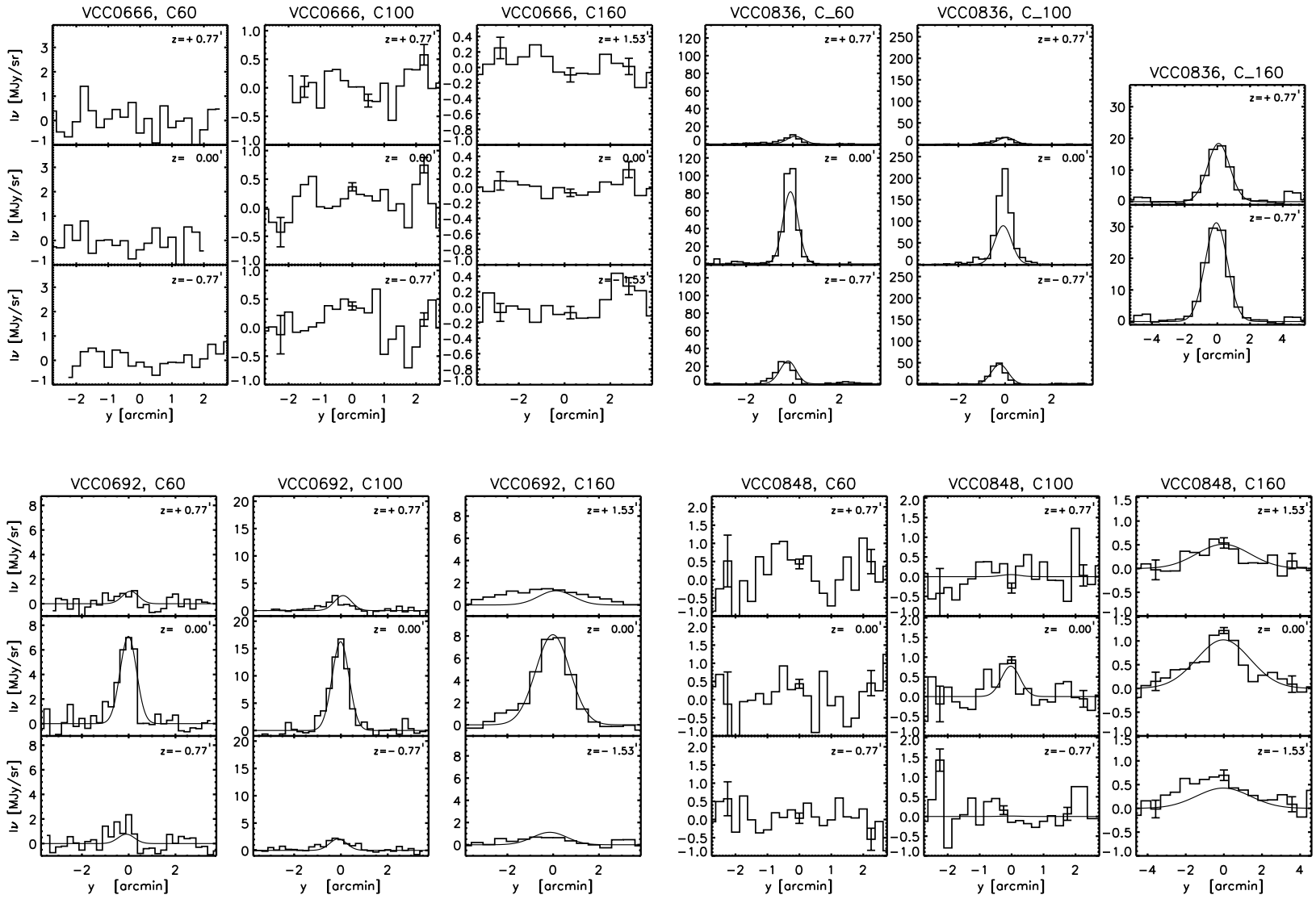

FIG. 10.—*Continued*

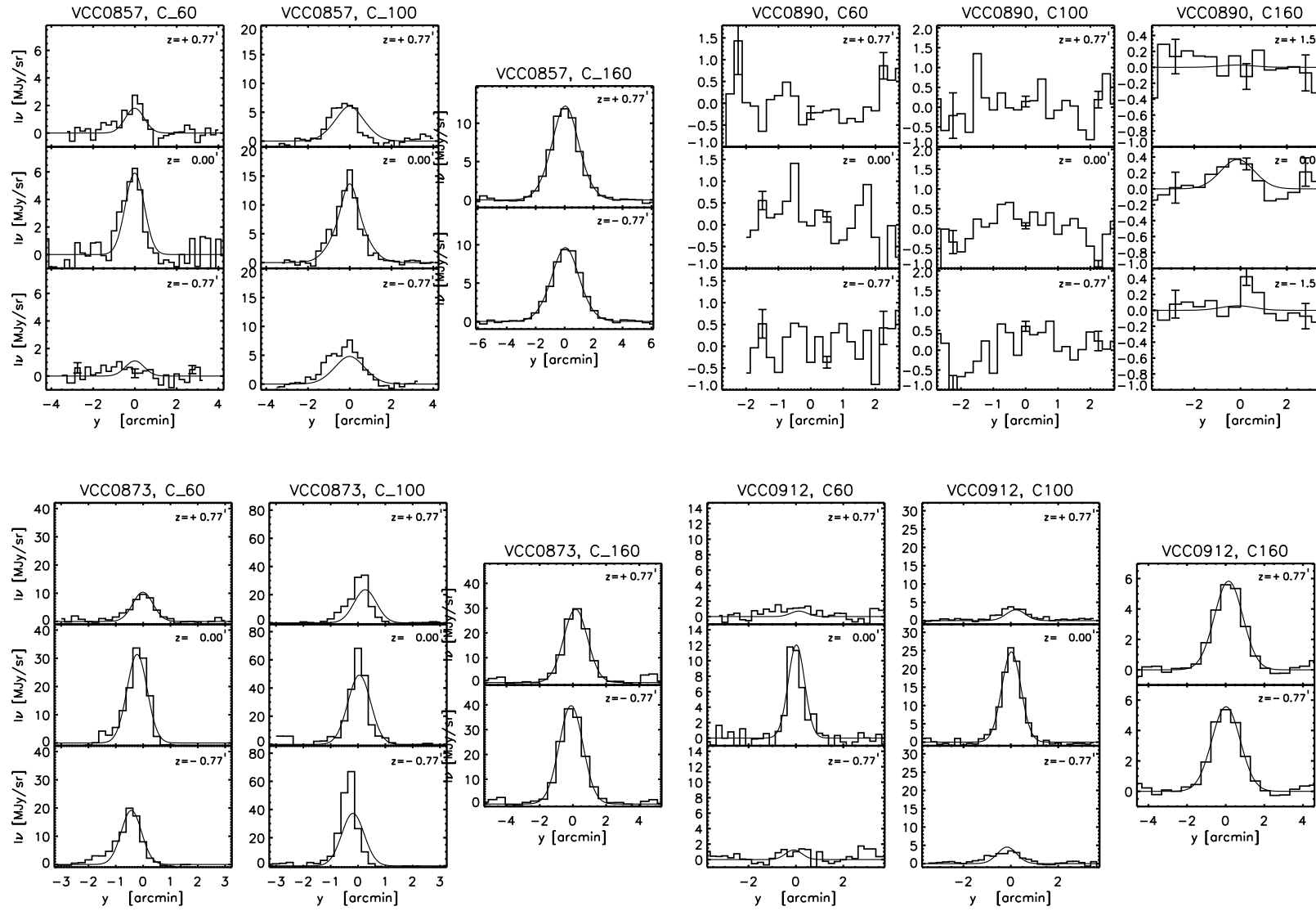

FIG. 10.—*Continued*

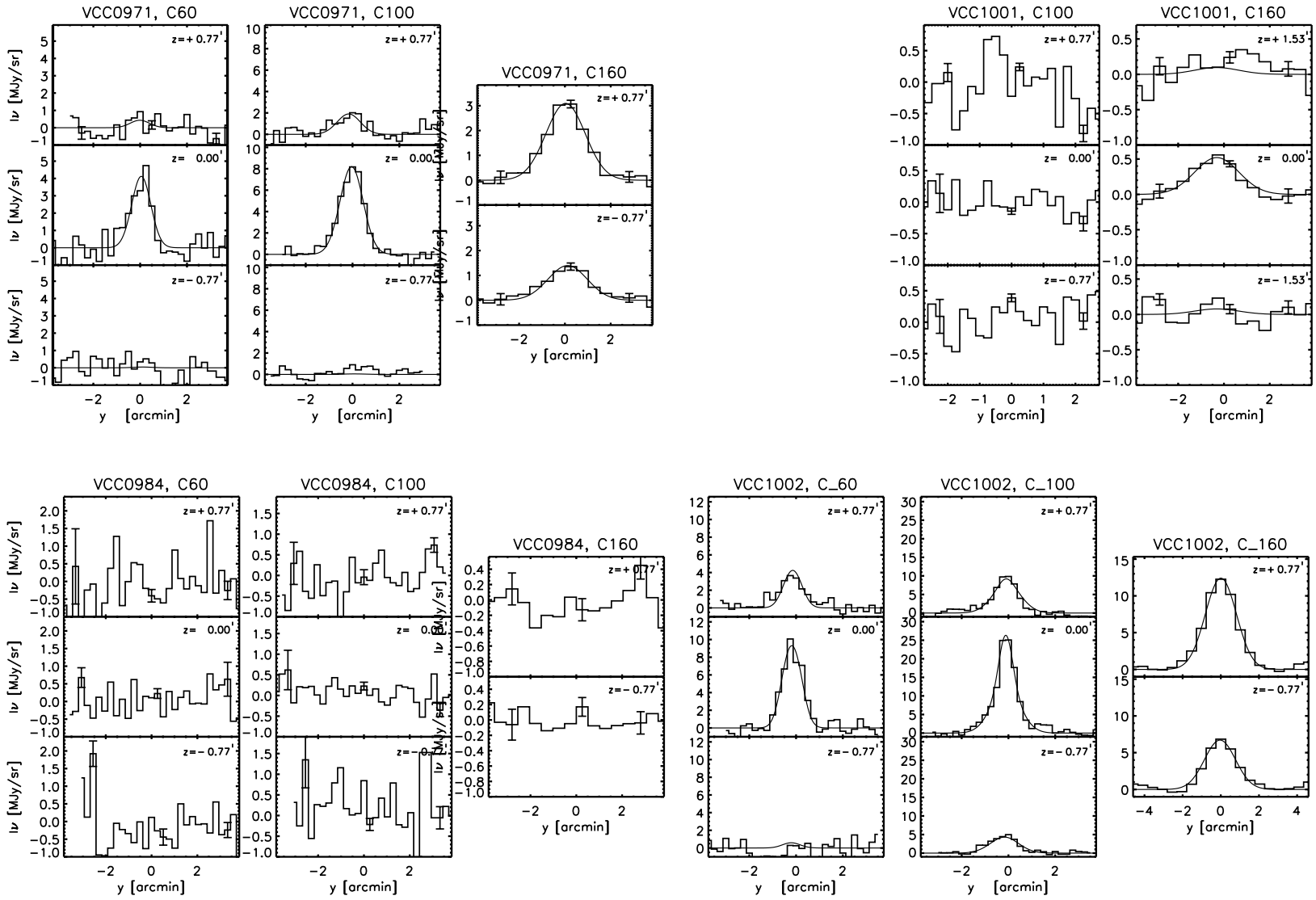

FIG. 10.—*Continued*

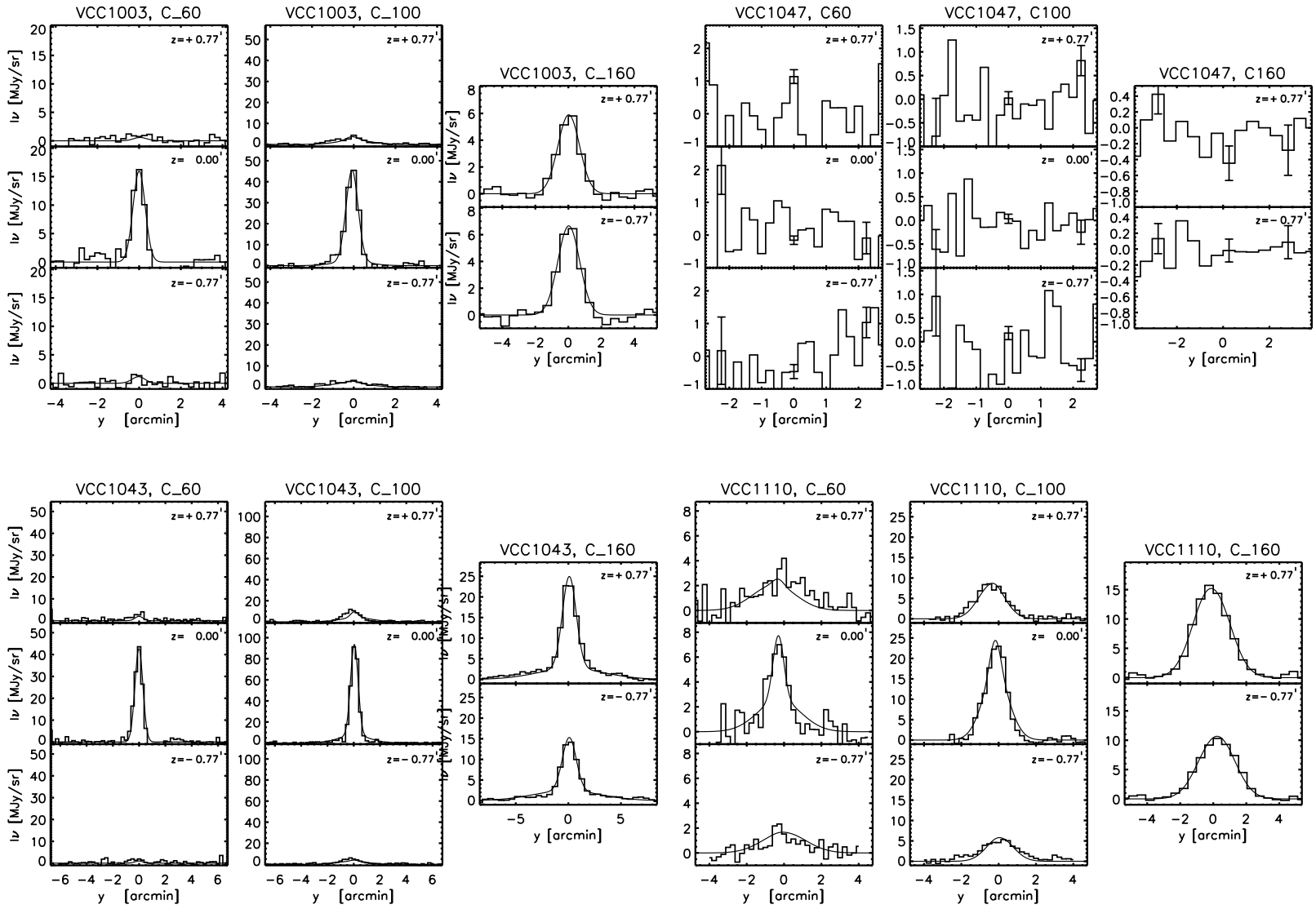

FIG. 10.—*Continued*

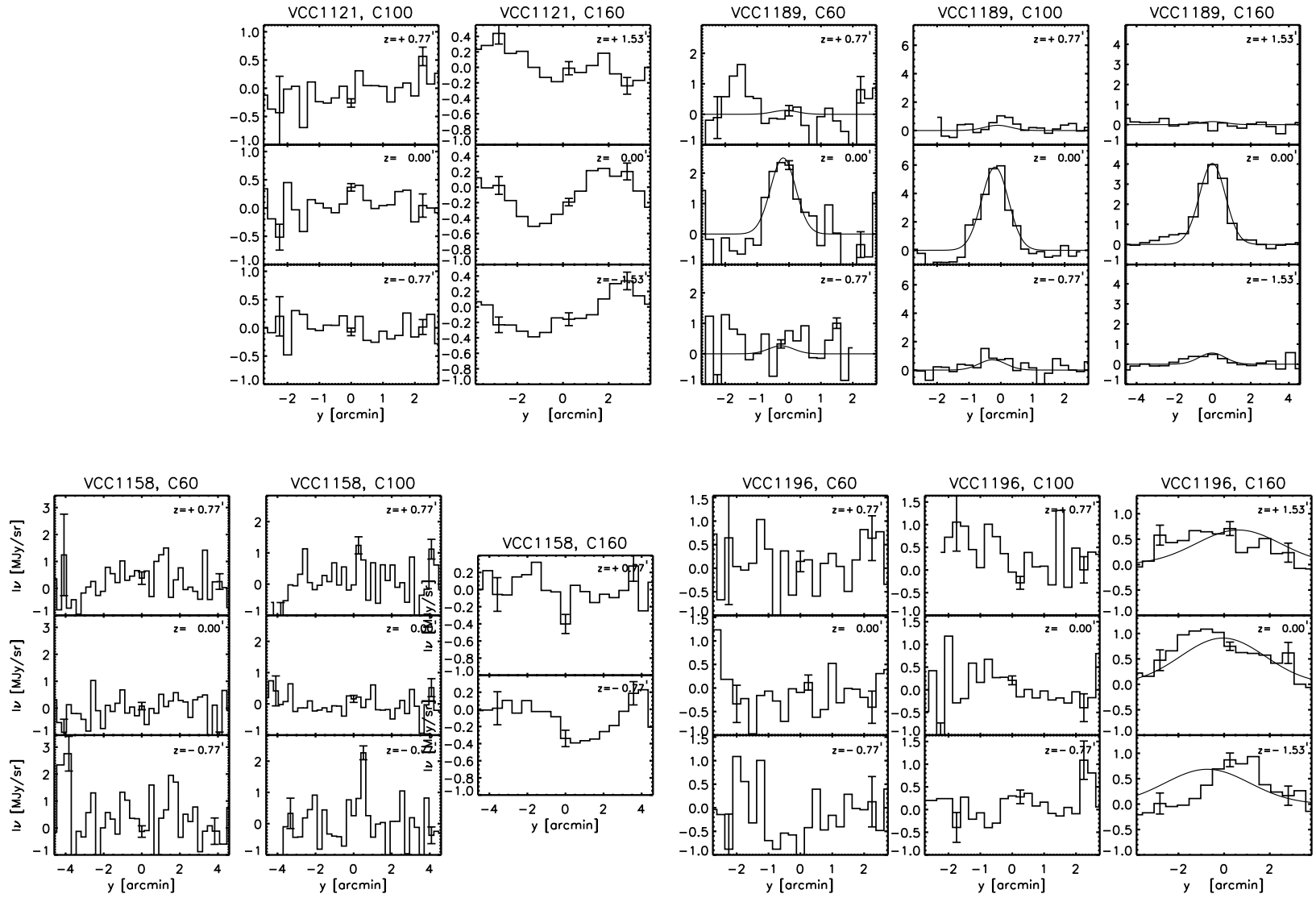

FIG. 10.—*Continued*

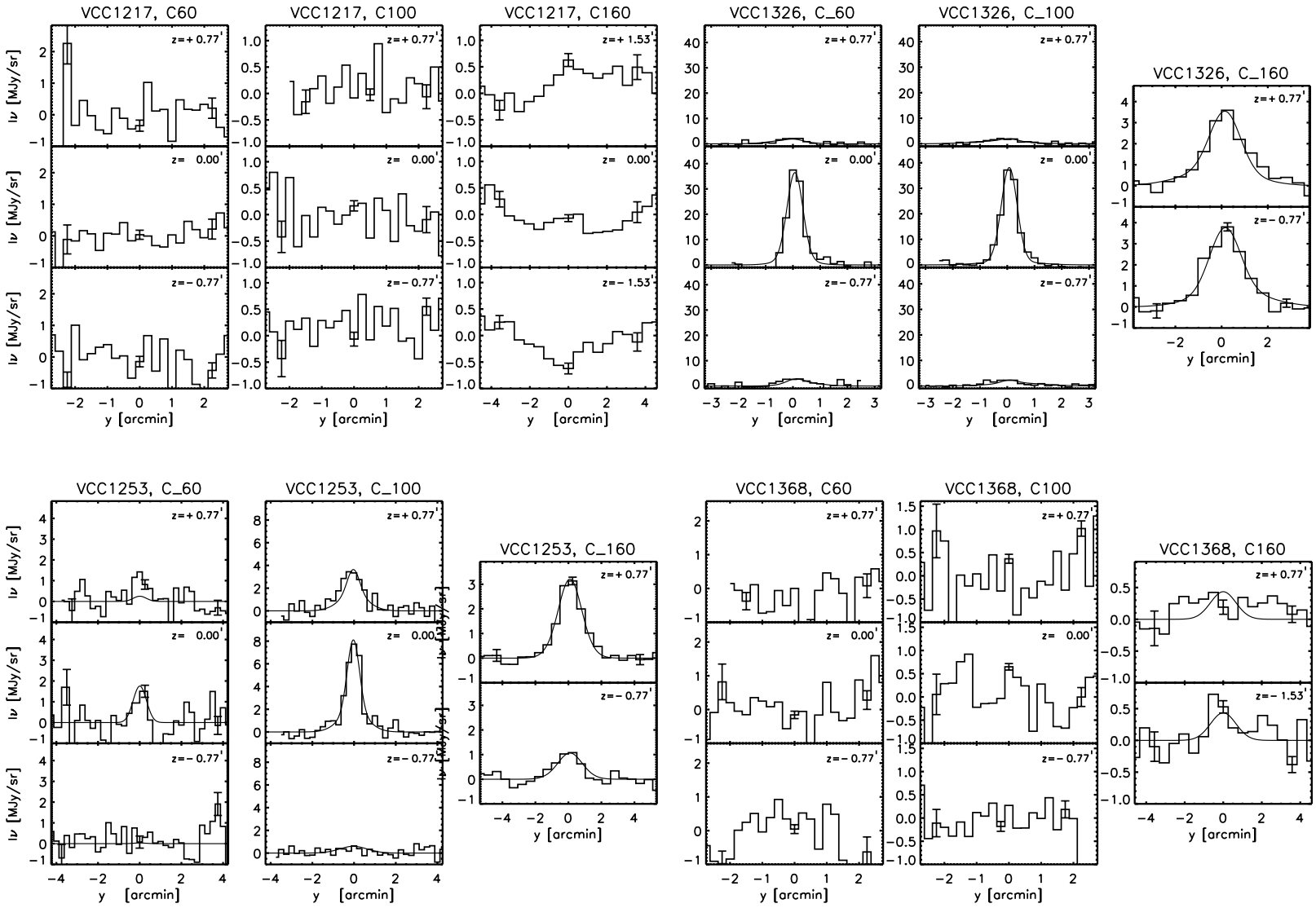

FIG. 10.—*Continued*

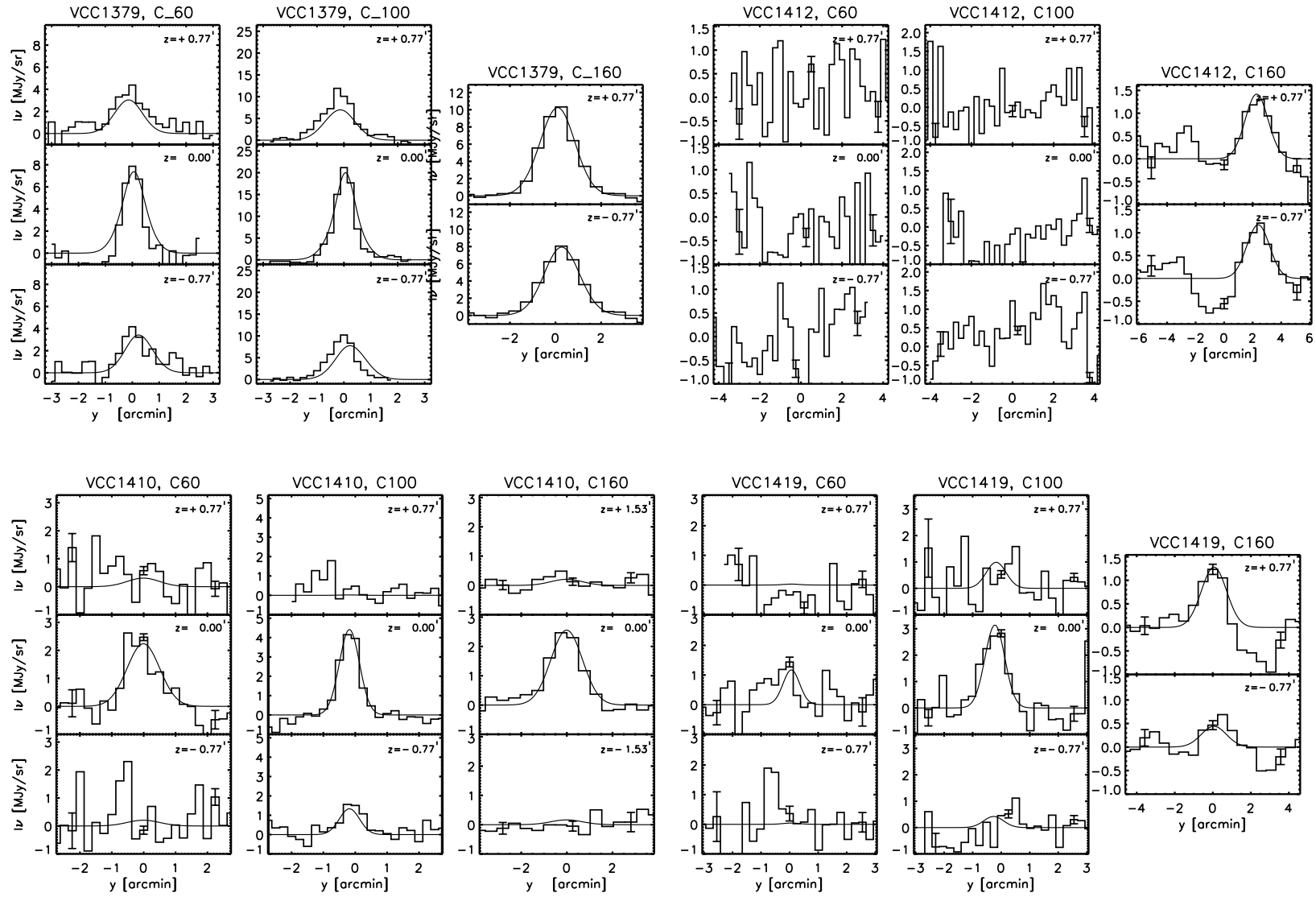

FIG. 10.—*Continued*

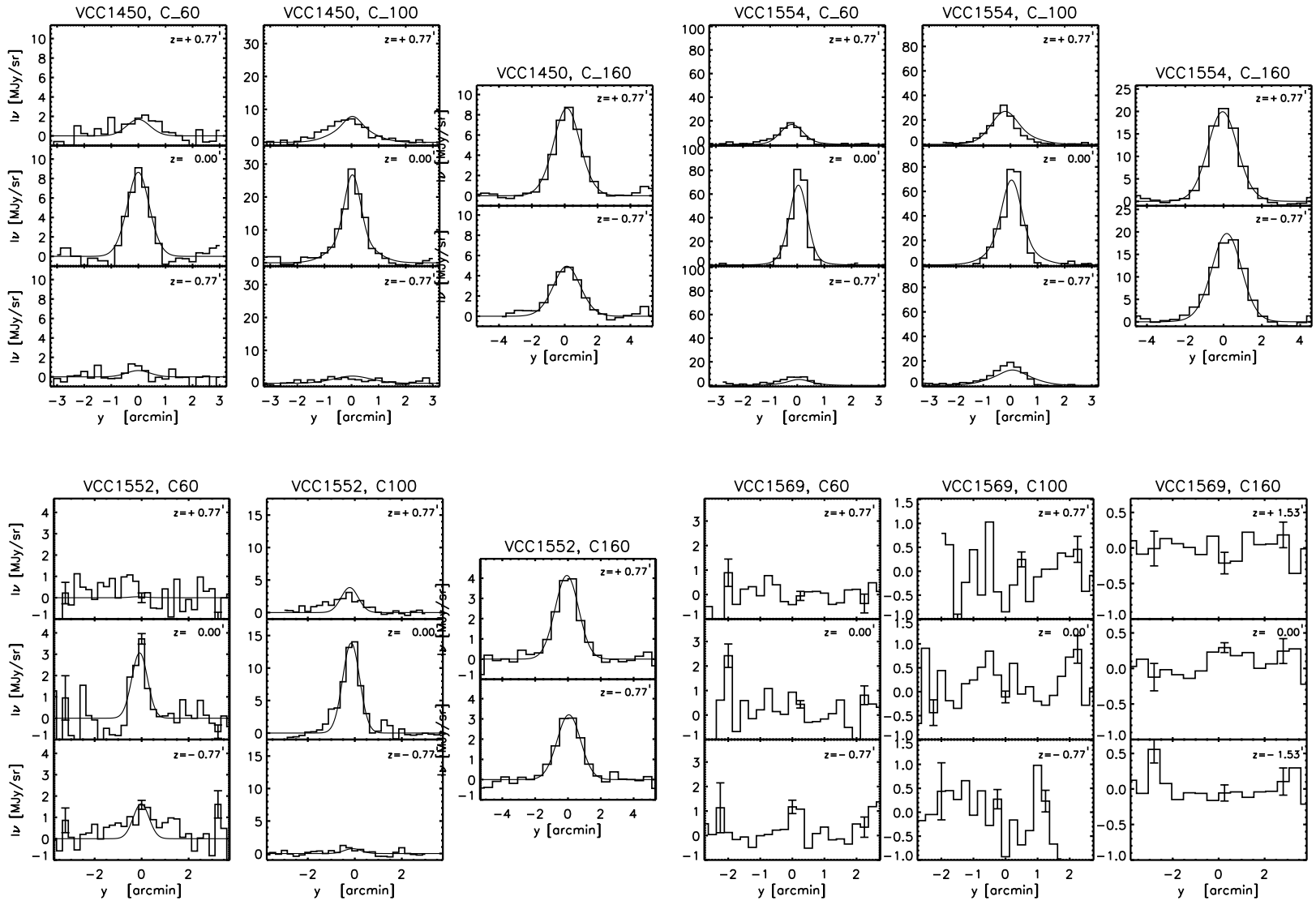

FIG. 10.—*Continued*

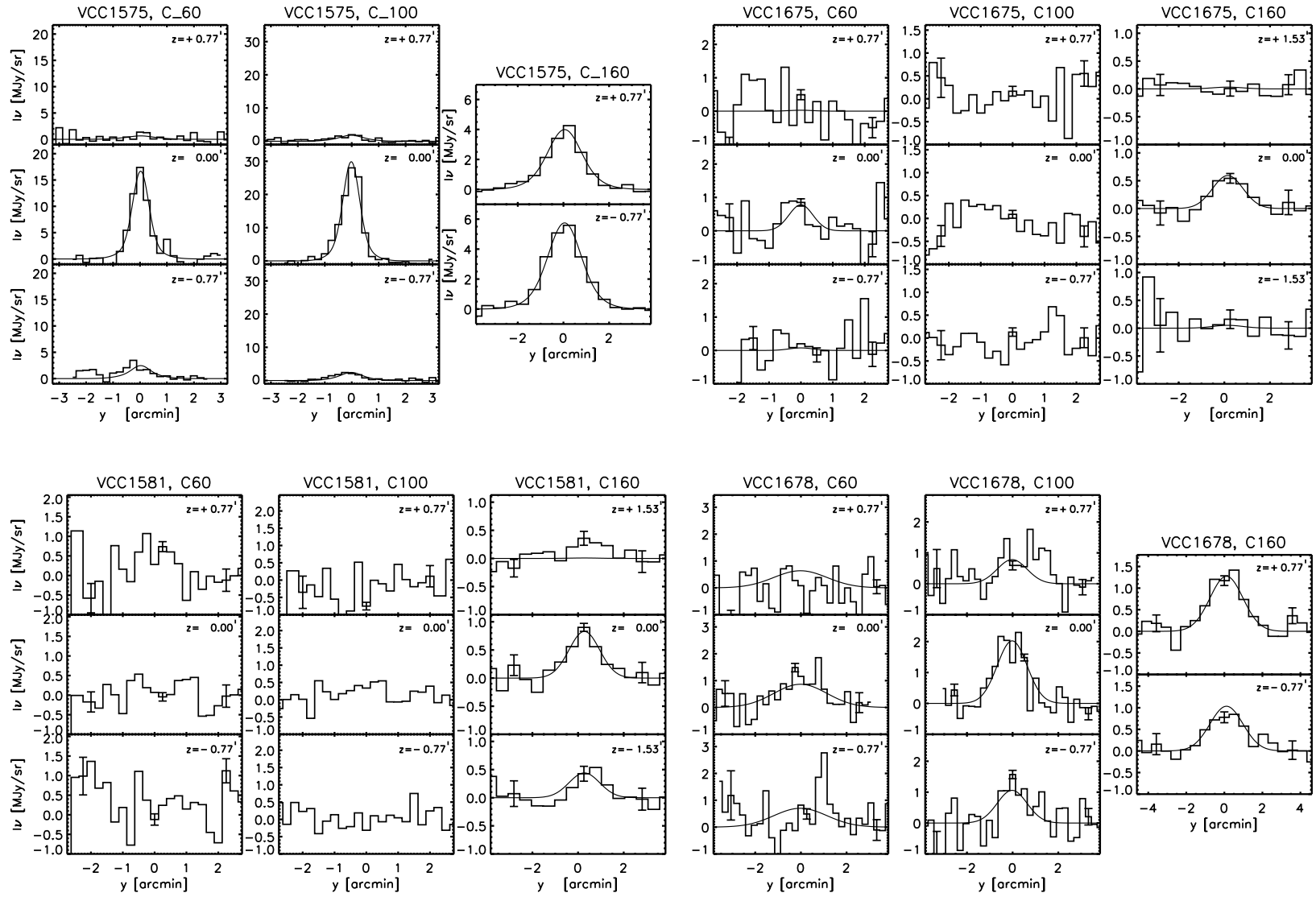

FIG. 10.—*Continued*

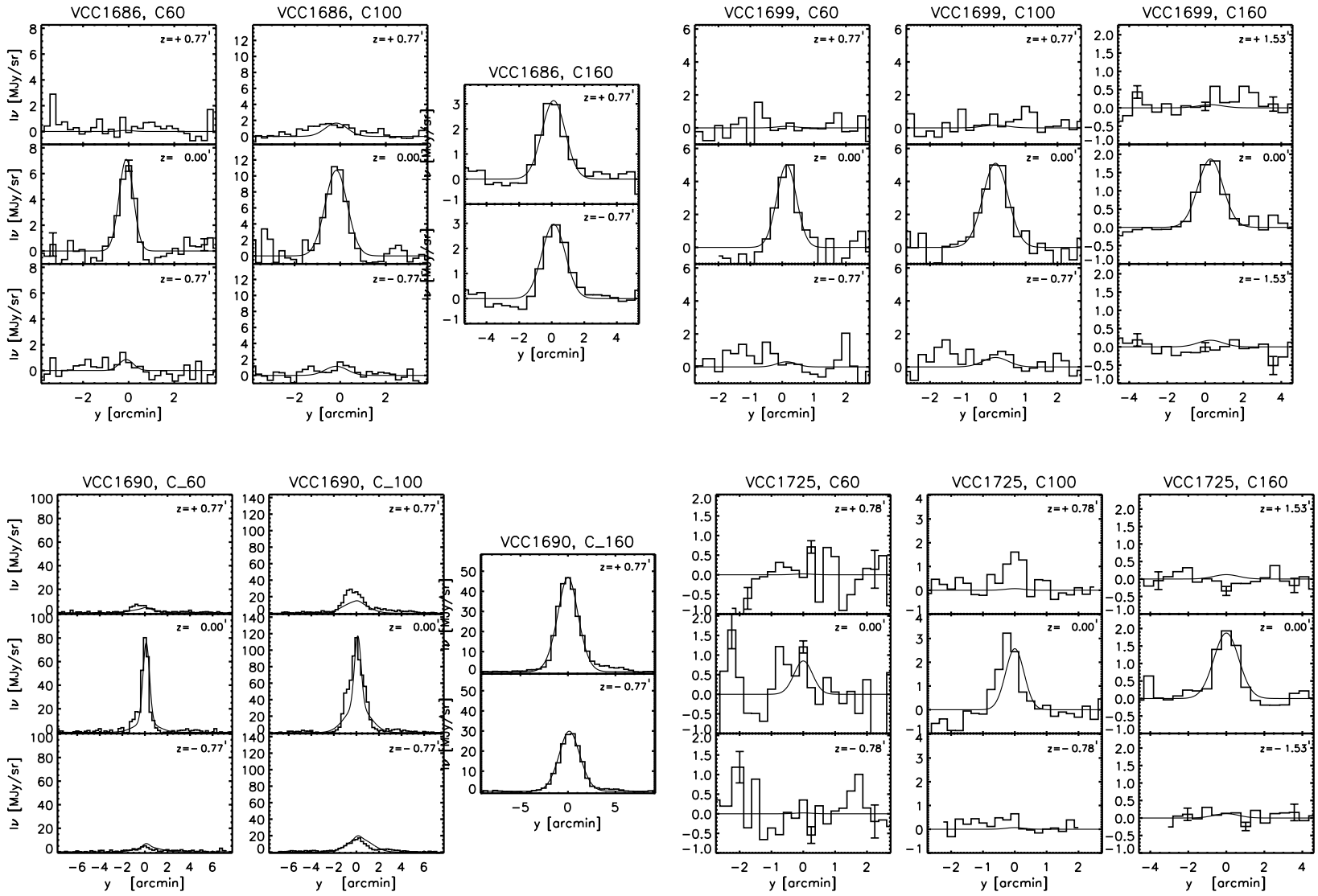

FIG. 10.—*Continued*

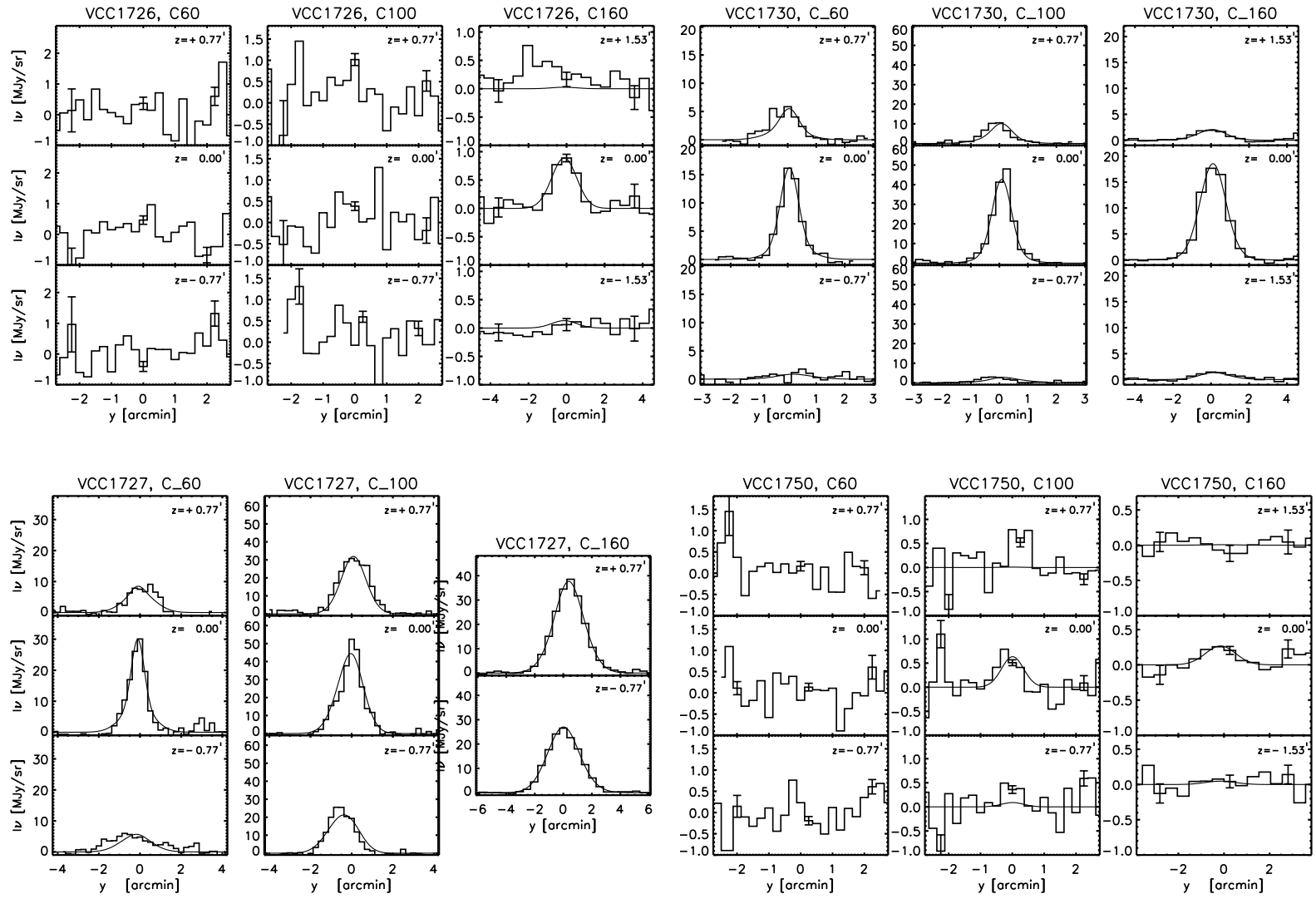

FIG. 10.—*Continued*

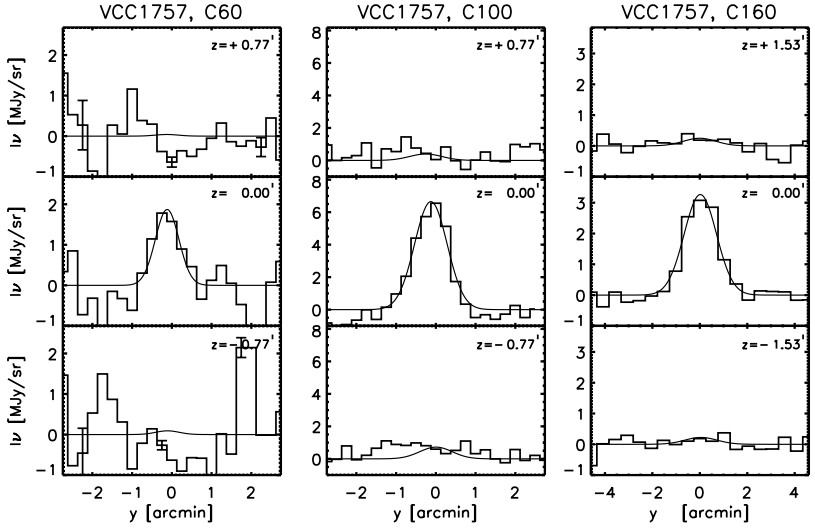

FIG. 10.—*Continued*

cluster periphery). The faintest detected emission at 100 μm is 0.04 ± 0.01 Jy (detected in VCC 1750, one of the two galaxies which were also assigned as being the faintest *B*-band galaxies detected at least at two FIR wavelengths). Finally, the faintest detected emission at 170 μm is 0.08 ± 0.02 Jy (detected in VCC 130 and VCC 1750, which were also the faintest *B*-band galaxies detected at least at two FIR wavelengths). For comparison the faintest detected *IRAS* emission on the galaxies from our sample is 0.2 Jy (VCC 459, VCC 1410, VCC 1757) at 60 μm and 0.4 Jy (VCC 1757) at 100 μm. Thus, our survey can go 10–20 times deeper (at 100 μm) than the *IRAS* survey.

The faintest upper limits (defined as 3 σ errors) assigned to the galaxies in our sample are 0.03 Jy at 60 μm (VCC 169, VCC 666, VCC 1581, VCC 1750), 0.02 Jy at 100 μm (VCC 1001, VCC 1121), and 0.04 Jy at 170 μm (VCC 666). For comparison the faintest upper limits assigned by *IRAS* to the galaxies from our sample are 0.2 and 0.5 Jy at 60 and 100 μm, respectively. Thus, our survey assigns upper limits which are again $\sim$20 times fainter (at 100 μm) than those assigned by the *IRAS* survey. The averaged 3 σ upper limits of the galaxies (point sources) from our sample were 43, 33, and 58 mJy at 60, 100, and 170 μm, respectively.

Interestingly, the highest detection rates were for the C160 band, even for dwarfs, despite the detection limit in terms of Jy being about twice as bright as the C100 and C60 detection limits. Particularly for BCDs it was not obvious that this was to be expected. The galaxies with the brightest FIR fluxes are VCC 1673/VCC 1676, which form an interacting system with total integrated flux densities of 11.32 ± 0.19, 29.34 ± 0.46, and 96.85 ± 1.56 Jy at 60, 100, and 170 μm, respectively. From the observed 63 galaxies, 21 (33.3%) galaxies present evidence for a nuclear and a disk component at least at one wavelength and four (6.3%) galaxies present evidence for a multicomponent morphology at least at one wavelength.

TABLE 8

STATISTICS OF THE DETECTIONS AT INDIVIDUAL WAVELENGTHS

Parameter	60 μm	100 μm	170 μm
Detected	41 (67.2)	43 (68.3)	54 (85.7)
Observed....	61	63	63

NOTE.—Values in parentheses are in %.

The flux density distributions at 60, 100, and 170 μm are given in Figure 11 . There is an obvious shift of the right-hand side of the histogram toward larger fluxes with increasing wavelength. The distribution at 170 μm is slightly broader than the distribution at 60 and 100 μm as a result of the larger completeness of the sample at longer wavelengths. Some faint galaxies detected at 170 μm failed detection at 60 μm, producing the cut in the faintest side in the histogram at 60 μm.

8. SUMMARY

A total of 63 spiral, irregular, and dwarf galaxies in the Virgo Cluster have been observed down to the limiting sensitivity of the ISOPHOT instrument on board *ISO* in bandpasses centered on 60, 100, and 170 μm. Rapid oversampled scans covering the entire optical extent of each target down to the 25.5 mag arcsec^{-2} *B*-band isophote and adjacent background directions were made using ISOPHOT's focal plane chopper in conjunction with a spacecraft raster. For the first time, data taken in this mode could be corrected for the complex nonlinear response to the illumination history in each observation. This allowed robust integrated photometry and structural information to be extracted down to the confusion limit in the 170 μm band and to the sensitivity limits imposed by low-level glitching in the 60 and 100 μm bands. The photometry in the 60 and 100 μm bands was found to be well correlated with the corresponding *IRAS* measurements for the 33 of the 63 galaxies detected by *IRAS*, with relative gains $ISO/IRAS = 0.95$ and 0.82 at 60 and 100 μm, respectively.

The faintest detected emissions from our galaxy sample were 50, 40, and 80 mJy at 60, 100, and 170 μm, respectively. The faintest 3 σ upper limits for integrated flux densities

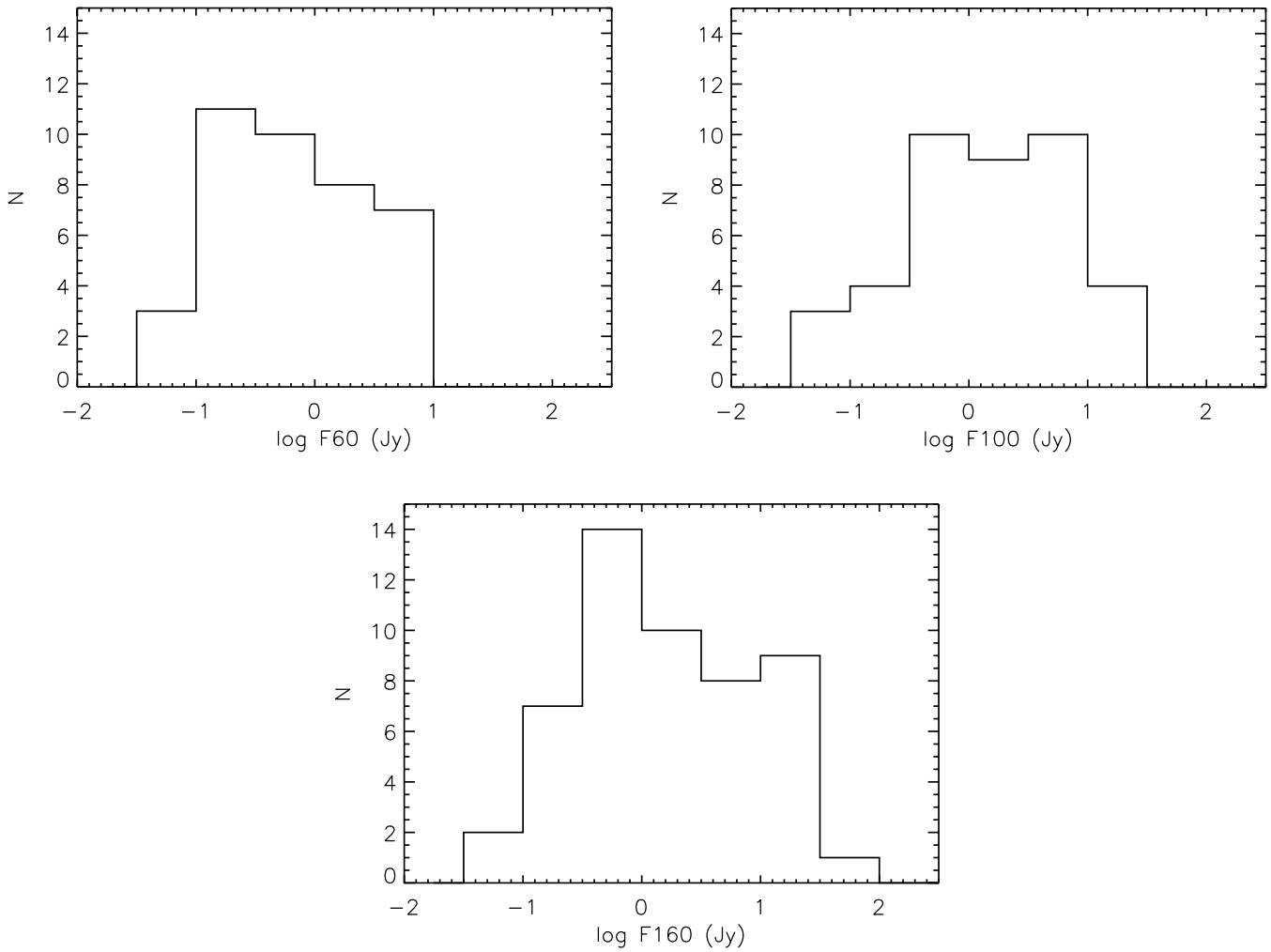

FIG. 11.—Flux density distributions at 60, 100, and 170 μm

were 30, 20, and 40 mJy (at 60, 100, and 170 μm). The averaged 3 σ upper limits (of galaxies with pointlike source appearance) were 43, 33, and 58 mJy (at 60, 100, and 170 μm). A total of 54 galaxies (85.7%) were detected at least at one wavelength, and 40 galaxies (63.5%) were detected at all three wavelengths. The highest detection rate (85.7%) was in the 170 μm band. From the observed 63 galaxies, 21 (33.3%) presented evidence for a nuclear and a disk component at least at one wavelength and four (6.3%) galaxies presented evidence for a multicomponent morphology at least at one wavelength.

The data presented in this paper were taken in guaranteed observing time made available by the ISOPHOT PI D. Lemke and the *ISO* Project Scientist M. F. Kessler. We thank U. Klein, J. Lequeux, and B. Binggeli for advice and discussions concerning the selection of galaxies observed, D. Skaley for assistance in entering the observing parameters into the uplink database, S. Niklas for support in the initial stages of the data evaluation, P. Abraham and the ISOPHOT data center for advice and assistance in the photometric comparison between *ISO* and *COBE*/DIRBE, and the staff of the *ISO* data center at Villafranca for advice on calibration and data analysis issues. R. J. T. thanks B. Madore for hospitality at the Observatories of the Carnegie Institution of Washington during the preparation of this paper. This project was supported by grant 50 QI 9201 of the DLR. This research has made use of the NASA/IPAC Extragalactic Database (NED), which is operated by the Jet Propulsion Laboratory, California Institute of Technology, under contract with the National Aeronautics and Space Administration.

REFERENCES

Alonso-Herrero, A., Rieke, M. J., & Rieke, G. H. 2000, ApJ, 530, 688
Barth, A. J., Ho, L. C., Filippenko, A. V., & Sargent, W. L. W. 1998, ApJ, 496, 133
Beichman, C. A., Neugebauer, G., Habing, H. J., Clegg, P. E., & Chester, T. J. 1988, *IRAS* Catalogs and Atlases: Explanatory Supplement (NASA RP-1190)
Binggeli, B., Popescu, C. C., & Tammann, G. A. 1993, A&AS, 98, 275
Binggeli, B., Sandage, A., & Tammann, G. A. 1985, AJ, 90, 1681
Binggeli, B., Tammann, G. A., & Sandage, A. 1987, AJ, 94, 251
Böhringer, H., Briel, U. G., Schwarz, R. A., Voges, W., Hartner, G., & Trümper, J. 1994, Nature, 368, 828
Boselli, A., Casoli, F., & Lequeux, J. 1995, A&AS, 110, 521
Boselli, A., et al. 1997a, A&A, 324, L13
———. 1998, A&A, 335, 53
Boselli, A., Tuffs, R. J., Gavazzi, G., Hippelein, H., & Pierini, D. 1997b, A&AS, 121, 507
Chini, R., Kreysa, E., Krügel, E., & Mezger, P. G. 1986, A&A, 166, L8

Deharveng, J.-M., Sasseen, T. P., Buat, V., Bowyer, S., Lampton, M., & Wu, X. 1994, A&A, 289, 715
de Jong, T., Klein, U., Wielebinski, R., & Wunderlich, E. 1985, A&A, 147, L6
Devereux, N. A., & Hameed, S. 1997, AJ, 113, 599
Devriendt, J. E. G., Guiderdoni, B., & Sadat, R. 1999, A&A, 350, 381
Dwek, E., Rephaeli, Y., & Mather, J. C. 1990, ApJ, 350, 104
Falcke, H., Wilson, A. S., & Simpson, C. 1998, ApJ, 502, 199
Gabriel, C., Acosta-Pulido, J., Heinrichsen, I., Morris, H., Skaley, D., & Tai, W.-M. 1997, in Proc. Data Analysis in Astronomy, ed. V. Di Gesu, M. J. B. Duff, A. Heck, M. C. Maccarone, L. Scarsi, & H. U. Zimmerman (Singapore: World Scientific), 409
Gavazzi, G., & Boselli, A. 1999, A&A, 343, 86
Gavazzi, G., Boselli, A., & Kennicutt, R. 1991, AJ, 101, 1207
González Delgado, R. M., Pérez, E., Tadhunter, C., Vilchez, J. M., & Rodríguez-Espinosa, J. M. 1997, ApJS, 108, 155
Haynes, M. P., & Giovanelli, R. 1984, AJ, 89, 758
Helou, G., Khan, I. R., Malek, L., & Boehmer, L. 1988, ApJS, 68, 151
Helou, G., Soifer, B. T., & Rowan-Robinson, M. 1985, ApJ, 298, L7
Ho, L. C., Filippenko, A. V., & Sargent, W. L. W. 1997, ApJS, 112, 315
Hoffmann, G. L., Williams, H. L., Salpeter, E. E., Sandage, A., & Binggeli, B. 1989, ApJS, 71, 701
Keel, W. C. 1983, ApJS, 52, 229
Kessler, M. F., et al. 1996, A&A, 315, L27
Klatt, U. 1993, Ph.D. thesis, Univ. Heidelberg
Leech, K. J., et al. 1999, MNRAS, 310, 317
Leech, K. J., Rowan-Robinson, M., Lawrence, A., & Hughes, J. D. 1994, MNRAS, 267, 253
Lemke, D., et al. 1996, A&A, 315, L64
Lisenfeld, U., Völk, H. J., & Xu, C. 1996, A&A, 306, 677
Lonsdale, C. J., & Helou, G. 1987, ApJ, 314, 513
Misiriotis, A., Popescu, C. C., Tuffs, R. J., & Kylafis, N.D. 2001, A&A, 372, 775
Moshir, M., et al. 1990, *IRAS* Faint Source Catalogue, Version 2.0
Niklas, S., Klein, U., & Wielebinski, R. 1995, A&A, 293, 56
Nilson, P. 1973, Uppsala General Catalogue of Galaxies, Nova Acta Regiae Soc. Sci. Upsaliensis, Ser. V:A, 1
Odenwald, S., Newmark, J., & Smoot, G. 1998, ApJ, 500, 554
Phillips, M. M., Charles, P. A., & Baldwin, J. A. 1983, ApJ, 266, 485
Phillips, M. M., & Malin, D. F. 1982, MNRAS, 199, 905
Pierini, D., et al. 2002, A&A, submitted
Pierini, D., Leech, K. J., Tuffs, R. J., & Völk, H. J. 1999, MNRAS, 303, L29
Pierini, D., Lequeux, J., Boselli, A., Leech, K. J., & Völk, H. J. 2001b, A&A, 373, 827
Popescu, C. C., Misiriotis, A., Kylafis, N. D., Tuffs, R. J., & Fischera, J. 2000a, A&A, 362, 138
Popescu, C. C., Tuffs, R. J., Fischera, J., & Völk, H. J. 2000b, A&A, 354, 480
Popescu, C. C., Tuffs, R. J., Völk, H. J., Pierini, D., & Madore, B. F. 2002, ApJ, in press
Rauscher, B. J. 1995, AJ, 109, 1608
Sandage, A., Binggeli, B., & Tammann, G. A. 1985, AJ, 90, 1759
Sanders, D. B., & Mirabel, I. F. 1996, ARA&A, 34, 749
Schröder, A. 1995, Ph.D. thesis, Univ. Basel
Sclar, N. 1984, Prog. Quant. Electron., 9, 149
Silva, L., Granato, G. L., Bressan, A., & Danese, L. 1998, ApJ, 509, 103
Soifer, B. T., Neugebauer, G., & Houck, J. R. 1987, ARA&A, 25, 187
Stauffer, J. R. 1982, ApJ, 262, 66
Stickel, M., et al. 2000, A&A, 359, 865
Thuan, T. X., & Sauvage, M. 1992, A&AS, 92, 749
Tully, R. B. 1989, Nearby Galaxies Catalog (Cambridge: Cambridge Univ. Press)
Tully, R. B., & Shaya, E. J. 1984, ApJ, 281, 31
Völk, H. J. 1989, A&A, 218, 67
Wheelock, S. L., et al. 1994, *IRAS* Sky Survey Atlas, Explanatory Supplement
Wunderlich, E., Wielebinski, R., & Klein, U. 1987, A&AS, 69, 487
Xu, C., & Buat, V. 1995, A&A, 293, L65

The Astrophysical Journal Supplement Series, 140:609–609, 2002 June

ERRATUM: "FAR-INFRARED PHOTOMETRY OF A STATISTICAL SAMPLE OF LATE-TYPE VIRGO CLUSTER GALAXIES" (ApJS, 139, 37 [2002])

Richard J. Tuffs, Cristina C. Popescu, Daniele Pierini, and Heinrich J. Völk
Max-Planck-Institut für Kernphysik

Hans Hippelein
Max-Planck-Institut für Astronomie

Kieron Leech and Leo Metcalfe
ISO Data Center, Astrophysics Division

and

Ingolf Heinrichsen and Cong Xu
Infrared Processing and Analysis Center

The legends for Figures 9 and 10 were switched. The legend for Figure 9 should read: "Uncorrected χ^2 values derived from fitting the Gaussian models to the maps vs. the corresponding flux densities at 60 μm obtained from integrating the model fit to infinity. The data were plotted as diamonds, except for those galaxies for which the model was an imperfect fit to the data, which were plotted as crosses. The solid line rising for $F_{60} > 1.5$ Jy represents the linear correlations between flux and χ^2, as a result of systematic errors due to the oversampling in cross-scan direction. For faint flux densities χ^2 is dominated by systematic errors, producing a clumpy distribution at the left-hand side of the plot, with a lower envelope, which we traced by a solid line to guide the eyes."

The legend for Figure 10 should read: "Model fits to the observed brightness profiles of all the Virgo galaxies from our sample (except for the interacting system VCC 1673/VCC 1676; see § 6.2.4). Statistical uncertainties for selected map pixels near the extremities and center of the scans are indicated by the 3 σ error bars. The legend is as in Fig. 8."

In addition, the references to Figures 9 and 10 in the main text should be interchanged.

The Press sincerely regrets this error.